

ARTICLE

<https://doi.org/10.1038/s41467-019-08934-3>

OPEN

Discovery of key whole-brain transitions and dynamics during human wakefulness and non-REM sleep

A.B.A. Stevner ^{1,2,3}, D. Vidaurre ⁴, J. Cabral ^{1,5}, K. Rapuano⁶, S.F.V. Nielsen⁷, E. Tagliazucchi^{8,9,10}, H. Laufs ^{9,10}, P. Vuust³, G. Deco^{11,12,13,14}, M.W. Woolrich⁴, E. Van Someren^{8,15} & M.L. Kringelbach^{1,2,3,5}

The modern understanding of sleep is based on the classification of sleep into stages defined by their electroencephalography (EEG) signatures, but the underlying brain dynamics remain unclear. Here we aimed to move significantly beyond the current state-of-the-art description of sleep, and in particular to characterise the spatiotemporal complexity of whole-brain networks and state transitions during sleep. In order to obtain the most unbiased estimate of how whole-brain network states evolve through the human sleep cycle, we used a Markovian data-driven analysis of continuous neuroimaging data from 57 healthy participants falling asleep during simultaneous functional magnetic resonance imaging (fMRI) and EEG. This Hidden Markov Model (HMM) facilitated discovery of the dynamic choreography between different whole-brain networks across the wake-non-REM sleep cycle. Notably, our results reveal key trajectories to switch within and between EEG-based sleep stages, while highlighting the heterogeneities of stage N1 sleep and wakefulness before and after sleep.

¹Department of Psychiatry, University of Oxford, Warneford Hospital, OX3 7JX Oxford, UK. ²Center of Functionally Integrative Neuroscience (CFIN), Aarhus University, 8000 Aarhus, Denmark. ³Center for Music in the Brain (MIB), Department of Clinical Medicine, Aarhus University, 8000 Aarhus, Denmark. ⁴Wellcome Centre for Integrative Neuroimaging, Oxford Centre for Human Brain Activity (OHBA), University of Oxford, Warneford Hospital, OX3 7JX Oxford, UK. ⁵Life and Health Sciences Research Institute (ICVS), School of Health Sciences, University of Minho, 4710-057 Braga, Portugal. ⁶Department of Psychological and Brain Sciences, Dartmouth College, 03755 Hanover, NH, USA. ⁷Department of Applied Mathematics and Computer Science, Technical University of Denmark, 2800 Kgs. Lyngby, Denmark. ⁸Netherlands Institute for Neuroscience, 1105 BA Amsterdam, The Netherlands. ⁹Department of Neurology, University Hospital Schleswig Holstein, Christian-Albrechts-Universität, 24105 Kiel, Germany. ¹⁰Department of Neurology and Brain Imaging Center, Goethe University, 60528 Frankfurt am Main, Germany. ¹¹Center for Brain and Cognition, Computational Neuroscience Group, Department of Information and Communication Technologies, Universitat Pompeu Fabra, Roc Boronat 138, Barcelona 08018, Spain. ¹²Institució Catalana de la Recerca i Estudis Avançats (ICREA), Passeig Lluís Companys 23, Barcelona 08010, Spain. ¹³Department of Neuropsychology, Max Planck Institute for Human Cognitive and Brain Sciences, 04103 Leipzig, Germany. ¹⁴School of Psychological Sciences, Monash University, Melbourne, Clayton, VIC 3800, Australia. ¹⁵Departments of Integrative Neurophysiology and Psychiatry GGZ-InGeest, Amsterdam Neuroscience, VU University and Medical Center, 1081 HV Amsterdam, The Netherlands. These authors jointly supervised this work: D. Vidaurre, M. L. Kringelbach. Correspondence and requests for materials should be addressed to A.B.A.S. (email: angus.stevner@psych.ox.ac.uk)

The primary behavioural observation of sleep is a lack of interaction with, and responsiveness to, the external world, i.e., a decreased level of arousal¹. The lack of communication with sleeping subjects implies that we rely on physiological recordings to scientifically describe and categorise sleep. The advent of modern neuroimaging techniques and network analyses has been explored to map and characterise spontaneous large-scale brain activity during wakefulness with high-spatiotemporal precision. Yet, our understanding of brain activity during sleep remains dictated by observations in a few channels of electroencephalographic (EEG) recordings.

Today, the dominant description of normal human sleep is represented by polysomnography (PSG), which relies mainly on EEG but also electromyography (EMG), electrooculography (EOG) and electrocardiography (ECG), as well as measures of respiration². On-going brain activity is recorded from a low number of EEG electrodes and typically categorised into wakefulness, rapid-eye movement (REM) sleep and—according to the most recent set of guidelines—three stages of non-REM (NREM) sleep (N1–N3)². Staging is based on the visual detection of spectral EEG qualities (e.g., alpha- and delta-frequency power) and sleep graphoelements (sleep spindles and K-complexes), many of which have been known since the 1930s³.

PSG has been essential in the development of modern sleep research, and remains undoubtedly the quickest and easiest way to establish arousal levels in individuals. Indeed, PSG-defined sleep stages were originally devised from EEG as surrogate markers of arousal thresholds, yet over time many have come to see them as a more or less exhaustive set of intrinsic canonical states that cover the full repertoire of brain activity during sleep. However, the use of (1) fixed scoring windows of 30 s and (2) only a few EEG electrodes means that PSG involves considerable averaging of brain activity in both time and space⁴—arguably leading to an incomplete representation of brain activity.

Furthermore, PSG corresponds relatively poorly to the subjective perception of sleep. Participants may experience being awake during periods with EEG signals otherwise fulfilling PSG criteria of NREM sleep^{5,6}. The relative lack of correspondence between PSG and subjective experience becomes important in populations with sleep complaints, where PSG is not indicated in the clinical evaluation of insomnia, the most common of all sleep disorders^{7,8}.

Recent developments in whole-brain neuroimaging and analyses support the examination of more sophisticated features of brain networks through functional connectivity (FC) and structural connectivity analyses, the detection of task-related and resting-state functional networks^{9,10}, and the development of mechanistic computational models^{11,12}. Yet, studies that have applied these promising tools to investigate large-scale brain activity of sleep have commonly relied upon PSG in a strict sense, thus regressing PSG stages onto functional brain data. This approach has yielded whole-brain correlates of PSG stages and sleep graphoelements, in terms of activation maps^{13,14}, FC patterns^{15–19}, graph-theoretical measures^{20,21} and EEG-microstates²². However, this top-down constraint by the low-resolution PSG scoring comes at the cost of exploring only a small fraction of the information available in the high-resolution neuroimaging data.

Rather than constraining analyses by traditional definitions of sleep stages, we propose to use novel data-driven analysis methods to elucidate whole-brain networks that can complement and potentially expand the classical understanding of sleep. This requires a sufficiently sensitive decomposition of whole-brain network activity in time. Building on a recent study showing that individual PSG stages can be extracted from functional magnetic resonance imaging (fMRI) recordings in a data-driven way²³, we

here leveraged the full spatiotemporal resolution of blood-oxygen-level dependent (BOLD) signals to find large-scale networks in sleep, applying a Hidden Markov Model (HMM)²⁴ on fMRI recordings of 57 healthy participants, who—according to simultaneously acquired EEG—cycled through PSG-defined stages of wakefulness and NREM sleep. Crucially, the HMM decomposition was not constrained by PSG stages, but rather allowed us to discover directly from the data, at a time-scale of seconds, the relevant brain network transitions explored by the human brain during the wake-NREM sleep cycle. Compared to other methods for extracting dynamic FC²⁵, the HMM framework explicitly models the transition probabilities between its inferred states. We show that this information can be used to discover new whole-brain aspects of sleep, complementing the traditional segmentation of brain activity offered by PSG.

Results

Whole-brain network states identified by HMM. In order to extract the large-scale networks inherent to whole-brain recordings of the wakefulness-NREM sleep cycle, we estimated an HMM on fMRI data from 57 healthy participants (age 23.5 ± 3.3 years, 39 females). Participants were instructed to lie still in the scanner with their eyes closed. Each recording had a duration of 52 min, and was accompanied by acquisitions of EEG, EMG, ECG and EOG, based on which PSG staging was performed by an expert, according to the AASM criteria² (see Supplementary Table 1). Following preprocessing, the voxel-wise BOLD timecourses were temporally averaged over 90 region-of-interest (ROI) timecourses, using the cortical and subcortical regions of the automated anatomical labelling (AAL) atlas²⁶. ROI timecourses were demeaned and variance-normalised for each participant, and subsequently concatenated across participants along the temporal dimension.

The estimated HMM contained a set of whole-brain network states, each defined as a multivariate Gaussian distribution, including: (i) a mean activation distribution, representing the mean level of activity in each ROI when a state is active; and (ii) an FC matrix, summarising the pairwise temporal co-variations occurring between the ROIs during that state. The HMM also contained a transition probability matrix with the probabilities of transitioning between each pair of states. Each state also had an associated state timecourse describing the points in time (defined by the fMRI sampling, $TR = 2.08$ s) where the state was active^{24,27}. The HMM was endowed with 19 states, and, crucially, was given no information about the PSG staging for its estimation. An illustration of the analysis workflow is given in Fig. 1 (see Methods for details).

To allow for unbiased within-participant testing, when comparing the HMM output to the PSG scoring we considered the subset of the HMM output that corresponded to the data from the 18 participants that reached all four PSG stages (wakefulness, N1, N2 and N3, see Supplementary Table 1).

Whole-brain network states underlie PSG sleep stages. The 19 whole-brain network states, inferred solely from the fMRI by the HMM, contained most of the temporal information given by the PSG stages that were scored from the EEG independently of the fMRI. The HMM state timecourses and the PSG scoring are plotted together in Fig. 2a for the 18 participants that included all four PSG stages, illustrating how the activity of the different HMM states co-varied with specific PSG stages. We have highlighted the HMM state timecourses of two participants to ease visual inspection, however, the temporal relationships between HMM states and PSG stages were consistent across the group. It can be observed, for example, that HMM state 8 occurred most

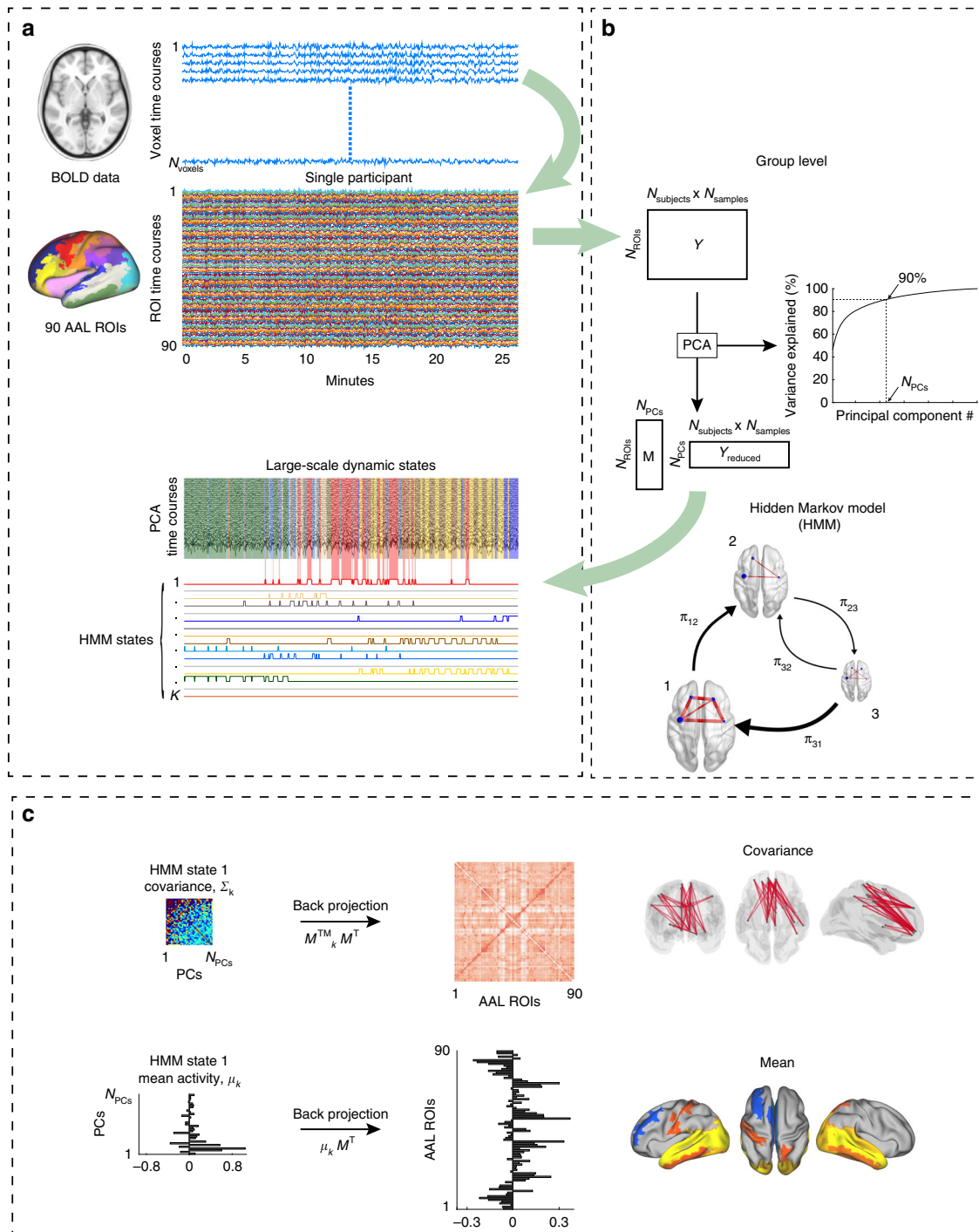


Fig. 1 Dynamic whole-brain networks from fMRI sleep recordings using a Hidden Markov Model. **a** ROI timecourses were extracted by averaging BOLD signals across voxels within each of the 90 cortical and subcortical AAL areas for each participant. Each ROI timecourse was demeaned and normalised by its standard deviation. **b** The data were concatenated across participants, and the dimensionality was reduced using PCA (principal component analysis), such that ~90% of the variance of the ROI timecourses was retained. The HMM was run on the PCA timecourses, resulting in K number of states with associated timecourses, each describing the points in time each state is active and inactive. **c** Each HMM state was characterised by a multivariate Gaussian distribution comprising a covariance matrix, Σ_k , and a mean distribution, μ_k . The state-specific mean distributions and covariance matrices were back-projected to the MNI space of the AAL by using the mixing matrix, M^T from the PCA decomposition, yielding a mean activation map and an FC matrix for each HMM state

often during wakefulness, HMM state 3 occurred during N2 sleep and HMM state 16 occurred during N3 sleep.

We quantified the temporal association between the PSG stages and the HMM state timecourses using multivariate analysis of variance (MANOVA). This allowed us to ask if the 19 HMM

states were significantly grouped in time by the four PSG stages (for the 18 participants that included all four PSG stages). Through non-parametric testing (see Methods) we confirmed this temporal relationship ($p < 0.05$, permutation testing, see Supplementary Figure 1b). The MANOVA placed the PSG stages in the

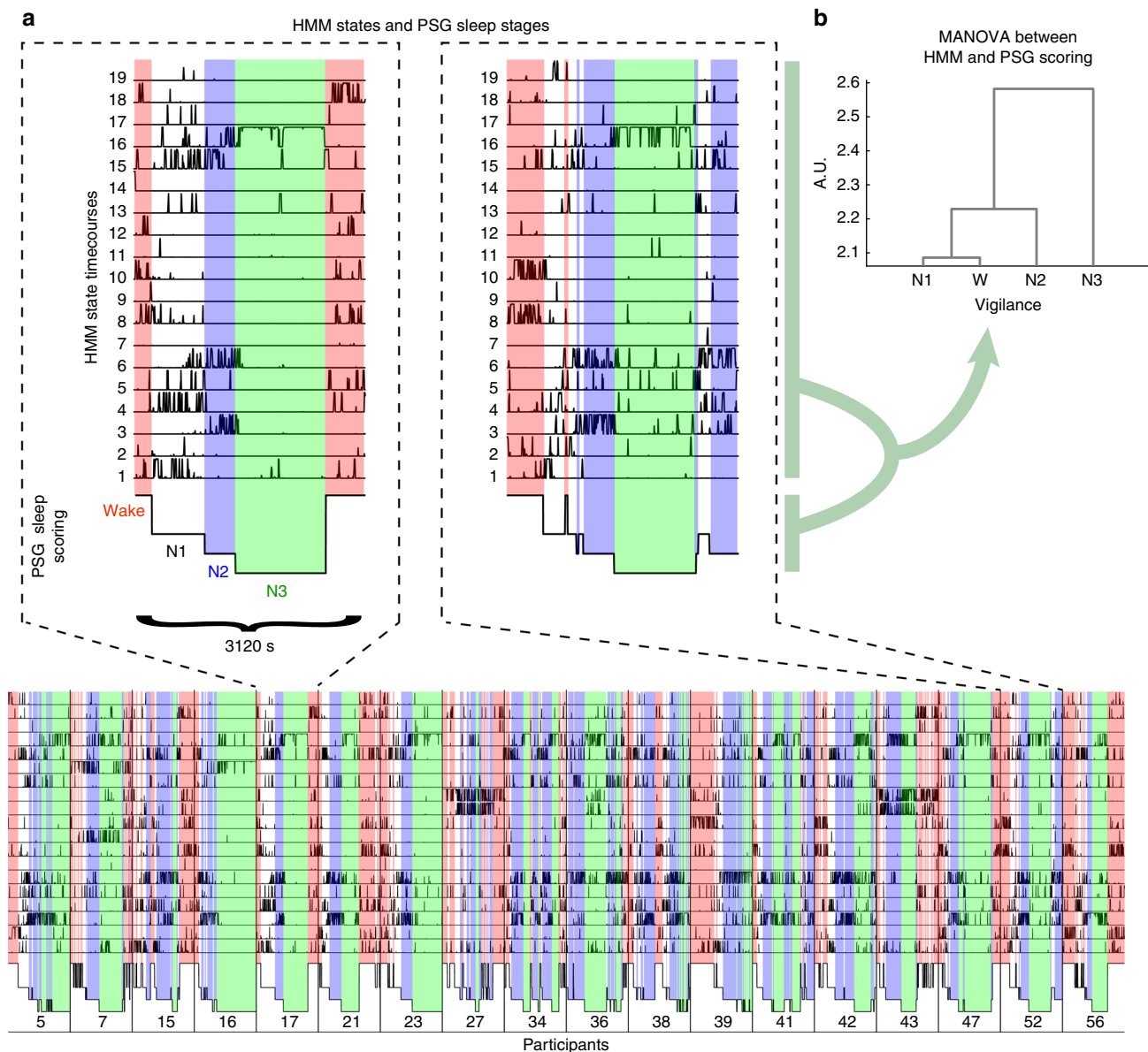


Fig. 2 State timecourses of whole-brain network states and their association to polysomnography. **a** The figure shows the 19 HMM state timecourses describing each state's probability of being active at each sample point of the fMRI sessions in the 18 participants that reached all four PSG stages. Below the HMM state timecourses are shown the independently obtained PSG sleep scoring (based on the simultaneously acquired EEG). The coloured overlay shows periods scored as wakefulness (red), N1 (white), N2 (blue) and N3 (green). The two dashed boxes highlight the HMM state timecourses and PSG scoring of two representative participants. Note, how the majority of HMM timecourses varied with the PSG stages, in highly consistent ways across participants. A few 'sporadic' HMM states, occurring mainly in a few participants, are also visible (e.g., states 11 and 12). **b** Quantifying the multivariate relationship between the HMM states and the PSG scoring, through the use of MANOVA, revealed a hierarchical grouping of the HMM states, in which wakefulness and N1 sleep were separated from N2 sleep, which in turn was separated from N3 sleep

space of the HMM state timecourses, resulting in the clustering dendrogram of Fig. 2b, with wakefulness and N1 sleep significantly separated from N2 sleep, which in turn was further separated from N3 sleep.

Whole-brain network states track different PSG stages. Next, we examined the contribution of the individual whole-brain network states to the multivariate relationship, established above, between the HMM and the PSG scoring. We quantified the temporal sensitivity and specificity of the HMM states for each of the PSG stages. For each of the 18 participants that included all four PSG stages, we defined the sensitivity of each HMM state as the proportion of total time spent in a PSG stage, in which this

HMM state was active. Specificity was defined as the likelihood of finding each HMM state active during a given PSG stage. We compared the sensitivity and specificity for each PSG stage within each of the HMM states, using paired *t* tests and a randomisation scheme of the PSG scoring (see Methods). The results are presented in Fig. 3a, b. HMM state 8 occupied a large proportion of PSG-scored wakefulness, i.e., it exhibited high sensitivity for wakefulness (see Fig. 3a). Since this whole-brain network state was significantly more sensitive to wakefulness than to any of the other PSG stages, i.e., it rarely occurred outside of wakefulness, its specificity for wakefulness was also high (see Fig. 3b). This combined sensitivity and specificity for wakefulness was also found for HMM states 10 and 18.

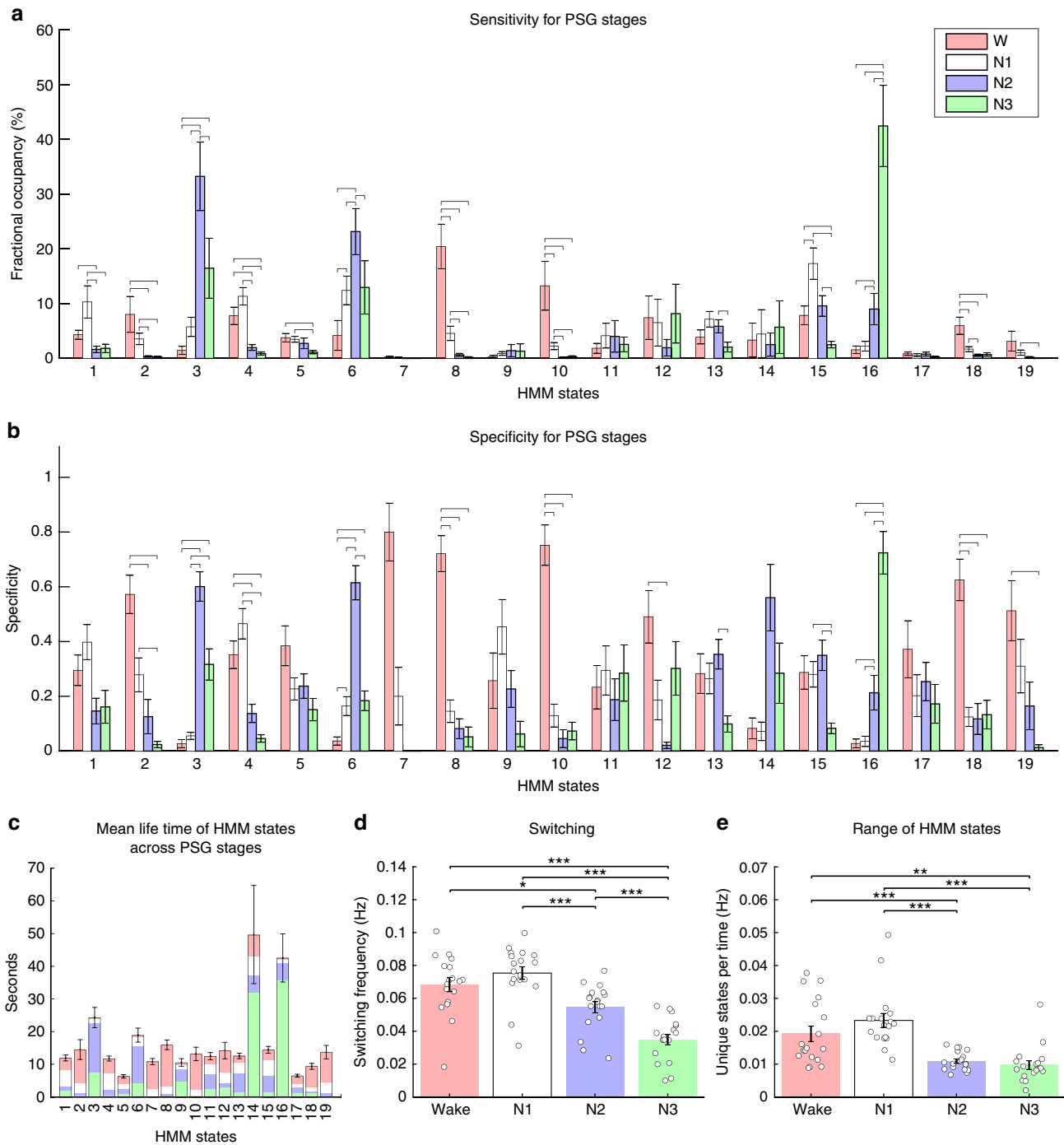


Fig. 3 Sensitivity and specificity of HMM states and dynamics within polysomnography stages. **a** Fractional occupancies of each of the 19 HMM states computed within the four PSG stages corresponded to the PSG-sensitivity of the whole-brain network states. The coloured bars and error bars show the average and standard error, respectively, across the 18 participants that included all four PSG stages. **b** PSG-specificity of the HMM states for each of the four PSG stages. Specificity corresponds to the probability of an HMM state occurring within a PSG stage. The bars represent the group average and the error bars the standard error ($n = 18$). In **a** and **b** horizontal lines show significant differences within HMM states, with p values < 0.01 as evaluated through paired t tests and permutation testing. **c** The mean life times of the 19 HMM states are shown by the bars, representing values averaged across the 18 participants. Error-bars represent the standard error across participants. Each HMM state is coloured according to the probability of finding it within each of the four PSG stages, i.e., their PSG specificity. Note how HMM states with high specificity for N3—and to a lesser extent N2—exhibit longer mean life times. **d** The dynamics of the HMM transitions were calculated within each of the four PSG stages, in terms of switching frequency ('Switching'), and **e** the number of different HMM states visited per time ('Range of HMM states'). These measures significantly separate the four PSG stages suggestive of a higher dynamical repertoire during wakefulness and N1. In **d** and **e** error bars represent standard error across participants and significant differences between PSG stages are denoted by stars: one star: $p < 0.05$, two stars: $p < 0.01$ and three stars $p < 0.001$; all evaluated using paired t tests and permutations. W: wakefulness, N1: N1 sleep, N2: N2 sleep, N3: N3 sleep

Select whole-brain network states displayed similarly exclusive sensitivity and specificity profiles for N2 (HMM states 3 and 6) and N3 sleep (HMM states 16). Notably, this was not the case for N1 sleep. The whole-brain network states occupying most of N1 sleep, such as HMM states 1, 4 and 15, were not found specific for this PSG stage. Instead these states would also occur with considerable likelihood outside of N1 sleep, although rarely during N3 sleep.

In summary, wakefulness was found to correspond to a collection of whole-brain networks states, while N2 and N3 were characterised by less state-diversity, and dominated by two and one whole-brain states, respectively. In contrast, no single whole-brain states were found specific for N1 sleep, which instead was modelled by a collection of HMM states with mixed PSG profiles.

Changes in whole-brain network dynamics between PSG stages. Having the whole-brain network states temporally defined allowed us to investigate the large-scale brain dynamics of the traditionally defined PSG stages in the 18 participants that reached all PSG stages during their recordings.

In Fig. 3c, the HMM states are represented by a bar plot showing their mean lifetimes, i.e., the average duration of the state visits. The bars have been overlaid with colours depicting the PSG specificity averaged across the corresponding HMM states. HMM states with high specificity for N2 and N3 (HMM states 3, 6 and 16) generally expressed longer mean lifetimes than those related to wakefulness and N1. The mean lifetimes of the HMM states ranged from seconds to tens of seconds.

Figure 3d, e shows two summary measures for the dynamics of the whole-brain network states during the individual PSG stages: (i) the amount of switching defined as the average number of transitions between HMM states during a given PSG stage divided by the total time a participant spent in this PSG stage and (ii) the range of HMM states defined as the number of unique states visited during the given PSG stage divided by the total time a participant spent in this PSG stage. Both measures were estimated for each PSG stage, within each of the 18 participants that included all four PSG stages, and normalised by time. Wakefulness and N1 sleep expressed significantly higher values than N2 and N3. Interestingly, the amount of switching was particularly low for N3 sleep.

In summary, unique state visits per time were few and of long durations during N2 and N3 relative to wakefulness and N1 sleep. Consequently, the switching between and range of HMM states were significantly higher in wakefulness and N1.

Sleep stages as modules of whole-brain network transitions. So far, we have used the traditional PSG stages to organise and evaluate the temporally resolved whole-brain network states. Yet, the data-driven nature of the HMM also allowed us to perform reverse inference, and consider the temporal progression of HMM states, taking this—rather than the PSG staging—as a starting point. This way, we were able to ask if the high-resolution, fMRI-based, HMM suggests new aspects of the wake-NREM sleep cycle, hidden from the EEG-based PSG. For this purpose, we examined the transition probabilities of the HMM states, extracting modules of HMM states that transitioned more often between each other than to other states—as recently identified for the waking resting state in ref. ²⁴.

The whole-brain network states organised into a transition map as presented in Fig. 4, where the 19×19 transition probability matrix (Fig. 4a) was submitted to a modularity analysis (see Methods). By considering the most frequent transitions between the HMM states that were consistent across participants (see Fig. 4b), the thresholded transition matrix organised into four

partitions or transition modules (see Fig. 4c, and Methods), suggestive of a lower time scale (see ref. ²⁴ and Supplementary Discussion 1). When these most consistent transitions are presented as a transition map, and each whole-brain network state is represented by a circle plot indicating its specificity for each of the four PSG stages, it can be seen that the HMM states exhibit a strong temporal structure (Fig. 4d). In line with the MANOVA results above, this transition map describes an overall progression from states with high specificity for PSG-defined wakefulness (red module) through states with more activity during, albeit not significant specificity for, N1. From here transitions lead towards states specific to N2 sleep and finally to a single whole-brain network state modelling N3 sleep. The N2- and N3-related HMM states thus grouped together in the blue module.

Interestingly a collection of HMM states with mixed PSG-specificity formed a transition module of their own. This white module was intercalated between the red module of wakefulness in the top and the blue module of N2/N3 sleep. Even if the included HMM states were not specific for PSG-defined N1 sleep, the white module appears in the location of the transition map, where one would expect to find N1 or rather sleep onset.

The transition map suggested two sub-divisions of HMM states with high specificity for wakefulness. The red module in close proximity to the white module of N1-related states, and the black module sending transitions to the blue module of consolidated NREM sleep. This apparent separation of wakefulness and the asymmetric relationship to the sleep-related HMM states led us to the hypothesis that one of these could represent wakefulness after sleep onset (WASO). Given the poor correspondence between the HMM states and the general uncertainty associated with the staging of PSG-defined N1 sleep (see Discussion), we chose to define WASO as PSG-staged wakefulness, which followed after visits to N2 sleep²⁸. By computing the sensitivity and specificity of the whole-brain network states in the subset of the data corresponding to the 31 participants who woke up after having reached N2 sleep (see Supplementary Table 2), we were able to confirm this hypothesis. As shown in Supplementary Figure 2, HMM states 5, 17 and 18 were all more sensitive and specific to WASO compared to wakefulness prior to N2 sleep. Whereas periods of wakefulness prior to and after sleep are scored equally in PSG, the whole-brain network states separated these into two different transition modules.

Although this transition map suggests multiple pathways from wakefulness (red module) to the white module of NREM sleep, it is interesting to note that HMM state 8 has direct access to HMM state 15, which in turn guards the transition to the blue module of N2/N3 sleep. Similarly, waking-up relates to a transition from HMM state 4 to HMM state 10, which in turn connects with HMM state 18 of the black WASO module. Further it is worth noticing the strong triangular transition structure within the blue module between the N2-specific whole-brain network states (HMM states 3 and 6) and the N3-modelling HMM state 16.

In summary, while agreeing with the overall sequence of PSG stages, the organisation of the transition modules also points to aspects of sleep-related brain activity that the PSG scoring cannot access, including the data-driven suggestions of N1 sleep, WASO-related whole-brain network states, and multiple transition pathways between wakefulness and sleep.

Spatial activation and FC maps of whole-brain network states.

We present the spatial maps of the whole-brain network states in the order suggested by the transition modules of Fig. 4d. Figure 5 and Fig. 6 show the mean activation maps, while the corresponding FC information is presented in Supplementary Figures 3–5 and 17–18 (see also Supplementary Note 5).

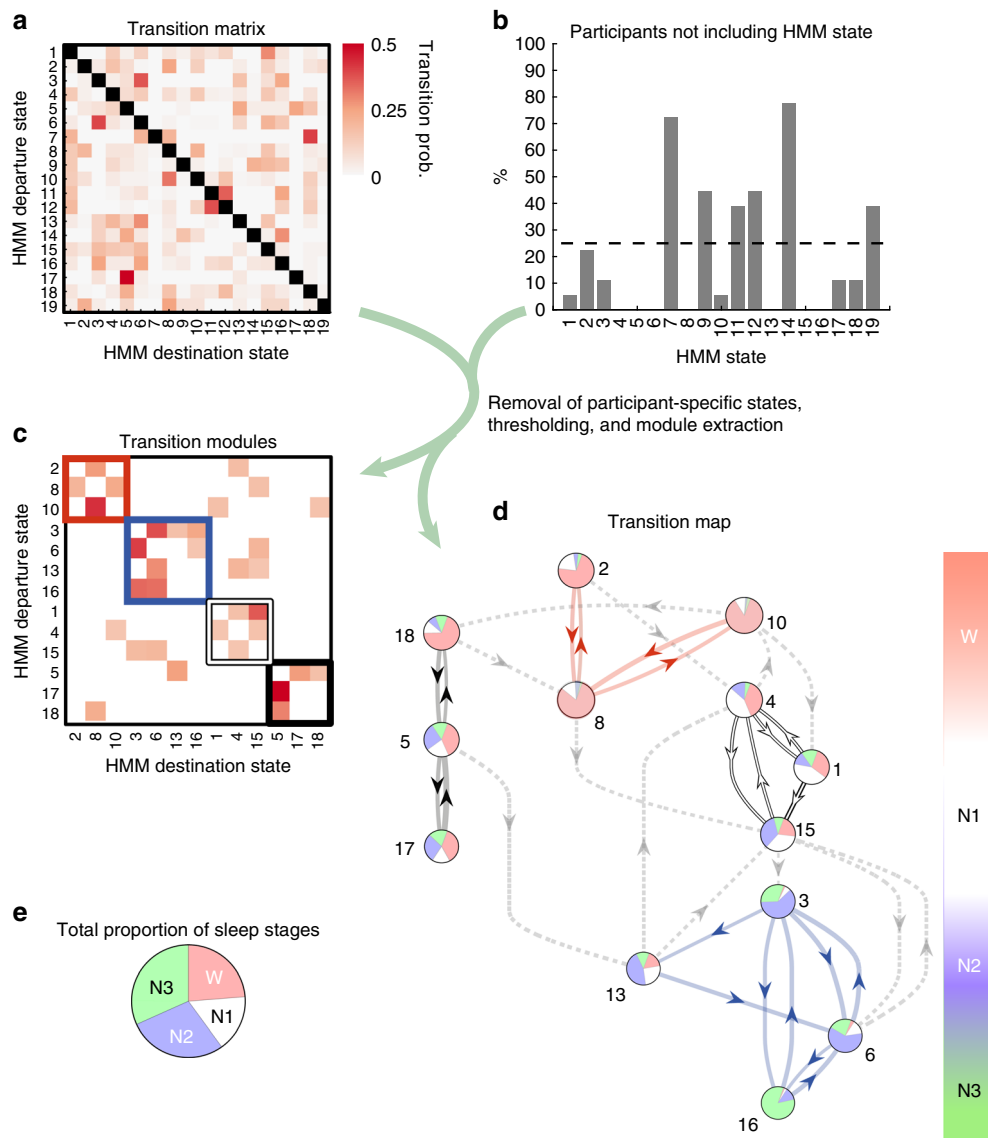


Fig. 4 Investigating modules of transitions between whole-brain network states. **a** The figure shows the 19 × 19 transition probability matrix of the HMM states calculated for the 18 participants that included all four PSG stages in their respective scanning session. This quantifies the likelihood of transitioning from any given state to any other state, yielding each matrix entry: transition probability from departure state to destination state. **b** A few HMM states were ‘sporadic’ and did not occur consistently across participants. HMM states not occurring in more than 25% of the participants were excluded. **c** The strongest transitions of the consistent HMM states were partitioned through a modularity analysis, and reorganised in a matrix according to the four resulting modules. **d** The transitions shown in **c** are presented as a transition map with each state depicted as a pie plot expressing its specificity for each of the four PSG stages. Arrows show the direction of the transitions with thickness proportional to the transition probability. The transitions describe a passage from HMM states with high activity during wakefulness in the top, further down through HMM states including more N1, and down to HMM states specific to N2 and finally N3. Interestingly, wakefulness appears to be represented by two modules (red and black). Even though no individual HMM state showed clear specificity for N1 sleep, a module (white) is evident between HMM states with specificity for wakefulness and HMM states with specificity for N2 and N3 sleep. **e** Pie chart showing the total proportion PSG stages within the 18 participants. Transition prob.: transition probability

In Fig. 5a, which shows the red module of wakefulness, the mean activation maps of HMM states 2 and 8 resemble resting-state network (RSN) configurations^{9,10}. The main increases of HMM state 8 were thus seen in key areas of the default-mode network (DMN)²⁹, including the bilateral posterior cingulate cortex, bilateral angular cortex, bilateral middle temporal cortex, and bilateral medial prefrontal cortex. These DMN-like increases in HMM state 8 were accompanied by decreases in the so-called anti-correlated network (ACN), involving the supramarginal gyrus and the dorsolateral part of the frontal cortex³⁰. In contrast, HMM state 2 was characterised by increases in many of these ACN-areas, including the bilateral supramarginal gyrus, middle

cingulate cortex and dorsolateral part of the frontal cortex. These results suggest an inverse relationship between the activity of the DMN and the ACN, which is an established trait of these RSNS³⁰. Since the discovery of these RSN patterns they have been hypothesised to reflect complex cognitive processes. The DMN has been linked to inwardly directed mentation, such as autobiographical memory and mind wandering^{31,32}. The ACN overlaps with areas also referred to as the dorsal attention network³³ or the central executive network (CEN)³⁴, and has been proposed to be involved in more externally directed processes, including attention³⁵. In agreement with this, we found these high-order RSNS to be relatively exclusive for

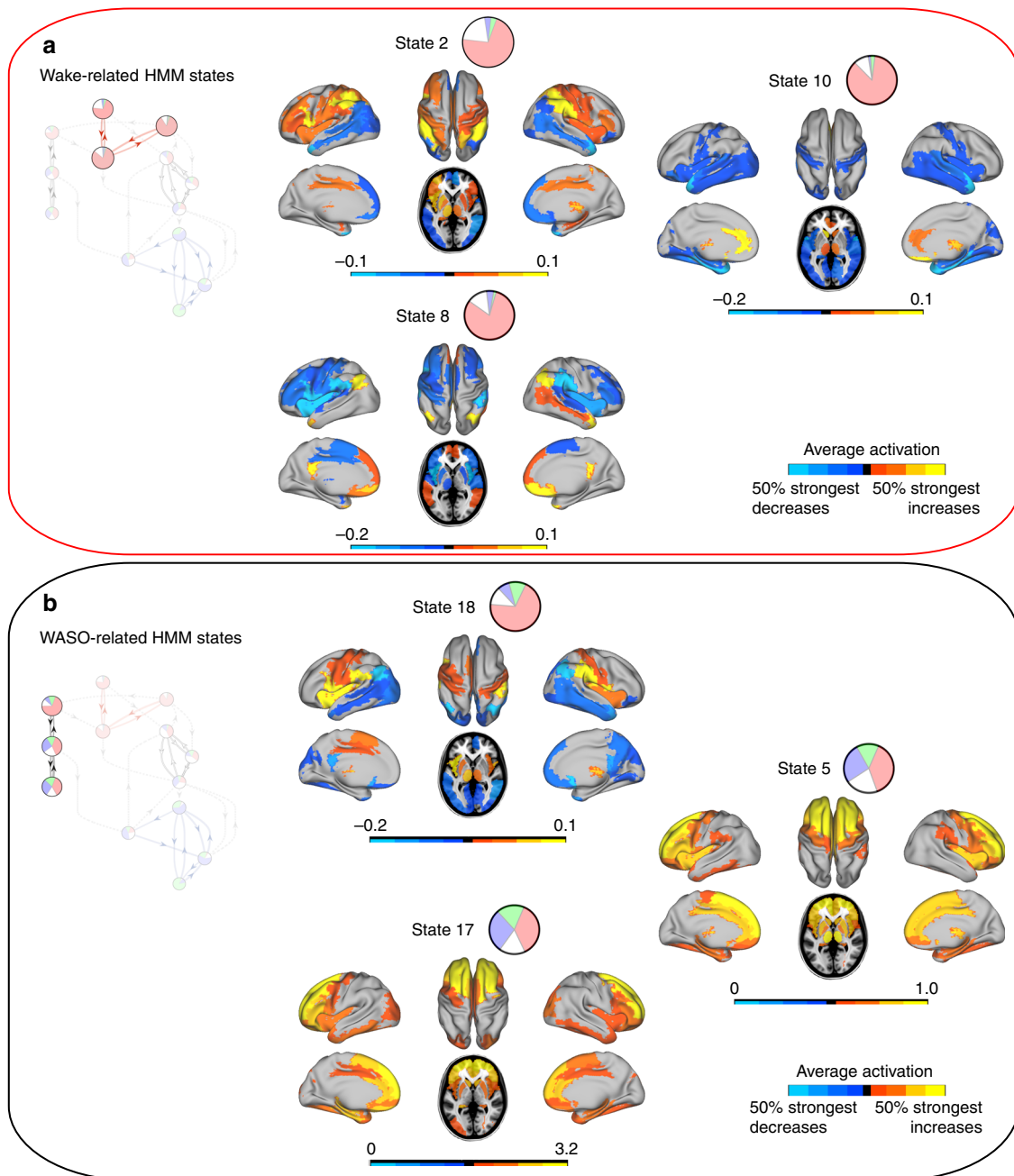


Fig. 5 Mean activation distributions of wakefulness-related HMM states. **a** Three HMM states identified as sensitive and specific to wakefulness prior to sleep. Note HMM state 8 with DMN-like configuration increases, and concomitant decreases in DAN/CEN-like areas. **b** Three HMM states associated to wakefulness after sleep. There are marked frontal increases in mean activation in HMM states 5 and 17. All maps were thresholded above the 50% strongest positive and negative changes, respectively

wakefulness. However, previous investigations have suggested a rather ubiquitous presence of both the DMN and the ACN, not just in wakefulness but, in all stages of NREM sleep^{15,17,36} (see Supplementary Discussion 1).

Figure 5b shows the mean activation maps of whole-brain network states with higher sensitivity and specificity for WASO (black module). The mean activation map of HMM state 18 expressed a distribution similar to that of HMM state 8 (see Fig. 5a), but with opposite signs. Hence, HMM state 18 showed decreases in DMN-related areas, and increases in regions overlapping the ACN. HMM states 5 and 17 were both characterised by mean activation increases in the frontal cortices. Interestingly, findings from high-density EEG studies of participants waking up

from sleep show that the posterior parts of the cortex are particularly ‘slow’ at returning to levels of activity seen prior to sleep³⁷. Consistent with this, converging evidence from PET and fMRI have indicated frontal cortical activity to be increased relative to that of posterior areas upon awakening^{28,38,39}.

The whole-brain network states of the white N1-related module are represented in Fig. 6a. A general observation for these spatial maps is the inverse relationship between mean activation in subcortical areas (thalamus and parts of the basal ganglia) and primary sensory cortical areas. Increases in subcortical activity were accompanied by decreases in primary sensory areas of the cortex and vice versa. This was true for HMM states 4 and 15 (and HMM state 1 although its decreases were not

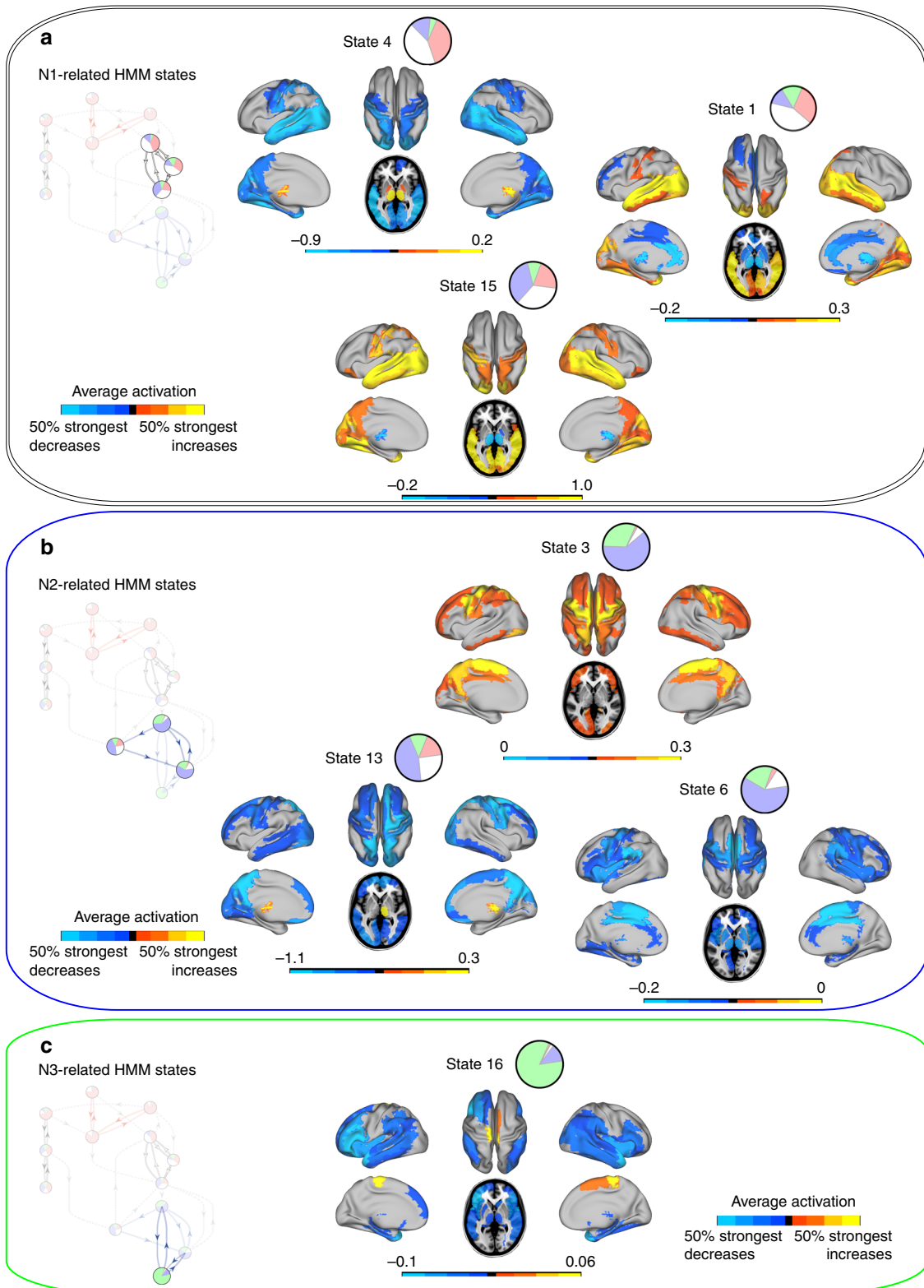


Fig. 6 Mean activation distributions of sleep-related HMM states. **a** HMM states associated with N1 sleep showed opposite signs in mean activation in subcortical areas and primary sensory areas of the cortex. **b** Three HMM states related to N2 sleep. HMM states 3 and 6 in particular showed peak increases and decreases, respectively, in areas previously identified as fMRI-correlates of sleep spindles. **c** HMM state 16 is dominating slow wave sleep (N3). Interestingly, there are marked decreases in mean activation in frontal areas and insula, and very localised increases in the supplementary motor area and paracentral lobule. All maps were thresholded above the 50% strongest positive and negative changes, respectively

confined to subcortical areas, but supplemented by decreases in the anterior and middle cingulate cortex). This is consistent with intracortical studies of the sleep onset process in rats⁴⁰ and in humans⁴¹ showing that thalamic changes in dynamics precede those of cortical areas near the onset of NREM sleep. Previous fMRI studies of NREM sleep have suggested decreased connectivity between the thalamus and cortical regions as perhaps the most consistent trait of FC during N1 sleep^{16,18,19,23}.

N2 sleep was dominated by HMM states 3 and 6, and the mean activation maps of these whole-brain network states are shown in Fig. 6b. The supplementary motor area was involved in both of these states; in HMM state 3 as increases in concert with the bilateral precuneus and primary motor cortices; and in HMM state 6 as decreases together with the bilateral thalamus, middle cingulate, supramarginal cortex, and the Rolandic operculum. Interestingly, these configurations overlap considerably with those previously reported in studies mapping fMRI-correlates of sleep spindles^{42,43}, which represent a defining EEG-feature of N2 sleep. However, no HMM state appeared to be driven solely by either sleep spindles or K-complexes. By identifying sleep spindles and K-complexes from the EEG data, we assessed the temporal relationships between these graphoelements and the HMM states. In summary the HMM states that were dominant during N2 sleep showed comparable sensitivity and specificity to both types of graphoelements, and hence the HMM did not appear to have assigned individual states for either spindles or K-complexes (for further information please see the Supplementary Discussion 1, Supplementary Note 4, Supplementary Table 3, and Supplementary Figures 19–21).

HMM state 16 accounted for the majority of time spent in N3 sleep. The corresponding mean activation map is shown in Fig. 6c. Apart from some very localised increases in the paracentral lobe and adjacent supplementary motor area the mean activation was characterised mainly by decreases, particularly in the bilateral middle and superior temporal pole, the orbital part and the operculum of the inferior frontal cortex, bilateral insula as well as medial temporal areas. These frontal decreases are consistent with previous PET findings of decreased metabolism in these areas during N3 sleep, which in turn are believed to reflect the high, localised concentration of slow-wave activity⁴⁴.

Discussion

Using a data-driven exploration of large-scale brain networks and associated dynamics from continuous fMRI recordings, we have explored the rich dynamical complexity in spatiotemporal patterns of brain activity during the healthy wake-NREM sleep cycle. Moving beyond the traditional PSG stages of sleep, we used a HMM to extract 19 recurring whole-brain network states, defined in space by patterns of mean BOLD activation and FC, and defined in time as the probability of being active at each time point of the fMRI sampling. Comparing the temporal evolution of the HMM-derived whole-brain network states with the independently obtained EEG-based PSG scoring, we have discovered a rich repertoire of brain dynamics underpinning the traditional PSG stages. The temporal resolution of the HMM identified state lifetimes on the order of seconds, providing a temporally fine-grained description of the traditional PSG stages. Crucially, a close examination of the HMM transition map furthermore revealed a heterogeneity of large-scale network activity that PSG cannot fully capture.

The description of brain activity offered by PSG has for long been acknowledged as incomplete, and attempts have been made to harvest more information from scalp EEG in a search for features relevant for sleep, overlooked by PSG^{45–47}. Our work adheres to this aim, while, through fMRI, incorporating evidence

of whole-brain spatial detail. Previous studies have indicated that fMRI can be used to identify dynamic re-configurations of large-scale brain activity during the conventional EEG-based sleep stages, either in form of voxel-wise changes in activity⁴⁸, changes in connection strengths in resting-state networks⁴⁹ or through long-range temporal dependencies in the BOLD signal³⁶. Rather than direct reflections of the conventional sleep stages, what has emerged from our HMM analysis is a probabilistic representation of the PSG scoring in the space of whole-brain network states and transitions. Agreements as well as disagreements between the PSG scoring and the independent HMM decomposition became clear in the transition map (Fig. 7). Wakefulness, N2 sleep and N3 sleep were each represented by one or more whole-brain network states, forming a good correspondence with PSG. In contrast, no states were found specific for N1 sleep. Furthermore, while treated equivalently in PSG staging, wakefulness prior to sleep and WASO were represented in the transition map as two different modules with different repertoires of large-scale brain networks. Consequently, the transition map also identified specific whole-brain network transitions underlying the descent to, and ascent from, NREM sleep.

Consistent with previous neuroimaging studies that have used regression analyses to identify consistent differences between traditionally defined sleep stages in terms of large-scale brain activity^{13,14,50}, PSG-defined wakefulness, N2 and N3 sleep each corresponded well to specific collections of whole-brain network states (see Supplementary Discussion 1). However, the HMM additionally provided access to the large-scale brain dynamics of the PSG stages, showing that the state repertoire, when estimated as amount of switching and range of states visited, is higher in wakefulness than in both N2 and N3 sleep. That a higher and more complex state repertoire is important for the brain to support wakeful consciousness follows from theoretical frameworks^{51–53} and has received empirical support from a series of combined TMS and EEG studies⁵⁴. From a large-scale network perspective fMRI has been used to show how an enhanced state repertoire is associated with an ‘expanded’ consciousness during the psychedelic experience^{55,56}. In the context of sleep, however, the large-scale network evidence is mainly represented by static FC studies suggesting decreased information integration during N2 and N3 sleep using graph theory^{20,21}, as well as a higher exploration of the structural connectome during wakefulness⁵⁷. Here, we have provided more direct evidence of a higher state repertoire in whole-brain dynamics during wakefulness.

The transition map identified a key trajectory from wakefulness in the red transition module to NREM sleep in the white transition module (see Fig. 7d), represented by the transition departing from the whole-brain network state with increased mean activation in the DMN. The proposed association between the DMN and inwardly directed mentation^{31,32} makes this finding intriguing, in the sense that it may suggest a role for the DMN as a ‘gate’ in the process of initiating sleep. Whole-brain network evidence of sleep initiation may improve our understanding of sleep disorders like insomnia where PSG criteria are difficult to apply^{7,58}, and hypersomnia disorders⁵⁹. Related hereto, a recent study identified switching instability to and from N2 sleep, together with difficulties reaching N3 sleep as important traits of insomnia⁶⁰. In the transition map we saw N2- and N3-related whole-brain network states forming a strong triangular loop of transitions (see Fig. 7e). This stable configuration of transitions may not be present in people suffering from insomnia.

The two main incongruities between the temporal segmentation suggested by the HMM and the PSG scoring concerned N1 sleep and WASO. N1 sleep did not correspond to any single state or any group of states identified by the HMM. This is likely related to the current consensus that PSG-defined N1 does not represent a

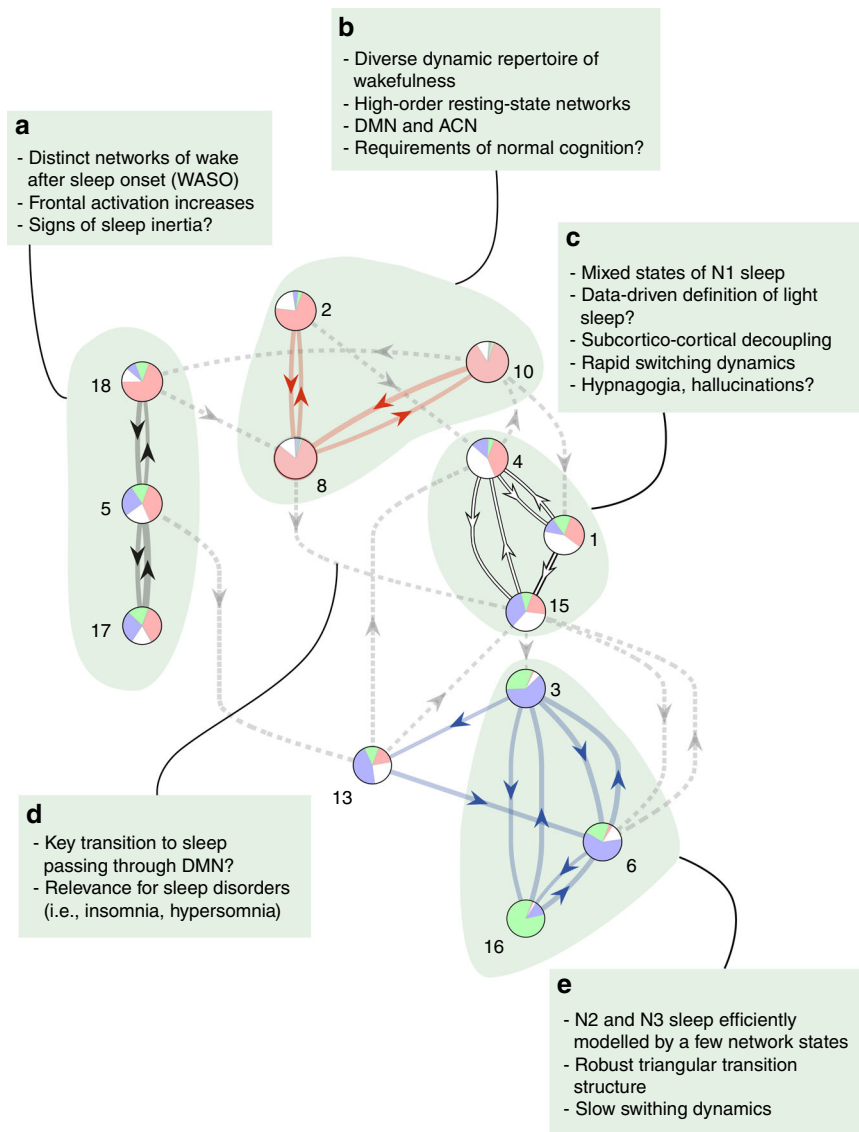


Fig. 7 A whole-brain network perspective on the human wake-NREM sleep cycle. The main discussion points of our results have been highlighted in the transition map of the whole-brain network states. Boxes a to e summarise the new perspectives provided by our HMM analysis

clear-cut sleep stage⁶¹, but rather an ill-understood mix of wakefulness and sleep. Compared to N2 and N3 sleep with their well-defined EEG spectral properties, such as K-complexes, spindles, and slow waves, N1 remains the most vaguely defined sleep stage within PSG. A recent report by the American Academy of Sleep Medicine (AASM) shows that staging of N1 is associated with the highest inter-rater scoring uncertainty of all PSG stages⁶². Furthermore, N1 sleep has proven the most difficult PSG stage to classify from fMRI FC information in machine-learning studies^{18,19}. Addressing the microstructure of N1, a line of evoked response potential-studies have demonstrated a high degree of variability in the cortical processing of external stimuli during early NREM sleep (for reviews, see ref. ^{63,64}). Phenomenologically, the sleep onset period is known to be rather complex, with varying mental content and responsiveness to sensory stimuli^{64,65}, and authors have long argued against the assumed homogeneity found in PSG definitions of N1 sleep, an opposition exemplified by Hori’s proposal of nine stages of early sleep⁴⁵. If PSG-defined N1 does in fact represent a mix of wakefulness and sleep, this would explain why we found the highest range of whole-brain states during this PSG stage. While this primarily serves to underline the common

notion that N1 is unlikely to be a reliable demarcation between wakefulness and sleep, the fact that the data-driven HMM was able to identify a transition module occurring between wakefulness and consolidated sleep (N2 and N3)—represented by whole-brain states characterised by subcortico-cortical decoupling consistent with intracortical evidence of brain activity during sleep onset⁴¹—suggests that an improved and principled categorisation of early sleep could be within reach.

PSG does not differentiate between brain activity prior to and after sleep onset. However, in line with the common subjective experience of grogginess when waking from sleep, behavioural experiments have shown cognitive deficits in the period following awakening. The term sleep inertia is often used to describe this phenomenon⁶⁶. Our results confirm that falling asleep and waking up are two asymmetric processes, leading to two separated transition modules of whole-brain network states during wakefulness, with one more likely to occur after consolidated sleep. Like the N1-related findings discussed above, this too serves as a prime example of how information-rich neuroimaging data, when treated in a data-driven way, can be carefully evaluated in light of established knowledge (PSG in this case) to make new

discoveries from, and categorisations of, brain activity. The presented findings point ahead to a research agenda making hypothesis-driven assessments of how the alternative, data-driven, temporal segmentations and dynamics of whole-brain networks across the NREM sleep cycle relate to sleep-behaviour and cognition, when the latter is measured independently of PSG (see Supplementary Discussion 3). Furthermore, there is scope for HMM explorations with higher temporal detail using electrophysiological modalities, such as magnetoencephalography (MEG) and high-density EEG (see Supplementary Discussion 3).

For further discussion about the reproducibility of our results across different numbers of states, different initialisations of the HMM, and different parcellation schemes, as well as discussion about our choice of data inclusion, pre-processing steps, such as spatial smoothing, and the use of the RETROICOR method to remove physiological signals from the fMRI data, we refer to the Supplementary Discussion 2, Supplementary Notes 1–3, and Supplementary Figures 1, 6–16, and 22–25.

In summary, the work presented here demonstrates how data-driven, temporally sensitive analyses of large-scale fMRI brain activity can be used to explore fundamental changes in behaviour and cognition, in the form of the wake-NREM sleep cycle. The results reveal a higher complexity of brain activity than what traditional sleep scoring—and neuroimaging relying strictly on PSG—can reveal. We projected the traditional stages of wakefulness and NREM sleep onto a probabilistic map of transitions between whole-brain network states. By studying these transitions we have shown a significant decrease in whole-brain dynamics during consolidated stages of NREM sleep; that brain activity prior to sleep is significantly different from just after sleep; that whole-brain network activity do not support traditional criteria to define N1 sleep; and that increased activity in the DMN might serve a gate-function for the entry into NREM sleep. By using fMRI data we have increased the spatiotemporal resolution of traditional NREM sleep stages, using a framework that should be sought expanded to include other fundamental changes in brain activity, such as REM sleep, sleep disorders, anaesthesia and psychedelic experiences. Finally, future work should aim to leverage even finer temporal details through modalities such as MEG and high-density EEG.

Methods

Acquisition and processing of fMRI and PSG data. fMRI was acquired on a 3 T system (Siemens Trio, Erlangen, Germany) with the following settings: 1505 volumes of T2*-weighted echo planar images with a repetition time (TR) of 2.08 s, and an echo time of 30 ms; matrix 64 × 64, voxel size 3 × 3 × 2 mm³, distance factor 50%, FOV 192 mm².

The EPI data were realigned, normalised to MNI space, and spatially smoothed using a Gaussian kernel of 8 mm³ FWHM in SPM8 (<http://www.fil.ion.ucl.ac.uk/spm/>). Spatial downsampling was then performed to a 4 × 4 × 4 mm resolution. From the simultaneously recorded ECG and respiration, cardiac- and respiratory-induced noise components were estimated using the RETROICOR method⁶⁷, and together with motion parameters these were regressed out of the signals. The data were temporally band-pass filtered in the range 0.01–0.1 Hz using a sixth-order Butterworth filter. Please note that the fMRI data were temporally filtered with no consideration of the later established PSG structure of the data. Hence, our findings of relative differences between the various PSG stages should not be affected by these pre-processing steps. We show that this is the case for the temporal filter in Supplementary Figure 16, where the plots of Fig. 3 from the main text have been re-computed for an HMM with 19 states on BOLD data, which had not been temporally filtered.

Simultaneous PSG was performed through the recording of EEG, EMG, ECG, EOG, pulse oximetry and respiration. EEG was recorded using a cap (modified BrainCapMR, EasyCap, Herrsching, Germany) with 30 channels, of which the FCz electrode was used as reference. The sampling rate of the EEG was 5 kHz, and a low-pass filter was applied at 250 Hz. MRI and pulse artefact correction were applied based on the average artefact subtraction method⁶⁸ in Vision Analyzer2 (Brain Products, Germany). EMG was collected with chin and tibial derivations, and as the ECG and EOG recorded bipolarly at a sampling rate of 5 kHz with a low-pass filter at 1 kHz. Pulse oximetry was collected using the Trio scanner, and respiration with MR-compatible devices (BrainAmp MR+, BrainAmp ExG; Brain Products, Gilching, Germany).

Participants were instructed to lie still in the scanner with their eyes closed and relax. Sleep classification was performed by a sleep expert based on the EEG recordings in accordance with the AASM criteria (2007).

Results using the same data and the same preprocessing have previously been reported in ref.¹⁸.

Participants. We used fMRI and PSG data from 57 participants taken from a larger data-base¹⁸. Exclusion criteria focussed on the quality of the concomitant acquisition of EEG, EMG, fMRI and physiological recordings. Written informed consent was obtained, and the study was approved by the ethics committee of the Faculty of Medicine at the Goethe University of Frankfurt, Germany.

Following the HMM decomposition, two different subsets of the solution were used for post hoc evaluation of the HMM. The first corresponded to the 18 participants that reached all four stages of PSG, and the second corresponded to the 31 participants that woke up after having reached consolidated sleep (the WASO group).

HMM general overview. In order to resolve dynamic whole-brain networks in the fMRI signals in a data-driven way, we applied a HMM^{24,27} to timecourses extracted from 90 ROIs defined by the cortical and subcortical areas of the AAL²⁶, however, please see Supplementary Note 1 for a demonstration of the robustness of our results using an alternative parcellation.

We used the FSL (<https://fsl.fmrib.ox.ac.uk/fsl/fslwiki/>) function `fslmeans` to average over voxels within each ROI to get the representative timecourses. The participant-specific sets of 90 ROI-timecourses were demeaned, divided by their standard deviation, and concatenated across participants, yielding a data matrix of dimensions 90 × (57 × 1500), with 1500 samples corresponding to 52 min given a TR of 2.08 s. The HMM inference estimated a number of recurring discrete states, each of which was characterised by a unique configuration of data statistics. We employed a Gaussian HMM, implemented using the Matlab toolbox HMM-MAR (<https://github.com/OHBA-analysis/HMM-MAR>), such that each state was modelled as a multivariate normal distribution with first (mean activity) and second order statistics (covariance matrix). The parameters of the states were defined at the group level, whereas the state timecourses are defined for each subject separately. Therefore, the HMM inference identified periods of time of quasi-stationary activity, where the 90 ROI timecourses could be described by certain configurations of mean activity and FC. The HMM represents a tool for decomposing multivariate data into fewer dimensions. Given the high spatial dimensionality of fMRI, it is common to use principal component analysis (PCA) to reduce the number of parameters to be estimated in the decomposition, increasing the signal-to-noise ratio of the data and improving the robustness of the results^{24,27}. Accordingly, we submitted the demeaned, standardised and concatenated BOLD timecourses to PCA prior to the HMM inference. Keeping approximately 90% of the signal variance, we used the top 25 principal components (see Fig. 1), yielding a data matrix of dimensions 25 × (57 × 1500), which were then fed to the HMM. An overview of the analysis workflow is given in Fig. 1 of the main text. For certain analyses, such as the MANOVA and the test for WASO-specific HMM states, we used subsets of the full set of HMM states.

Choice of number of HMM states. The HMM was implemented with variational Bayes inference, which was used to probabilistically estimate the state statistics and transition probabilities^{24,27}. The number of states of the HMM was a free parameter, which had to be chosen before further evaluation. Determining the number of states present in recordings of spontaneous brain activity is a non-trivial task, which may be approached in a number of ways. We ran the HMM for model orders spanning 4–45, and evaluated each solution by a number of summary statistics, the most important of which are plotted in Supplementary Figure 1.

Supplementary Figure 1a shows the minimum free energy as a function of the HMM model order. The free energy is the statistical measure that is minimised during the (variational inference) Bayesian optimisation process. Technically speaking, it is an approximation of the model evidence, and includes two terms: how well the model fits the data, and the complexity of the model (measured as how much it departs from the prior distribution). Whereas the free energy is a reasonable criterion for choosing the ideal number of states for the HMM, its biological validity remains unclear in so far as the HMM does not represent a biophysical model. As apparent from the plot in Supplementary Figure 1a, the minimum free energy was monotonically decreasing over the large range of tested numbers of states, showing no negative peaks. Hence, like in previous applications of the HMM^{24,27}, the free energy was not informative for choosing the number of states in our case.

We defined fractional occupancy as the temporal proportion of a recording, in which an HMM state was active²⁷. In Supplementary Figure 1c is plotted the development of the median fractional occupancy across HMM states as a function of model order. While the curve decreases rapidly for low values of K , meaning that, as expected, each HMM state on average accounted for less of the total recording time as the number of states was increased, this trend ceased from around $K = 19$. This stagnation for higher model orders was caused by the occurrence of ‘sporadic’ states, which modelled very (participant-) specific subparts of the data (see Supplementary Figure 6). This phenomenon was also reflected in the development of the average HMM state lifetime, which too stabilised around the same value of K , as shown in Supplementary Figure 1d.

To test whether the fMRI-based HMM states showed a significant relationship with the EEG-based sleep scoring, we used a multivariate analysis of variance (MANOVA). The built-in MATLAB function `manova1` provided the summary statistic Wilk's Λ , which described how well the K number of HMM state timecourses could be grouped according to the sleep scoring. In order to test if the relationship was significant, we performed MANOVA's on 1000 permuted cases of the sleep scoring, collecting the Wilk's Λ for each run. Each permutation was constructed, such that the original stage transition points, stage counts, and periods were preserved, while the sleep-stage labelling of each of these periods was shuffled randomly within participants. For each permutation, each participant thus retained the same sleep stages, but the temporal orderings of these were random. Supplementary Figure 1b plots Wilk's Λ as a function of the HMM model order for both the original sleep scoring and the permuted cases. For number of states above $K = 7$, the HMM state timecourses were grouped significantly better by the original compared to the permuted sleep scoring. This result suggests that only when using more than seven states, the HMM identified states with a significant dependency on the PSG scoring.

The results in Supplementary Figure 1b–d are computed from a subset of the HMM solutions corresponding to the participants including all four available PSG stages (18 participants with: wakefulness, N1 sleep, N2 sleep, and N3, see right part of Supplementary Table 1). This was done to minimise the unevenness in the representation of PSG stages. Based on the evaluations above, we concluded that the HMM was able to, in data-driven fashion, estimate the temporal structure given by the EEG-based sleep scoring for model orders above 7. We chose $K = 19$ states, because increasing the number of states above this point mainly resulted in the addition of HMM states of low-fractional occupancy and participant-specific occurrences.

Significance testing. In order to evaluate the PSG-sensitivity and -specificity, we used paired t tests to test for significant differences within the HMM states. As such, with the original PSG stages, we compared the sensitivity and the specificity, respectively, for W, N1, N2 and N3 within each HMM state for the 18 participants that included all of these four stages. This yielded six comparisons within each HMM state (W-vs.-N1, W-vs.-N2, W-vs.-N3, N1-vs.-N2, N1-vs.-N3, N2-vs.-N3), for both the sensitivity and specificity measures, and each of these comparisons was associated with a t -statistic. To test if these t -statistics were larger than random, we used permutation testing as explained above (see section Choice of number of HMM states), where the EEG-based sleep scoring vector was permuted 1000 times with number of PSG stages and periods kept constant, but with their temporal order randomly shuffled within each participant. We computed the PSG-sensitivity and -specificity for each permutation and performed paired t tests for every case. The resulting t -statistics were used to build null-distributions, and the original t -statistics were compared against these to get p values for the original tests. The bar plots of PSG-sensitivity and -specificity in Fig. 3a, b of the main text include line crossbars indicating the cases with p values < 0.01 (paired t tests with permutations). Please note that the use of paired t tests ensured that the identified differences were consistent within participants, and not merely as a group effect.

We evaluated the hypothesis that certain HMM states had higher activity in periods of wakefulness after sleep onset (WASO) by considering the subgroup of participants that, according to PSG scoring, woke up after having reached N2 sleep. This corresponded to 31 participants, and we defined WASO as polysomnographically estimated periods of wakefulness that followed N2 sleep. From here we followed the same steps outlined above for the original PSG stages, and the results are shown in Supplementary Figure 2.

To test for differences in the measures of dynamics, amount of switching and range of HMM states, we also employed paired t tests and the permutation scheme explained above to establish chance levels.

Analysis and visualisation of HMM transitions. The matrix of transition probabilities, which were explicitly modelled by the HMM, contained a clear organisation, in which subnetworks of HMM states expressed more frequent transitions within each other than to states outside. In other words, the transition matrix represented a directed graph with modular organisation. We demonstrated this by submitting the transition matrix (shown in Fig. 4a) to a modularity analysis, using Matlab functions from the Brain Connectivity Toolbox (<https://sites.google.com/site/bctnet/Home>)⁶⁹, based on Newman's spectral community detection⁷⁰. Prior to running the modularity algorithm, we excluded the transitions of the HMM states that did not occur consistently across participants, i.e., sporadic states (see Methods, Choice of number of states, and Fig. 4b), and thresholded the remaining transition matrix to include the strongest elements. The choice of this latter threshold was done for visualisation purposes (for the results shown in the main text using 19 states we included the 21% strongest transitions), however, different thresholds resulted in highly similar module partitions. The modular organisation is presented in a reordered matrix (Fig. 4c) and as a map (Fig. 4d).

Visualising mean activation maps of HMM states. The mean activation maps have been overlaid on brain surfaces in Figs. 5 and 6 of the main text, using the Human Connectome Project software Connectome Workbench (<https://www.humanconnectome.org/software/connectome-workbench>). The HMM was inferred in volumetric MNI152 space and mapped to the surface of the Conte-69 template using the Workbench function `wb_command -volume-to-surface-mapping`. The presented

surface maps are shown with the 50% strongest increases and the 50% strongest decreases in activation for each HMM state relative to baseline averaged over all HMM states.

Data availability

The datasets generated during and/or analysed during as well as code used during the current study are available from the corresponding author on reasonable request.

Received: 23 February 2018 Accepted: 11 February 2019

Published online: 04 March 2019

References

- Laureys, S., Perrin, F. & Bredart, S. Self-consciousness in non-communicative patients. *Conscious. Cogn.* **16**, 722–741 (2007).
- Iber, C., Ancoli-Israel, S., Chesson, A. & Quan, S. F. *The AASM Manual for the Scoring of Sleep and Associated Events: Rules, Terminology and Technical Specifications* (American Academy of Sleep Medicine, Westchester, IL, 2007).
- Loomis, A. L., Harvey, E. N. & Hobart, G. Potential rhythms of the cerebral cortex during sleep. *Science* **81**, 597–598 (1935).
- Himanan, S. L. & Hasan, J. Limitations of Rechtschaffen and Kales. *Sleep. Med. Rev.* **4**, 149–167 (2000).
- Ogilvie, R. D. & Wilkinson, R. T. The detection of sleep onset: behavioral and physiological convergence. *Psychophysiology* **21**, 510–520 (1984).
- Bonnet, M. H. & Moore, S. E. The threshold of sleep: perception of sleep as a function of time asleep and auditory threshold. *Sleep* **5**, 267–276 (1982).
- Manconi, M. et al. Measuring the error in sleep estimation in normal subjects and in patients with insomnia. *J. Sleep Res.* **19**, 478–486 (2010).
- Edinger, J. D., Ulmer, C. S. & Means, M. K. Sensitivity and specificity of polysomnographic criteria for defining insomnia. *J. Clin. Sleep. Med.* **9**, 481–491 (2013).
- Raichle, M. E. Two views of brain function. *Trends Cogn. Sci.* **14**, 180–190 (2010).
- Smith, S. M. et al. Correspondence of the brain's functional architecture during activation and rest. *Proc. Natl Acad. Sci. USA* **106**, 13040–13045 (2009).
- Deco, G., Jirsa, V. K. & McIntosh, A. R. Emerging concepts for the dynamical organization of resting-state activity in the brain. *Nat. Rev. Neurosci.* **12**, 43–56 (2011).
- Woolrich, M. W. & Stephan, K. E. Biophysical network models and the human connectome. *Neuroimage* **80**, 330–338 (2013).
- Maquet, P. Functional neuroimaging of normal human sleep by positron emission tomography. *J. Sleep Res.* **9**, 207–231 (2000).
- Dang-Vu, T. T. et al. Functional neuroimaging insights into the physiology of human sleep. *Sleep* **33**, 1589–1603 (2010).
- Sämman, P. G. et al. Development of the brain's default mode network from wakefulness to slow wave sleep. *Cereb. Cortex* **21**, 2082–2093 (2011).
- Spoormaker, V. I. et al. Development of a large-scale functional brain network during human non-rapid eye movement sleep. *J. Neurosci.* **30**, 11379–11387 (2010).
- Larson-Prior, L. J. et al. Cortical network functional connectivity in the descent to sleep. *Proc. Natl Acad. Sci. USA* **106**, 4489–4494 (2009).
- Tagliazucchi, E. & Laufs, H. Decoding wakefulness levels from typical fMRI resting-state data reveals reliable drifts between wakefulness and sleep. *Neuron* **82**, 695–708 (2014).
- Altman, A. et al. Validation of non-REM sleep stage decoding from resting state fMRI using linear support vector machines. *Neuroimage* **125**, 544–555 (2016).
- Boly, M. et al. Hierarchical clustering of brain activity during human nonrapid eye movement sleep. *Proc. Natl Acad. Sci. USA* **109**, 5856–5861 (2012).
- Tagliazucchi, E. et al. Large-scale brain functional modularity is reflected in slow electroencephalographic rhythms across the human non-rapid eye movement sleep cycle. *Neuroimage* **70**, 327–339 (2013).
- Brodbeck, V. et al. EEG microstates of wakefulness and NREM sleep. *Neuroimage* **62**, 2129–2139 (2012).
- Haimovici, A., Tagliazucchi, E., Balenzuela, P. & Laufs, H. On wakefulness fluctuations as a source of BOLD functional connectivity dynamics. *Sci. Rep.* **7**, 5908 (2017).
- Vidaurre, D., Smith, S. M. & Woolrich, M. W. Brain network dynamics are hierarchically organized in time. *Proc. Natl Acad. Sci. USA* **114**, 12827–12832 (2017).
- Preti, M. G., Bolton, T. A. W. & Ville, D. V. D. The dynamic functional connectome: state-of-the-art and perspectives. *NeuroImage* **160**, 41–54 (2017).
- Tzourio-Mazoyer, N. et al. Automated anatomical labeling of activations in SPM using a macroscopic anatomical parcellation of the MNI MRI single-subject brain. *Neuroimage* **15**, 273–289 (2002).

27. Vidaurre, D. et al. Discovering dynamic brain networks from big data in rest and task. *Neuroimage* **180**(Pt 4), 646–656 (2018).
28. Balkin, T. J. et al. The process of awakening: a PET study of regional brain activity patterns mediating the re-establishment of alertness and consciousness. *Brain* **125**, 2308–2319 (2002).
29. Raichle, M. E. et al. A default mode of brain function. *Proc. Natl Acad. Sci. USA* **98**, 676–682 (2001).
30. Fox, M. D. et al. The human brain is intrinsically organized into dynamic, anticorrelated functional networks. *Proc. Natl Acad. Sci. USA* **102**, 9673–9678 (2005).
31. Buckner, R. L., Andrews-Hanna, J. R. & Schacter, D. L. The brain's default network: anatomy, function, and relevance to disease. *Ann. N. Y. Acad. Sci.* **1124**, 1–38 (2008).
32. Spreng, R. N., Mar, R. A. & Kim, A. S. The common neural basis of autobiographical memory, prospection, navigation, theory of mind, and the default mode: a quantitative meta-analysis. *J. Cogn. Neurosci.* **21**, 489–510 (2009).
33. Fox, M. D., Corbetta, M., Snyder, A. Z., Vincent, J. L. & Raichle, M. E. Spontaneous neuronal activity distinguishes human dorsal and ventral attention systems. *Proc. Natl Acad. Sci. USA* **103**, 10046–10051 (2006).
34. Koehlin, E. & Summerfield, C. An information theoretical approach to prefrontal executive function. *Trends Cogn. Sci.* **11**, 229–235 (2007).
35. Menon, V. & Uddin, L. Q. Saliency, switching, attention and control: a network model of insula function. *Brain Struct. Funct.* **214**, 655–667 (2010).
36. Tagliazucchi, E. et al. Breakdown of long-range temporal dependence in default mode and attention networks during deep sleep. *Proc. Natl Acad. Sci. USA* **110**, 15419–15424 (2013).
37. Ferrara, M. et al. The electroencephalographic substratum of the awakening. *Behav. Brain Res.* **167**, 237–244 (2006).
38. Tsai, P. J. et al. Local awakening: regional reorganizations of brain oscillations after sleep. *Neuroimage* **102**(Pt 2), 894–903 (2014).
39. Braun, A. R. et al. Regional cerebral blood flow throughout the sleep-wake cycle. An H2(15)O PET study. *Brain* **120**(Pt 7), 1173–1197 (1997).
40. Baker, R. et al. Altered activity in the central medial thalamus precedes changes in the neocortex during transitions into both sleep and propofol anesthesia. *J. Neurosci.* **34**, 13326–13335 (2014).
41. Magnin, M. et al. Thalamic deactivation at sleep onset precedes that of the cerebral cortex in humans. *Proc. Natl Acad. Sci. USA* **107**, 3829–3833 (2010).
42. Schabus, M. et al. Hemodynamic cerebral correlates of sleep spindles during human non-rapid eye movement sleep. *Proc. Natl Acad. Sci. USA* **104**, 13164–13169 (2007).
43. Caporro, M. et al. Functional MRI of sleep spindles and K-complexes. *Clin. Neurophysiol.* **123**, 303–309 (2012).
44. Werth, E., Achermann, P. & Borbély, A. A. Fronto-occipital EEG power gradients in human sleep. *J. Sleep Res.* **6**, 102–112 (1997).
45. Hori, T. et al. Proposed supplements and amendments to 'a manual of standardized terminology, techniques and scoring system for sleep stages of human subjects', the Rechtschaffen & Kales (1968) standard. *Psychiatry Clin. Neurosci.* **55**, 305–310 (2001).
46. Olbrich, E. & Achermann, P. Analysis of oscillatory patterns in the human sleep EEG using a novel detection algorithm. *J. Sleep Res.* **14**, 337–346 (2005).
47. Abeysuriya, R. G. & Robinson, P. A. Real-time automated EEG tracking of brain states using neural field theory. *J. Neurosci. Methods* **258**, 28–45 (2016).
48. Picchioni, D. et al. fMRI differences between early and late stage-1 sleep. *Neurosci. Lett.* **441**, 81–85 (2008).
49. Watanabe, T. et al. Network-dependent modulation of brain activity during sleep. *Neuroimage* **98**, 1–10 (2014).
50. Tagliazucchi, E. & van Someren, E. J. W. The large-scale functional connectivity correlates of consciousness and arousal during the healthy and pathological human sleep cycle. *Neuroimage* **160**, 55–72 (2017).
51. Tononi, G. Consciousness as integrated information: a provisional manifesto. *Biol. Bull.* **215**, 216–242 (2008).
52. Tononi, G., Edelman, G. M. & Sporns, O. Complexity and coherency: integrating information in the brain. *Trends Cogn. Sci.* **2**, 474–484 (1998).
53. Marshall, W., Gomez-Ramirez, J. & Tononi, G. Integrated information and state differentiation. *Front. Psychol.* **7**, 926 (2016).
54. Casali, A. G. et al. A theoretically based index of consciousness independent of sensory processing and behavior. *Sci. Transl. Med* **5**, 198ra105 (2013).
55. Carhart-Harris, R. L. et al. The entropic brain: a theory of conscious states informed by neuroimaging research with psychedelic drugs. *Front. Hum. Neurosci.* **8**, 20 (2014).
56. Tagliazucchi, E., Carhart-Harris, R., Leech, R., Nutt, D. & Chialvo, D. R. Enhanced repertoire of brain dynamical states during the psychedelic experience. *Hum. Brain Mapp.* **35**, 5442–5456 (2014).
57. Tagliazucchi, E., Crossley, N., Bullmore, E. T. & Laufs, H. Deep sleep divides the cortex into opposite modes of anatomical–functional coupling. *Brain Struct. Funct.* **221**, 4221–4234 (2016).
58. Littner, M. et al. Practice parameters for using polysomnography to evaluate insomnia: an update. *Sleep* **26**, 754–760 (2003).
59. Larson-Prior, L. J., Ju, Y. E. & Galvin, J. E. Cortical–subcortical interactions in hypersomnia disorders: mechanisms underlying cognitive and behavioral aspects of the sleep–wake cycle. *Front. Neurol.* **5**, 165 (2014).
60. Wei, Y. et al. Sleep stage transition dynamics reveal specific stage 2 vulnerability in insomnia. *Sleep* **40**, zsx117 (2017).
61. Carskadon, M. A. & Dement, W. C. in *Principles and Practice of Sleep Medicine* 5th edn (eds Kryger, M. H., Roth T. & Dement, W. C.) Ch. 2 (W.B. Saunders, Elsevier, Philadelphia, 2011).
62. Rosenberg, R. S. & Van Hout, S. The American Academy of Sleep Medicine inter-scoring reliability program: sleep stage scoring. *J. Clin. Sleep. Med.* **9**, 81–87 (2013).
63. Colrain, I. M. & Campbell, K. B. The use of evoked potentials in sleep research. *Sleep Med. Rev.* **11**, 277–293 (2007).
64. Ogilvie, R. D. The process of falling asleep. *Sleep Med. Rev.* **5**, 247–270 (2001).
65. Goupil, L. & Bekinschtein, T. A. Cognitive processing during the transition to sleep. *Arch. Ital. Biol.* **150**, 140–154 (2012).
66. Tassi, P. & Muzet, A. Sleep inertia. *Sleep Med. Rev.* **4**, 341–353 (2000).
67. Glover, G. H., Li, T. Q. & Ress, D. Image-based method for retrospective correction of physiological motion effects in fMRI: RETROICOR. *Magn. Reson. Med.* **44**, 162–167 (2000).
68. Allen, P. J., Polizzi, G., Krakow, K., Fish, D. R. & Lemieux, L. Identification of EEG events in the MR scanner: the problem of pulse artifact and a method for its subtraction. *Neuroimage* **8**, 229–239 (1998).
69. Rubinov, M. & Sporns, O. Complex network measures of brain connectivity: uses and interpretations. *Neuroimage* **52**, 1059–1069 (2010).
70. Leicht, E. A. & Newman, M. E. J. Community structure in directed networks. *Phys. Rev. Lett.* **100**, 118703 (2008).

Acknowledgements

G.D. was supported by the Spanish Research Project PSI2016-75688-P (AEI/FEDER) and by the European Union's Horizon 2020 research and innovation programme under Grant agreement no. 720270 (HBP SGA1). M.L.K. was supported by the ERC Consolidator Grant CAREGIVING (615539) and the Center for Music in the Brain, funded by the Danish National Research Foundation Grant DNRF117. J.C. was supported under the project NORTE-01-0145-FEDER-000023. The authors would like to thank Martin Dietz for his inputs regarding the hemodynamic response function convolution.

Author contributions

H.L. oversaw data acquisition. E.T., A.B.A.S. and D.V. preprocessed the data. A.B.A.S., M.L.K., D.V., S.F.V.N. and M.W. conceptualised the data analyses. A.B.A.S., D.V., M.L.K. and K.R. analysed the data. A.B.A.S., D.V. and M.L.K. wrote the manuscript. A.B.A.S., D.V., M.L.K., M.W., G.D., E.V.S., P.V., J.C., H.L., E.T., S.F.V.N. and K.R. edited the manuscript.

Additional information

Supplementary Information accompanies this paper at <https://doi.org/10.1038/s41467-019-08934-3>.

Competing interests: The authors declare no competing interests.

Reprints and permission information is available online at <http://npg.nature.com/reprintsandpermissions/>

Journal peer review information: *Nature Communications* thanks the anonymous reviewers for their contribution to the peer review of this work. Peer reviewer reports are available.

Publisher's note: Springer Nature remains neutral with regard to jurisdictional claims in published maps and institutional affiliations.

 **Open Access** This article is licensed under a Creative Commons Attribution 4.0 International License, which permits use, sharing, adaptation, distribution and reproduction in any medium or format, as long as you give appropriate credit to the original author(s) and the source, provide a link to the Creative Commons license, and indicate if changes were made. The images or other third party material in this article are included in the article's Creative Commons license, unless indicated otherwise in a credit line to the material. If material is not included in the article's Creative Commons license and your intended use is not permitted by statutory regulation or exceeds the permitted use, you will need to obtain permission directly from the copyright holder. To view a copy of this license, visit <http://creativecommons.org/licenses/by/4.0/>.

© The Author(s) 2019

Supplementary Information for the manuscript:

Discovery of key whole-brain transitions and dynamics during human wakefulness and non-REM sleep

Stevner, A.B.A. et al.

Supplementary Discussion 1

The HMM was sensitive to recurrent changes in both mean BOLD activity and FC, and the overall reflection of PSG stages in the whole-brain network states, seen also from the MANOVA results, suggests that these two features of brain activity changed reliably with PSG stages. This is in line with previous PET ^{1, 2, 3, 4} and fMRI ^{5, 6, 7} studies that have regressed PSG stages onto neuroimaging data to show differences between individual PSG stages in metabolic and BOLD activity, an EEG study showing PSG-dependent changes in EEG microstates ⁸, demonstrations that machine-learning can be used to classify fMRI recordings into PSG stages based only on FC patterns ^{9, 10, 11}, and most recently the study by Haimovici and colleagues demonstrated that PSG stages could be identified as individual states of dynamic FC ¹².

We found high-order RSNs, i.e. the DMN and the ACN, to occur relatively exclusively during wakefulness. However, previous investigations have suggested a rather ubiquitous presence of both the DMN and the ACN, not just in wakefulness but, in all stages of NREM sleep ^{6, 13, 14, 15}. These studies were based on static FC analyses of PSG-defined sleep stages, using both seed-based correlations ^{6, 13, 14, 15} and spatial ICA ¹⁶, and the seeming lack of sensitivity to changes in vigilance has raised questions about the relevance of these RSNs for on-going cognition ¹⁷. Our results contribute to this debate, by suggesting a clear wakefulness-specificity of the DMN and the ACN in terms of mean activation, but not in FC (see also Supplementary Note 5).

Two HMM states were clearly specific to periods of N2 sleep. The corresponding mean activation maps showed either increases or decreases in areas consistently identified in a number of studies as fMRI-correlates of sleep spindles ^{18, 19, 20}. We tested the temporal relationships between the data-driven HMM states and the occurrence of sleep spindles, as identified in the EEG (see Supplementary Figures 19–20 and Supplementary Note 4), and indeed we found HMM states 3 and 6 to account for the majority of time where sleep spindles were present. However, the same was true for K-complexes. When identifying K-complexes from the EEG and comparing their occurrences with the HMM states, we once again found HMM states 3 and 6 accounting for the majority (see Supplementary Figures 19 and 21). In line with previous studies investigating the effects of spindles and K-complexes on the BOLD signal ^{18, 20, 21} we also looked at the temporal relationships to the HMM states after convolving the sleep graphoelements with the canonical hemodynamic response function (HRF, see Methods and Supplementary Figure 19 for illustration).

This led to an increase in the correlation and specificity values of the HMM states compared to when the raw non-convolved occurrences of spindles and K-complexes were used, but overall did not change the differences on these scores between the states. HMM states 3 and 6 still accounted for the majority of the HRF-convolved sleep spindles and K-complexes. Within HMM states 3 and 6 we did not find marked differences in their relationship to the graphoelements. Both with and without the HRF convolution HMM state 3 tended to show higher correlation and specificity values than HMM state 6 for both spindles and K-complexes, although these differences did not survive correction for multiple comparisons, as shown in Supplementary Figures 20 and 21. The theoretical scenario that the two HMM states (3 and 6), accounting for the majority of N2 sleep, might represent direct reflections of different sleep graphoelements does thus not seem to be supported. Rather, both of these HMM states included each of their share of both spindles and K-complexes. In light of previous event-related demonstrations of robust effects of sleep graphoelements on the BOLD signal^{18, 19, 20, 21, 22}, as well as the similarity between these event-related patterns and the mean activation maps of HMM states 3 and 6, it seems unlikely that spindles and K-complexes did not influence the HMM state description, however this did not result in any HMM state coding exclusively for one or the other graphoelement. There is of course the possibility that HMM states 3 and 6 are suggesting a categorisation of spindles and K-complexes beyond what the scalp EEG is able to resolve, or at least beyond the classical interpretation of these graphoelements. Future mapping of the spectral and spatial properties of these graphoelements at higher resolutions than the AASM criteria, that were used here, could bring more insights in this regard, as could a combination or comparison with intracortical evidence^{23, 24, 25}.

There is growing evidence that neuroimaging timecourses contain long-range temporal dependencies^{26, 27, 28}, i.e. they are non-Markovian²⁹. The HMM used here follows the Markovian assumption in the sense that the probability of a state transition at a given time point depends only on the state that is active at the preceding time point, and hence it does not parametrically model long-range temporal dependencies. Importantly, however, it does not preclude them either. This means that the HMM state timecourses can in fact exhibit non-Markovian dynamics and long-term dependencies; see e.g.³⁰. Notably, our finding of HMM states grouping into modules of transitions represents an analysis that goes beyond Markovianity, and demonstrates non-Markovian dynamics (i.e. long-term dependencies) at the system level of the HMM states. In light of this, our finding that N3 sleep was modelled almost exclusively by a single HMM state, while several states grouped into modules during wakefulness, is in line with the study by Tagliazucchi and colleagues, showing that long-range temporal dependencies in fMRI signals decreases from wakefulness to N3 sleep¹⁶.

Supplementary Discussion 2

Methodological considerations

For the HMM analysis we chose to make use of the full dataset of 57 participants, when inferring the states. Subsequently we analysed the part of the HMM solution that corresponded to the 18 participants that included all PSG stages. We chose to include as much data as possible for the initial inference in order to maximise the signal-to-noise ratio and amount of evidence for the HMM parameter estimation. Yet, as it is clear from Supplementary Table 1, the full dataset included rather uneven distributions of PSG stages. While PSG stages are more evenly distributed in the subset of 18 participants, and we diligently made sure to normalise the relevant summary measures by number of samples of PSG stages within participants, there still exists a possibility that the HMM could be biased by having more data available from certain PSG stages than others, even if the HMM remained uninformed of the PSG staging. For instance, one could imagine that more data from a certain PSG stage would lead to more HMM states per time being assigned to data from that PSG stage. Such an effect is not immediately present in our results, however, since for instance we found both switching and range of HMM states to be higher in N1 sleep, even though the original full dataset included more than twice as much data from wakefulness (see Supplementary Table 1 and Figure 3d–e).

The number of HMM states was set to 19 in our analyses based on an evaluation of a range of HMM solutions with varying numbers of states (see Methods). It is important to note, however, that it is difficult to determine a ‘correct’ number of states, when decomposing continuous recordings of brain activity. The recent study by Haimovici and colleagues aimed to identify individual FC states for each PSG stage, and thus chose 4 states for their sliding-window analysis¹². Our aim was to extract as much temporal resolution as possible from the BOLD ROI timecourses. Ideally, a higher number of states should provide more temporal detail, however increasing the number of states above 19 was associated with a higher occurrence of ‘sporadic’ HMM states, modelling very specific subparts of the data and not generalising across participants (see Methods and Supplementary Note 3). Based on this it is important to emphasise that we do not suggest the number 19 as definitive, but simply a tool to resolve as much temporal information as possible from the current dataset.

It should be noted that the HMM framework was chosen over other methods for extracting dynamic states from multivariate neuroimaging datasets, such as sliding-window clustering^{12, 31, 32}, point-

process analysis³³, and co-activation pattern analysis^{34, 35} (for reviews, see^{36, 37}). The employed HMM framework has been successfully applied to resting state data of wakefulness in both MEG^{38, 39, 40} and fMRI^{30, 41}, and was particularly suitable for our purpose by virtue of its explicit modelling of temporal dynamics, resulting in states that repeat in a predictable way. Although the HMM is not a mechanistic model of brain activity (a limitation shared with the alternative approaches mentioned above) we have shown how the explicitly modelled HMM transition matrix was fundamental to suggest new partitions of dynamic whole-brain states, which future mechanistic frameworks of NREM sleep and wakefulness should take into account^{42, 43, 44, 45}.

Sleep is of course a process associated with profound physiological changes, not merely those reflected in brain activity⁴⁶. Despite our use of the RETROICOR method to reduce the effects on the fMRI data of cardiac and respiratory signals (see Methods), it is currently not possible to completely isolate the neural effects of sleep in fMRI. Our results hence share the limitation with other neuroimaging studies of sleep of potentially being influenced by physiological changes not directly linked to brain activity. On the other hand, certain sleep-dependent peripheral changes such as those of the autonomic nervous system will also induce genuine activities in the brain, which in future studies would be important to investigate and with the proper recordings could potentially be evaluated within an HMM framework.

In addition, it should be noted that there could be potentially confounding effects of spatially smoothing the fMRI data, which can create artificial dependencies between regions of interest. In the context of the HMM, which focuses on the aspects of the data that represent more variance, this confound is however likely to be minor.

Another potential caveat of our analyses pertains to the initialisation of the HMM, which is not deterministic. In Supplementary Note 2, we provide a summary analysis showing that the HMM infers consistent states across independent initialisations and splits of data (see Supplementary Figure 16)

Supplementary Discussion 3

Perspectives

Features identified by the HMM could prove to be essential supplements to PSG and other conventional methods when trying to understand phenomena like the subjective perception of sleep^{47, 48}, mental content during sleep^{49, 50}, such as the hypnagogic or even hallucinogenic character of

sleep onset ^{51, 52}, sleep inertia of the awakening process ⁵³, sleep-dependent processes related to memory and learning ⁵⁴, and disordered sleep, like insomnia ⁵⁵. Such studies should explore the theoretical potential of applying the current HMM, parameterised on the present sleep fMRI data, to identify the presence of the same dynamical whole-brain network states and transition modules in data from different cohorts, potentially even at the individual level. This new data could then be linked to behaviour and cognition through sophisticated measures of arousal, such as eyelid-closure ⁵⁶, sleep mentation ⁴⁹, post-sleep memory- and learning performance ⁵⁷, and careful clinical examination of sleep disorders ^{58, 59, 60}.

The wake-NREM sleep cycle merely represents a sub-part of a continuum of activities that the brain supports. Other important brain processes should be sought integrated with the presented transition map (Figure 7), most obviously including REM sleep, but also other altered states of consciousness, such as anaesthesia ^{61, 62, 63}, the psychedelic experience ⁶⁴, and even different contents of consciousness during wakefulness ⁶⁵.

Finally, there is scope for an even more detailed examination of sleep within the HMM framework, given that BOLD data is not the most temporally sensitive modality available. Recently developed methods combining the HMM framework with source-reconstructed MEG data could prove capable of providing an even more fine-grained picture of sleep's evolution in whole-brain networks, and allow for an examination of microstructural EEG elements of sleep, such as spindles and K-complexes ^{38, 39, 40, 66}, as well as EEG-markers of vigilance fluctuations during wakefulness ⁶⁷.

Supplementary Note 1

Robustness across different parcellations

We chose the AAL over other possible parcellations because it is the most frequently used in previous fMRI studies of FC during NREM sleep ^{15, 16, 17, 18, 19, 20}. Alternative parcellations, such as those derived from FC configurations in the data, could be problematic, since FC has been shown to robustly vary across the sleep cycle ^{9, 10, 11}. Being anatomically defined, the AAL is essentially agnostic to potentially changing FC configurations within the data. In order to make sure that the use of the HMM generalises to different levels of spatial granularity and that the interpretation following from our results were not specific to the use of the AAL atlas, we re-ran the HMM with a different parcellation. While the field of proposed parcellations for large-scale neuroimaging is rapidly expanding ⁶⁸, we opted for the Brainnetome atlas, originally published by Fan and colleagues ⁶⁹. Unlike many of the most popular parcellation schemes, the Brainnetome is not solely

derived from fMRI FC, but also depends on structural connectivity information for its partitioning of the brain volume. As mentioned above, the use of an FC-derived atlas could bias results, since FC has a well-established dependence on vigilance. Another advantage of the Brainnetome is that it, like the AAL, includes sub-cortical regions, which, as shown in the Results and Discussion of the main text, undergo important changes in activity across NREM sleep. Finally, the 246 regions of the Brainnetome atlas compared to the 90 regions of the AAL provides a good test for the robustness of the HMM across different levels of spatial granularity.

We followed exactly the same steps as explained in the Methods section, but extracted ROI timecourses from the Brainnetome atlas instead of the AAL. It became clear that the increase in spatial detail, going from the AAL to the Brainnetome, had an impact on the ability of the HMM to track the sleep scoring. As such, when using 90% of the variance from the PCA on the Brainnetome ROI timecourses (Figure 1), the performance of the HMM, as quantified through MANOVA between the resulting HMM state timecourses and the sleep scoring, was inferior to the original results using the AAL (see Supplementary Figure 22). However, a slightly stronger regularisation of the ROI timecourses, using only 85% of the variance from the PCA, made the results from the Brainnetome highly comparable to the original results using the AAL. At 85% of the variance the HMM on the Brainnetome data performed in a very similar fashion to the HMM on the 90% of the AAL data, in terms of MANOVA and the development of median fractional occupancy across number of HMM states (see Supplementary Figure 22b and c). The difference between using 90% and 85% of the variance was importantly also evident in the number of HMM states that were consistent across participants for a given HMM solution ($K = 19$, see Supplementary Figure 22d). For 90% of the variance, only 6 HMM states occurred in more than 25% of the participants, whereas this number increased to 12, when 85% of the variance was used. In Supplementary Figure 23 we have re-constructed Figure 3 of the main text, but with the results using 19 HMM states on 85% of the variance of the Brainnetome data. The results are highly consistent, with individual HMM states showing sensitivity and specificity to different sleep stages, and in terms of the differences in dynamics found between sleep stages. Regarding the spatial configuration of the HMM states resulting from the Brainnetome data, these were also highly consistent with the original HMM states using the AAL. This is illustrated in Supplementary Figures 24 and 25, where we have matched HMM states from the Brainnetome to the original HMM states, based on their specificity profiles to sleep stages and spatial patterns.

Overall, the above analysis shows that increasing the spatial granularity by introducing a different parcellation comes at the cost at decreasing the signal-to-noise ratio on the HMM estimation. However when this is controlled through PCA, results can be brought to convergence.

Supplementary Note 2

Robustness across different HMM initialisations

The initialisation of the HMM includes a stochastic element. To make sure that the states inferred by the HMM were not contingent on the initialisation, we ran the HMM with 19 states an additional four times on the full dataset ($N = 57$), and five times on each of the two half-splits of the data ($N = 29$ and $N = 28$). The 19 resulting states of each HMM repetition were matched to the states of the original HMM. Each state of a repetition was thus paired to an original HMM state, based on the similarity between their respective Gaussian distributions. The similarity was estimated using the Bhattacharyya distance⁷⁰, and the matching of states across repetitions were carried out using the Munkres algorithm⁷¹.

Following the pairing of states, all resulting states were compared in an all-to-all manner, again using the Bhattacharyya distance as a measure of similarity. The resulting matrix $[(n_{\text{dataset}} + n_{\text{states}} + n_{\text{repetitions}}) \times (n_{\text{dataset}} + n_{\text{states}} + n_{\text{repetitions}})]$ is shown in Supplementary Figure 15a. The common pattern in the data-set-specific sub-matrices indicates that consistent HMM-state distributions were inferred across initialisation repetitions and data-splits.

Following the matching of the HMM Gaussian distributions from independent initialisations, we tested the temporal correspondence between the original HMM states and their counterparts from the repetition runs. This was done by comparing the corresponding state timecourses. For a pair of HMM states (one original and one from a repetition run) the temporal correspondence was quantified as the ratio between time points of overlap (simultaneous activity or inactivity) and time points of misses (off-sets of activity or inactivity). In Supplementary Figure 15b are plotted the mean values and standard deviations within data-splits, and it is clear that temporal overlaps outweighed misses for all runs of the HMM. This is an important indication that the evaluations of the HMM dynamics presented in the main text would be highly similar for other initialisations.

Supplementary Note 3

Varying the number of HMM states

In appreciation of the potential limitations related to choosing the number of HMM states with no strict, formal criterion, we include the results of using different numbers of HMM states. In Supplementary Figures 7 to 10 we have reproduced Figure 3 of the main text with HMM results using 15, 17, 21, and 23 states respectively. Demonstrating the robustness of our HMM findings,

the conclusions of the main text using 19 states are also found in Supplementary Figures 7 to 10. Specifically Supplementary Figures 7a-b to 10a-b show how select HMM states expressed high sensitivity and specificity for different PSG stages. In line with the results for $K = 19$ states, the HMM with lower and higher K identified states with high sensitivity and specificity for wakefulness, N2, and N3 sleep, but not for N1 sleep. Supplementary Figures 7d-e to 10d-e quantify the dynamics of HMM states within PSG stages. The relative differences between PSG stages are conserved and highly stable across numbers of HMM states. Interestingly, the absolute values of switching between and range of HMM states within PSG stages were in fact also quite preserved across numbers of HMM states. This is likely caused by the fact that the main effect of changing the number of HMM states is an addition of non-recurring, ‘sporadic’, states that modelled very (participant-) specific periods of the fMRI data (see Methods and Supplementary Discussion 2).

Another main result of this study is presented in the transition map of the HMM states (see Figure 4 of the main text). Again we have re-produced equivalent figures for $K = 15, 17, 21,$ and 23 HMM states (Supplementary Figures 11 to 14). Our modularity analysis (see below) of the resulting transition matrices illustrates how the four modules from the HMM with 19 states can be identified in the solutions with different numbers of states. This was true for $K = 17, 21,$ and 23 . For $K = 15$, the white and blue modules appear to have merged together. The overall structure of the transition map was therefore robust across the chosen numbers of HMM states. A separate transition module for wakefulness after sleep onset (WASO) was found consistently across all of these values of K , while the intercalated module between wakefulness and consolidated sleep (N2/N3) were found for all but one value of K ($K = 15$).

Whereas these overall configurations of the HMM transitions were found robust to the chosen number of states, the more fine-grained details of the transition map appeared more variable. The gateway-like quality of a DMN-like configuration of brain activity was thus particularly clear for the originally chosen 19 states.

Supplementary Note 4

Relationship between HMM states and sleep graphoelements

In order to determine the effect of micro-structural features in the sleep EEG, (sleep graphoelements) on the HMM states we used information on the occurrence of sleep spindles and K-complexes during the fMRI recordings. The procedure for obtaining this information from the EEG for the present data has previously been described in Jahnke et al. ²¹. Briefly, sleep graphoelements were manually identified according to the criteria set out in the AASM guidelines

⁷². This included the use of an EEG montage with frontal, central, and occipital electrodes referenced to the contra-lateral mastoid electrodes (TP9, TP10). The resulting temporal markings of sleep spindles and K-complexes were re-sampled to the sampling frequency of the fMRI acquisition (TR = 2.08 seconds) and collected in the variables SS-timecourse and KC-timecourse (for illustration of the SS- and KC-timecourse in an example participant, see Supplementary Figure 19). To account for the delay in the BOLD response, we also created versions of the SS- and KC-timecourses convoluted with the canonical hemodynamic response function (HRF). We used the HRF included in the SPM12 function `spm_hrf.m` (<http://www.fil.ion.ucl.ac.uk/spm/>). Specifically, SS-timecourse and KC-timecourse were binary and of the same length as the fMRI data, with ones representing the fMRI samples during which the respective graphoelement occurred, while the HRF-convolved versions were scaled between 0 and 1 with the canonical delays and undershoots (an example of the HRF-convolved timecourses is provided in Supplementary Figure 19c). We evaluated in turn the temporal association of each HMM activity timecourse to both sleep spindles and K-complexes. Three summary measures of association were used: i) Pearson's correlation was computed between each of the HMM state timecourses and the SS- and KC-timecourses within the set of participants that included the given graphoelement (see Supplementary Table 3 for an overview of the occurrence of sleep spindles and K-complexes). ii) Sensitivity to sleep spindles/K-complexes was quantified for each HMM state as the proportion of sleep spindles/K-complexes occurring during that given HMM state. iii) Specificity for sleep spindles/K-complexes was defined for each HMM state as the likelihood of finding that given HMM state active during an instance of the given graphoelement. The distributions across participants of these three summary measures are plotted in Supplementary Figures 20 (for sleep spindles) and 21 (for K-complexes).

To test if any HMM states expressed higher association with the sleep graphoelements than others, we used *t*-tests comparing each combination of the 19 HMM states ($n_{\text{comparisons}} = [19 \times 19 - 19] / 2 = 171$). To establish a chance level we compared the original summary measures (correlation, sensitivity, and specificity) to surrogate data created by permuting the HMM state timecourses 1000 times, and re-calculating the summary measures for each permutation. Each permutation consisted in a random switching of the labels of each instance of an HMM state, keeping the number of occurrences of each HMM state and state transition times constant within participants (see Supplementary Figure 19 for an illustration of the permutation principle).

Supplementary Note 5

FC maps of whole-brain network states

The HMM characterised each state by a vector of mean activity and a covariance matrix. These two data statistics may be understood as a dyadic hierarchy of FC information. The mean distribution of a given state gets estimated from the demeaned and standardised timecourses, and hence describes a change away from the grand-average activity level. ROIs that change their activity in the same direction (positive or negative) are thus functionally connected. The covariance matrix of the state then describes the pairwise ROI-to-ROI co-fluctuations within the time periods where the state is active after subtracting the mean activity of the state (i.e. it is the covariance matrix of the residual). Therefore, the state-wise covariance matrices reflect FC within states, above and beyond the largest global FC trends as accounted for by the mean parameter of the Gaussian distributions. The mean activation maps have been overlaid on brain surfaces in Figure 5 and 6 of the main text. The corresponding FC information is represented in Supplementary Figure 5 and 6. The FC matrices were estimated by converting the state-specific covariance matrices to correlations using the Matlab function, `corrcoef`. In order to highlight the unique FC characteristics of each HMM state, Supplementary Figure 5 and 6 show differential FC maps. These were computed by taking an FC matrix of a given HMM state and subtracting the average of the FC matrices of the remaining states.

Below we describe the FC information of the whole-brain network states in the order suggested by the transition modules of Figure 4d with an emphasis on how they complement the interpretations of the mean activation maps of the HMM states given in the main text. Supplementary Figures 4 and 5 show the differential FC maps.

For the red module of wakefulness shown in Supplementary Figure 4a, the DMN-like increases in mean activation of HMM state 8 (see Figure 5a) were accompanied by relative increases in FC between occipital and temporal areas, and decreases in FC from the supramarginal gyrus to the posterior cingulate and medial prefrontal areas. Similar decreases in FC were evident for HMM state 2, while increases were particularly clear between the posterior cingulate and medial frontal areas.

For the WASO-related HMM states 5 and 17 the frontal increases in mean activation seen in Figure 5 were complemented by relative frontal increases in FC (see Supplementary Figure 4b).

The whole-brain network states of the white N1-related module are represented in Supplementary Figure 5a. These states generally exhibited opposite polarities in their mean activation between subcortical areas (thalamus and parts of the basal ganglia) and primary sensory

cortical areas (see Figure 6a). In terms of differential FC this subcortico-cortical decoupling was mainly evident for HMM state 1, while increases in connections towards the medial prefrontal cortex and the anterior cingulate was common for all three states.

N2 sleep was dominated by HMM states 3 and 6, and the differential FC maps of these whole-brain network states are shown in Supplementary Figure 5b. Relative increases in FC between superior temporal/inferior parietal areas and medial frontal areas were common, and a few increases in thalamo-cortical connections could be related to association of these HMM states to sleep spindles and the thalamo-cortical mechanism behind the generation of these ^{73, 74} (although see Supplementary Note 4 for a closer examination of the relationship between the HMM states and sleep graphoelements).

HMM state 16 accounted for the majority of time spent in N3 sleep, and its differential FC is shown in Supplementary Figure 5c. Interestingly, the decreases in mean activation, exhibited broadly throughout the frontal cortices, were complemented by relative increases in frontal and temporo-frontal connectivity. In the same way that the frontal decreases in mean activation could be explained by slow-wave activity (see main text), the relative increases in frontal FC are also in line with the localisation found in EEG-based source modelling of slow waves ⁷⁵.

To make sure that the differential FC maps were not biased by the effect of the HMM states having different baseline mean activation patterns (as modelled by the mean vector of the Gaussian distribution), we produced equivalent maps using the cosine similarity instead of the covariance matrices outputted by the HMM. Unlike Pearson's correlation, the cosine similarity does not demean the time series, and, therefore, the differences in baselines are accounted for. These maps are shown in Supplementary Figures 17 and 18. This analysis yielded 19 matrices of 90×90 cosine similarity values. By taking each cosine similarity matrix and subtracting from it the average of the remaining 18 cosine similarity matrices, we obtained maps equivalent to the differential FC maps, which were based on the covariance information modelled directly by the HMM. As may be seen, when comparing Supplementary Figure 4 to Supplementary Figure 17, and Supplementary Figure 5 to Supplementary Figure 18, the maps are highly similar.

Supplementary Tables

PSG stage	Mean duration $N = 57$ (minutes)	Proportion $N = 57$ (%)	Number of participants out of $N = 57$	Mean duration $N = 18$ (min)	Proportion $N = 18$ (%)	Number of participants out of $N = 18$
Wake	24.87 (S.D. 15.39)	47.82	57	12.34 (S.D. 6.61)	23.72	18
N1	12.20 (S.D. 9.78)	23.47	57	8.48 (S.D. 2.83)	16.31	18
N2	9.71 (S.D. 9.18)	18.68	40	14.66 (S.D. 5.72)	28.19	18
N3	5.22 (S.D. 9.02)	10.04	18	16.53 (S.D. 8.39)	31.78	18

Supplementary Table 1. Summary details of dataset. Left half: presence of each of the four polysomnography (PSG) stages in the full ($N = 57$) dataset. All participants included wakefulness and N1 sleep. Right half: Similar overview for the 18 participants that visited all four PSG stages during their fMRI recordings.

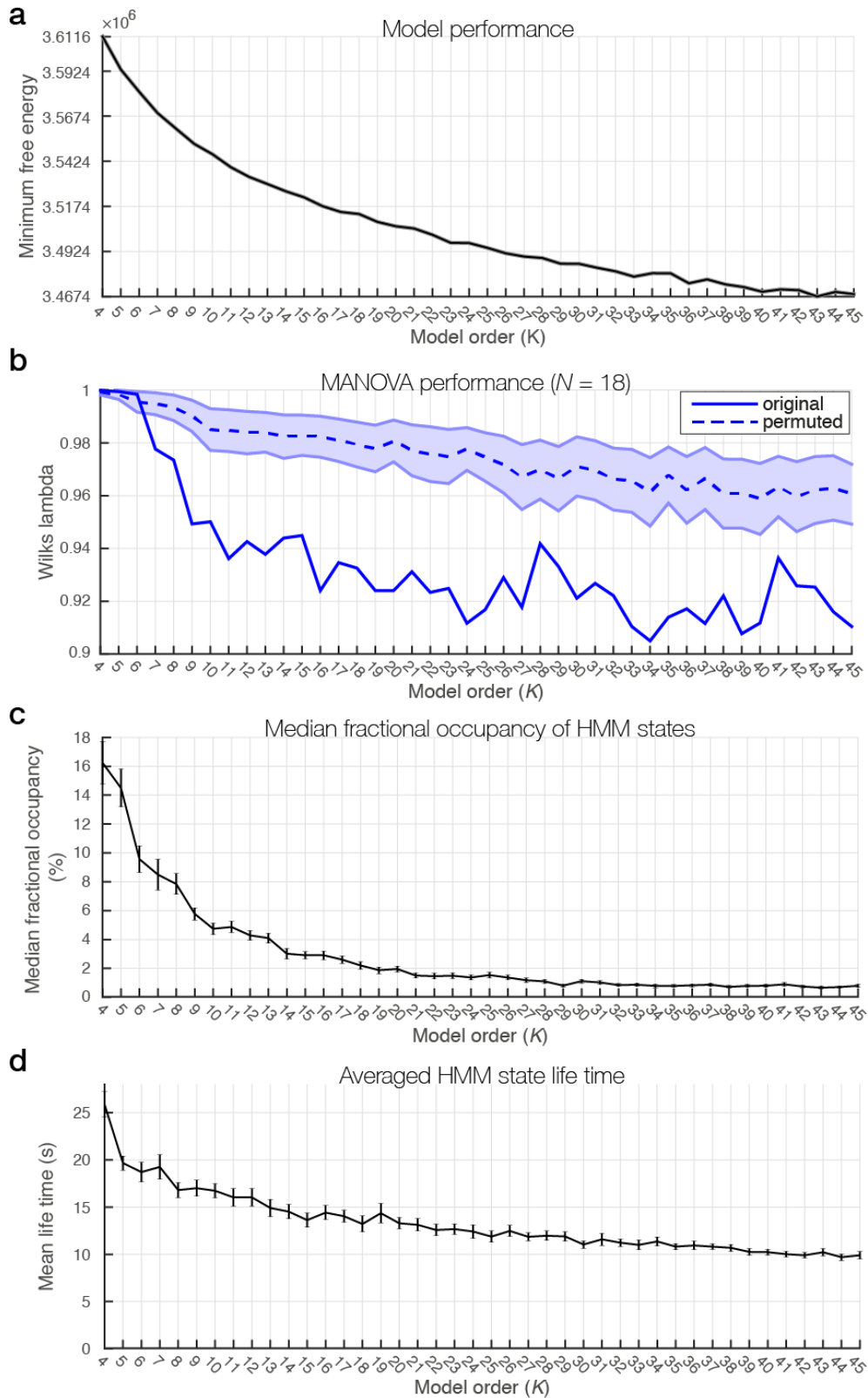
PSG stage	Mean duration $N = 31$ (minutes)	Proportion $N = 31$ (%)	Number of participants out of $N = 31$
Wake	8.39 (S.D. 7.94)	16.13	31
N1	13.19 (S.D. 7.06)	25.37	31
N2	13.54 (S.D. 8.05)	26.05	31
N3	4.88 (S.D. 7.92)	9.38	11
WASO	12.00 (S.D. 7.68)	23.08	31

Supplementary Table 2. Summary details of WASO-subset of the dataset In order investigate whether certain HMM states were more likely to occur after consolidated, we extracted the part of the HMM solution that corresponded to the participants, who woke up after having reached N2 sleep. The table shows the distributions of PSG stages (including WASO) across the 31 participants that woke up.

Sleep graphoelement	Mean count (for participants with count > 0)	Number of participants with count > 0 (% of 57)
Sleep spindles	29.42 (S.D. 29.36)	33 (57.89 %)
K-complexes	32.73 (S.D. 29.19)	37 (64.91 %)

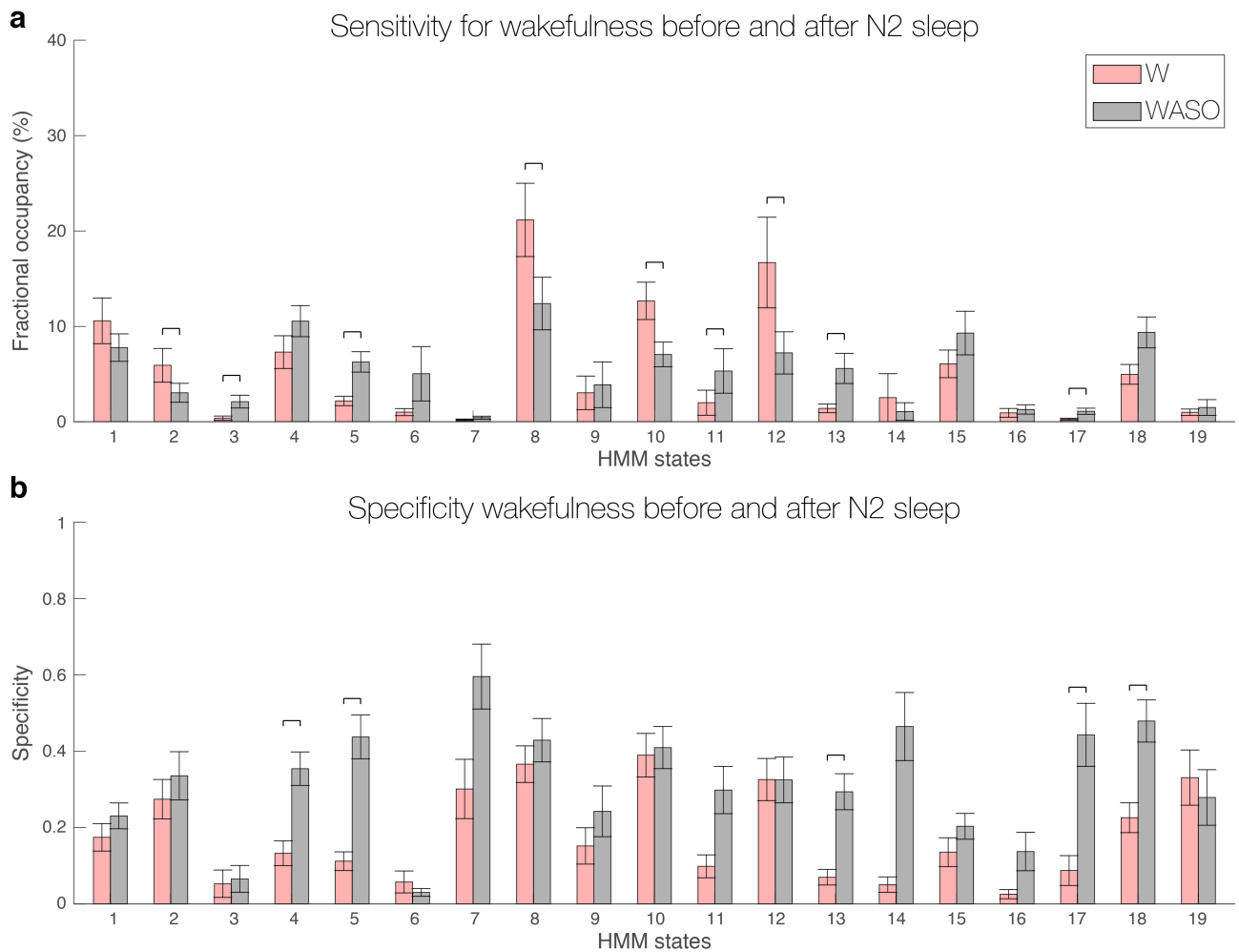
Supplementary Table 3. Summary statistics of sleep graphoelements in dataset The EEG acquired simultaneously with the fMRI was used to identify sleep graphoelements. This scoring information was re-sampled to the fMRI, such that volumes during which either a sleep spindle or a K-complex occurred were marked. The first column of the table shows the mean number of occurrences of each sleep graphoelement after this re-sampling. The mean value is calculated within the participants that included at least one of the given graphoelement. The number of participants including at least on sleep spindle or K-complex is shown in the first and second row, respectively, of the second column of the table.

Supplementary Figures



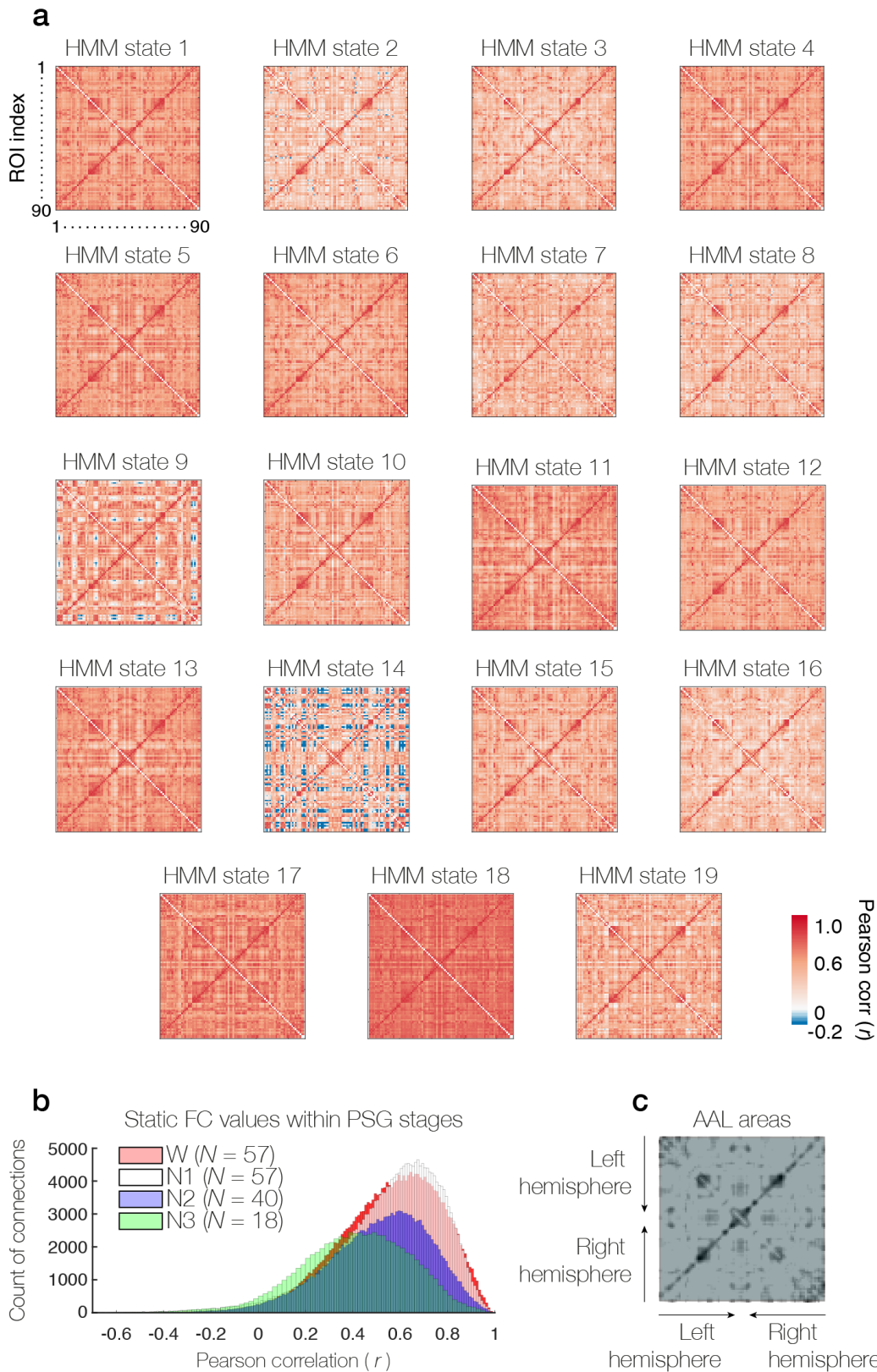
Supplementary Figure 1. Summary measures of HMM solutions across a range of model orders. **a** The minimum free-energy on the VB inference decreased monotonically for increasing model orders. **b** Wilk’s lambda is an output of the MATLAB function `manova1`, and describes how well the HMM state timecourses

could be grouped according to the EEG-based sleep scoring. Lower values correspond to a better fit. Here Wilk's lambda is shown for the part of HMM solutions corresponding to the 18 participants that included all four PSG stages and across a range of model orders. The solid blue line depicts the output of the MANOVA run with the original sleep scoring, while the dashed blue line corresponds to the average Wilk's lambda from 1000 MANOVAs where the sleep scoring was randomly permuted. Error zones correspond to the standard deviations of the permuted cases. Note how the original sleep scoring expressed significantly better fitting with the HMM state timecourses for model orders above $K = 7$, and how Wilk's lambda appeared to stagnate somewhere between $10 < K < 20$. **c** The development of the median fractional occupancy as a function of HMM model order. Vertical error bars indicate the standard errors across participants ($N=18$). Note how the median fractional occupancy stagnates from around $K \sim 19$, indicating that the addition of more states did not split existing (at lower model orders) states, but resulted in the addition of 'sporadic' states. **d** HMM state life time averaged across states and participants ($N = 18$) as a function of model order. Error bars indicate the standard errors across participants. Note how the curve stagnates around $K \sim 18$.



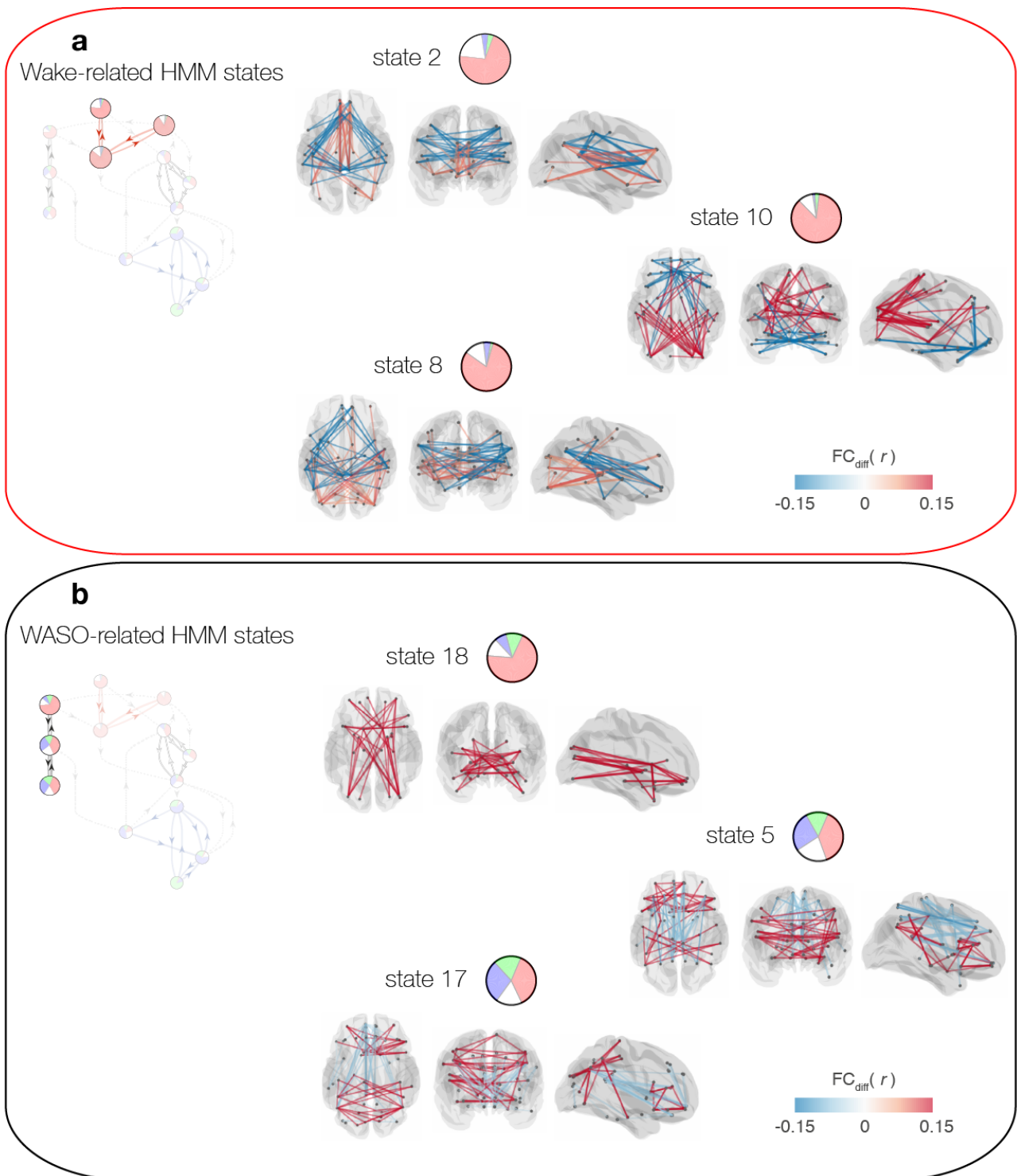
Supplementary Figure 2. Sensitivity and specificity of HMM states when separating wakefulness before and after sleep (supplement to Figure 3). a and b corresponds to a and b of Figure 3 respectively, but for the 31 participants that woke up after having reached N2 sleep. Wake after sleep onset (WASO) was defined as polysomnographically estimated wakefulness following N2 sleep, and is represented by the black bars, while wakefulness (W) was defined as periods of PSG-estimated wakefulness prior to N2 sleep. The coloured bars and error bars show the average and standard error, respectively, across participants. To highlight the differences between W and WASO, we have excluded the remaining sleep stages from this plot. Horizontal lines show significant differences with p -values < 0.01 , as evaluated with paired t -tests and permutation testing. Note how HMM states forming the black module in the transition map of Figure 4, showed higher specificity for WASO compared to W.

HMM state FC matrices

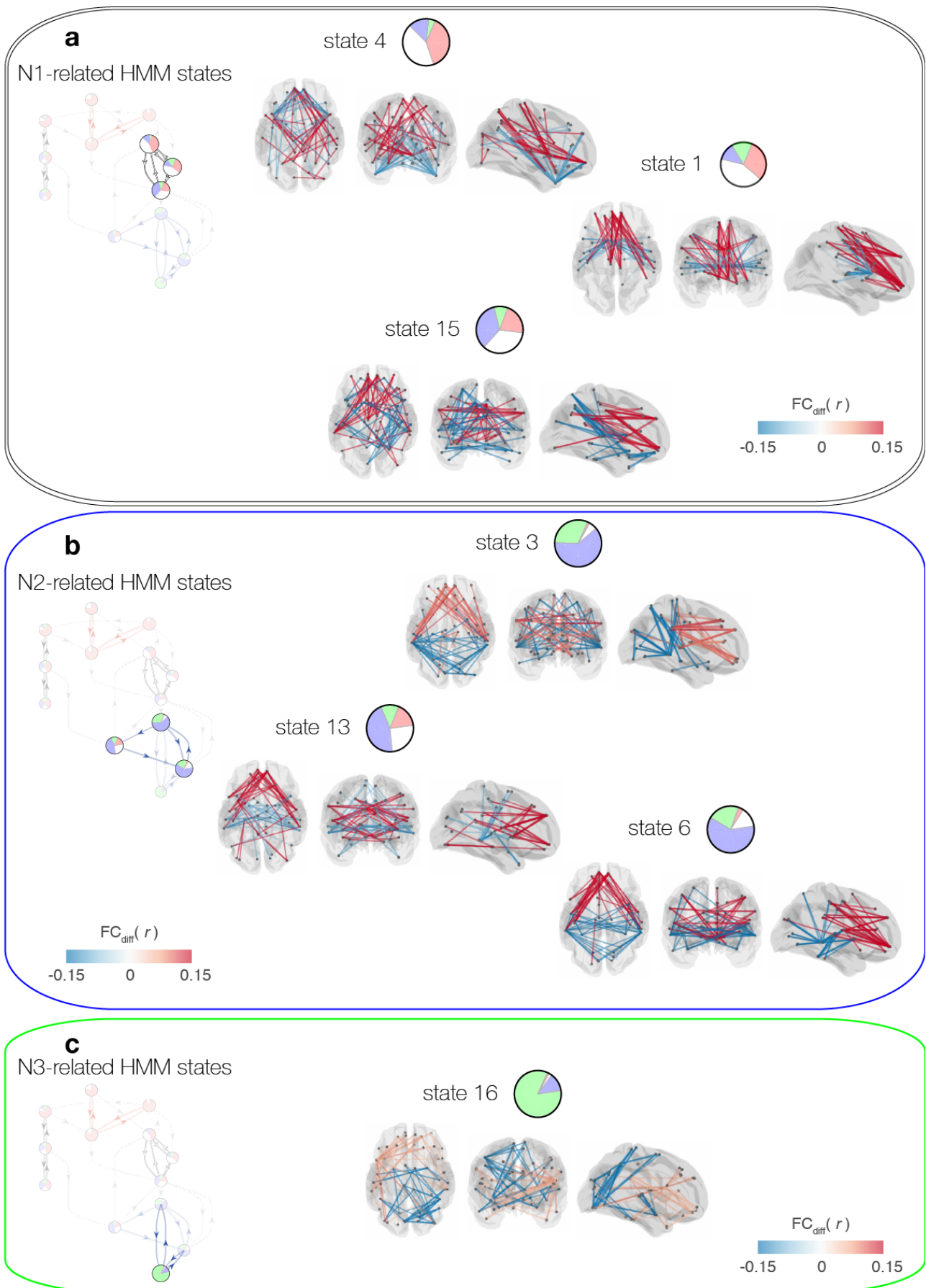


Supplementary Figure 3. HMM state FC matrices. **a** The 90×90 FC matrices for the 19 HMM states were calculated as conversion from the state covariance matrices output directly by the HMM. Covariance values were converted to Pearson's correlation values. Each entry of a matrix corresponds to the pairwise FC between two AAL ROIs. **b** The FC matrices of the HMM states were skewed towards positive correlations. To show that this was a feature of the ROI timecourses and not an effect of the HMM, we have included

histograms of the super-diagonal elements of the static FC matrices computed directly from the fMRI data within the PSG stages. **c** The ROIs of the FC matrices in **a** have been reordered such that the first and third quadrants include cross-hemispheric connections, while inter-hemispheric connections are shown in the second and fourth quadrants.

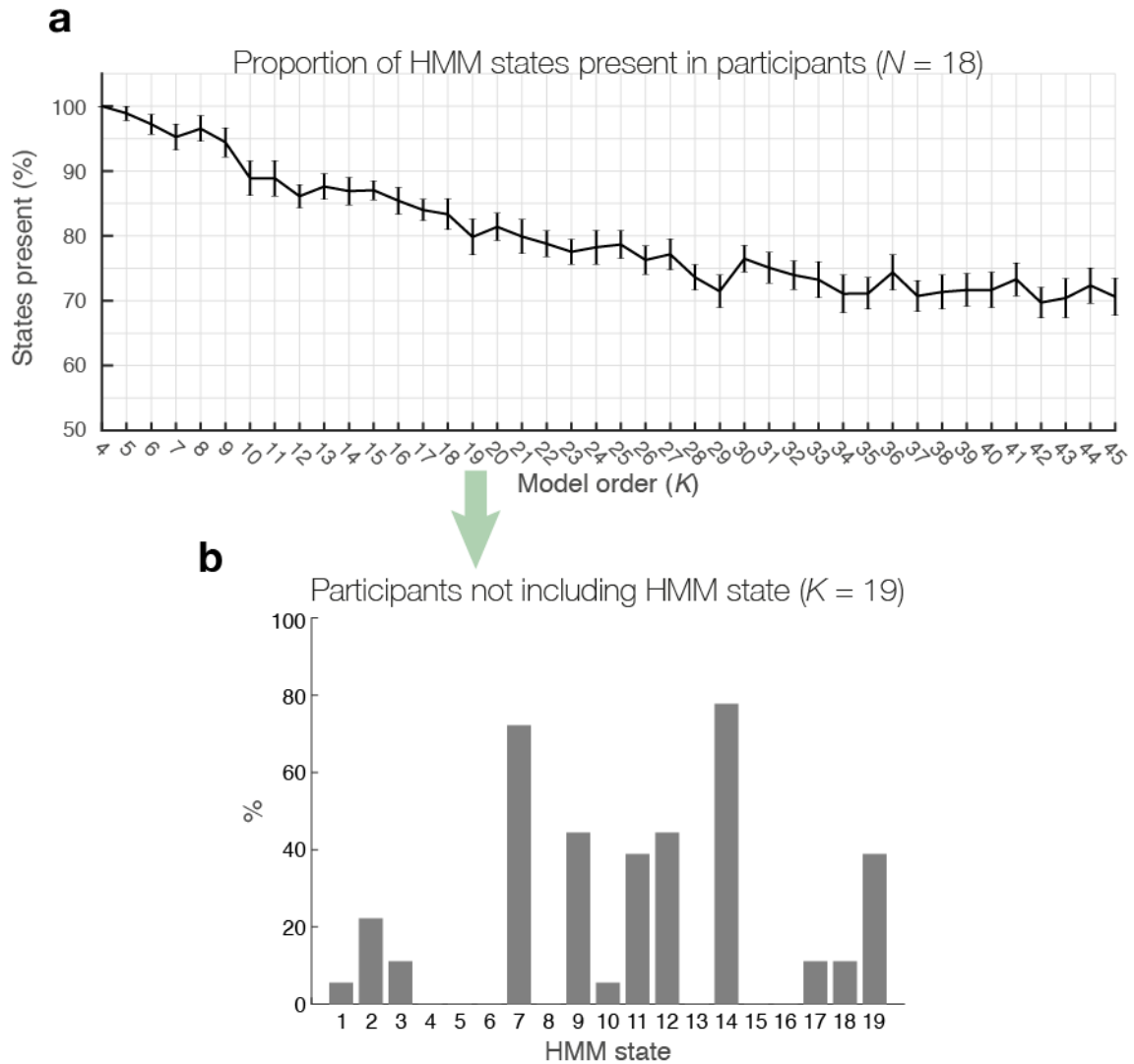


Supplementary Figure 4. Differential FC maps of wakefulness-related HMM states (supplement to Figure 5). Differential FC maps were computed by taking an FC matrix of a given HMM state and subtracting the average of the FC matrices of the remaining states. Maps show the 1% most negative and 1% most positive weights of each state **a** Differential FC maps of wakefulness prior to sleep. Note the relative increases in connections between occipital and temporal areas, as well as the decreases between supramarginal gyrus and the posterior cingulate cortex. **b** Differential FC maps of wakefulness after sleep onset (WASO). These states were in general characterised by relative increases in frontal connections.

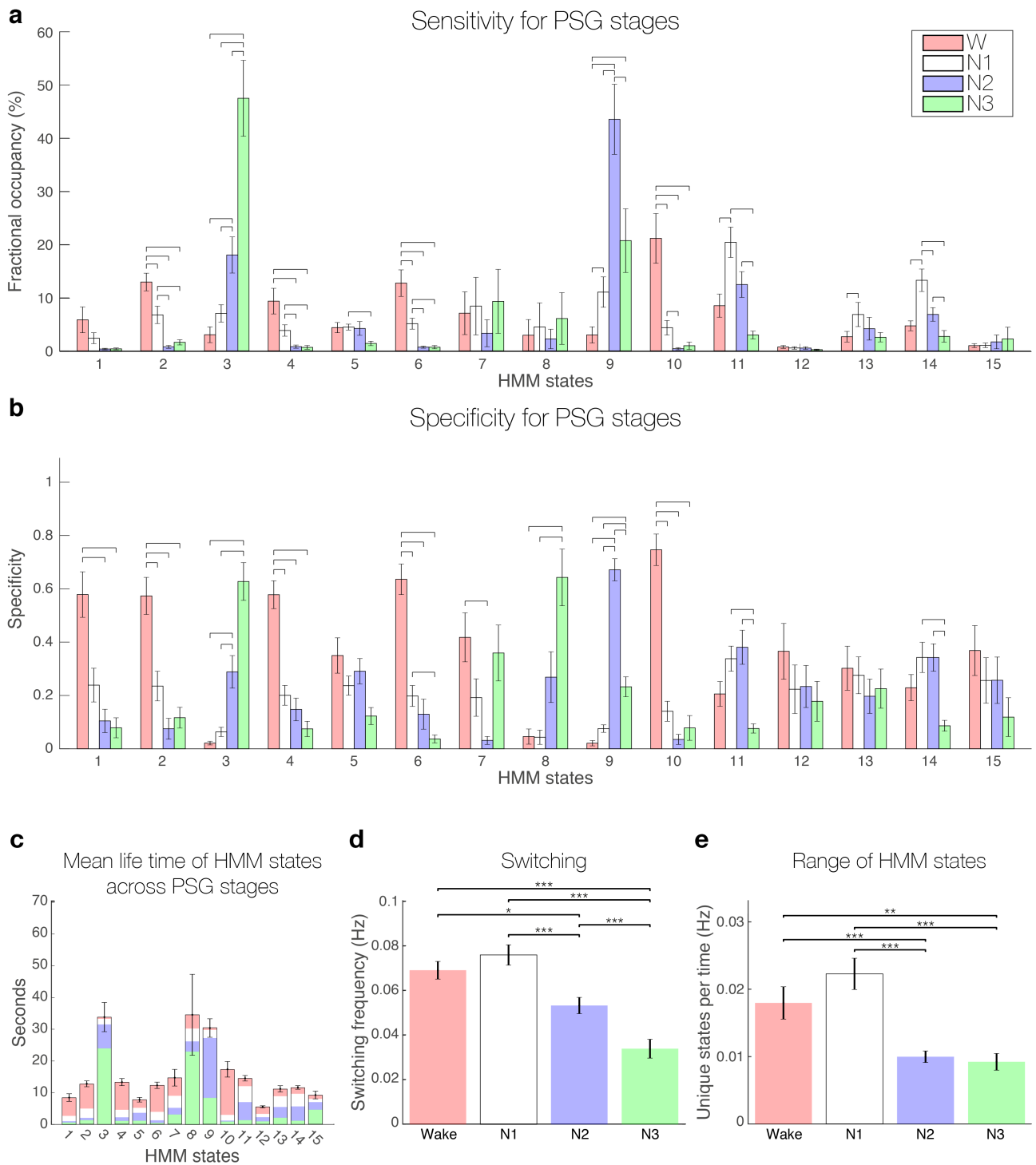


Supplementary Figure 5. Differential FC maps of sleep-related HMM states (supplement to Figure 6). **a** Differential FC maps of HMM states related to N1 sleep. Note the decreased FC between subcortical and

temporal/parietal areas of HMM state 1. **b** Differential FC maps of N2-related HMM states. A common trait of these three states was increased FC in temporal/inferior parietal areas and medial frontal. **c** N3-related differential FC maps. Note the relative increases in frontal FC. Maps show the 1% most negative and 1% most positive weights of each state

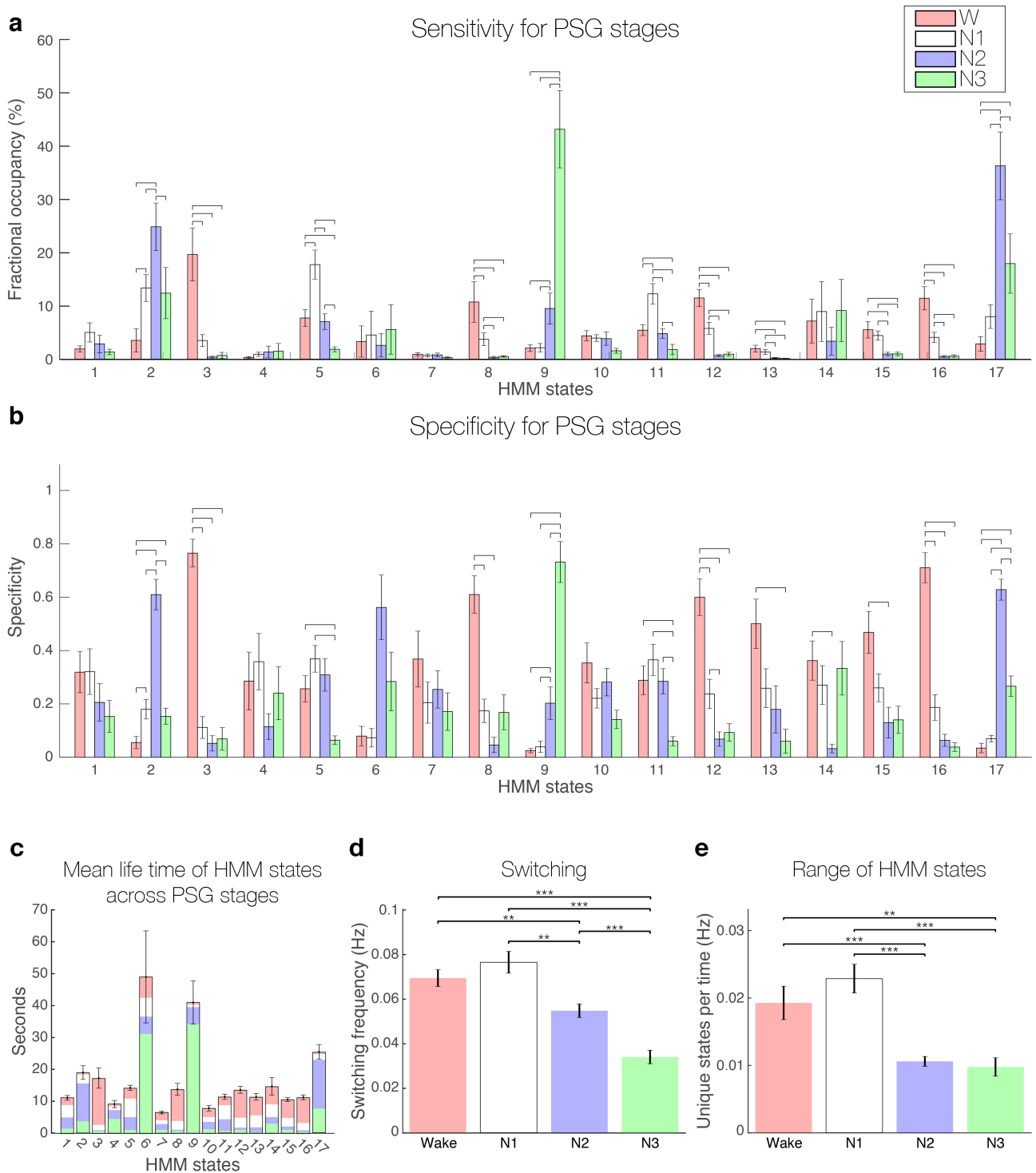


Supplementary Figure 6. Summary of inconsistent HMM states across participants. **a** The graph shows the proportion of HMM states that were present in all participants as a function of model order. Included here are the 18 participants that reached all four PSG stages during their recording session. As the model order increased the probability of finding all HMM states in all participants dropped. Error bars show the standard error across participants. **b** The solution presented in the main text ($K = 19$) is summarised in terms of the presence of the individual HMM states. The bars show the proportion of participant in which the HMM states were not present. As evident, six HMM states (7, 9, 11, 12, 14, and 19) were present in less than 60 % of the participants. We call these ‘sporadic’ HMM states, as they did not model data traits consistent across participants.



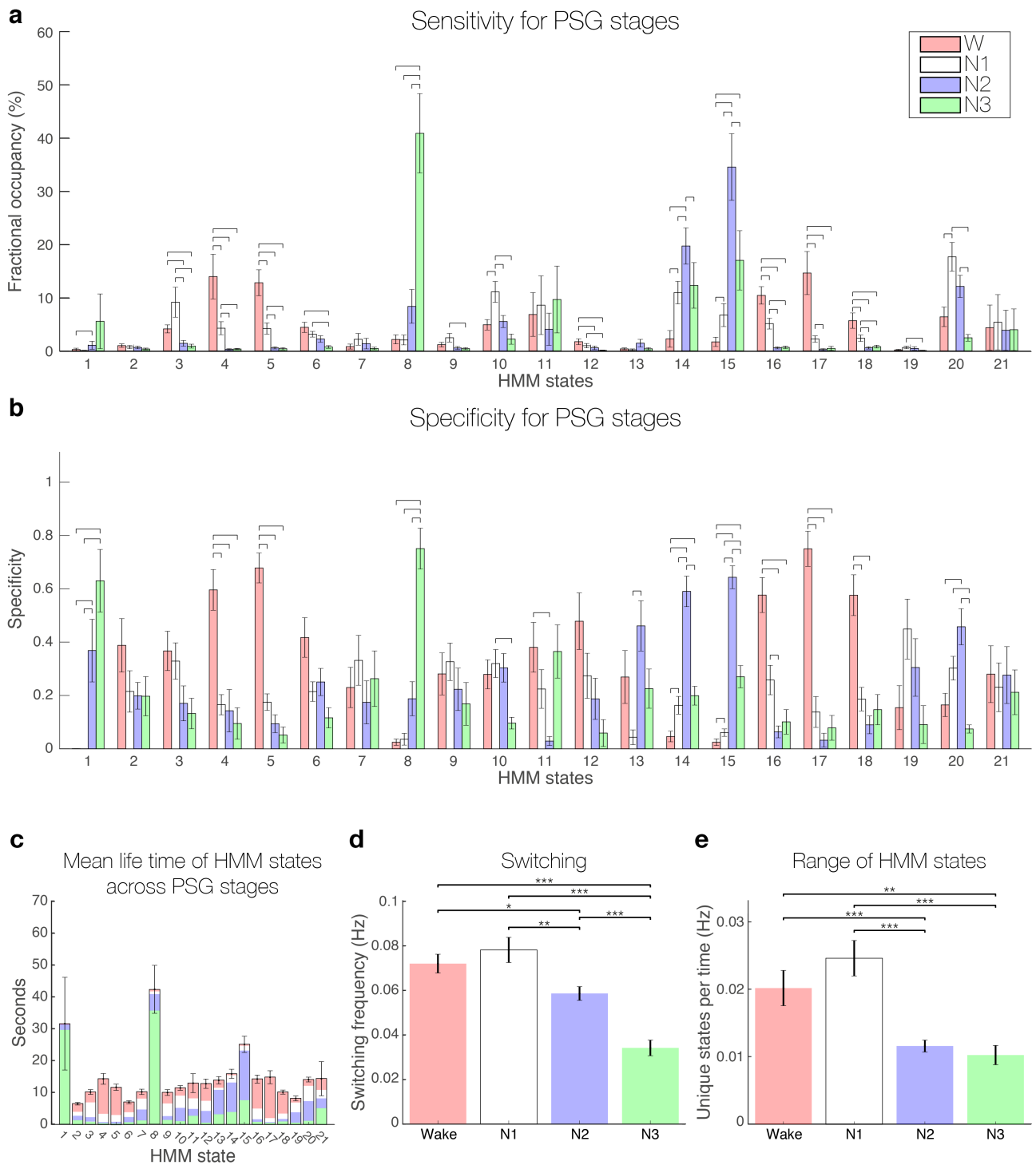
Supplementary Figure 7. $K = 15$, Sensitivity and specificity of HMM states and dynamics within polysomnography stages (supplement to Figure 3). **a** Fractional occupancies of each of the 15 HMM states computed within the four PSG stages corresponded to the PSG-sensitivity of the whole-brain network states. The coloured bars and error bars show the average and standard error, respectively, across the 18 participants that included all four PSG stages. **b** PSG-specificity of the HMM states for each of the four PSG stages. Specificity corresponds to the probability of an HMM state occurring within a PSG stage. The bars represent the group average and the error bars the standard error ($N = 18$). In **a** and **b** horizontal lines show significant differences within HMM states, with p -values < 0.01 as evaluated through paired t -tests and permutation testing. **c** The mean life times of the 15 HMM states are shown by the bars, representing values averaged across the 18 participants. Error-bars represent the standard error across participants. Each HMM state is coloured according to the probability of finding it within each of the four PSG stages, i.e. their PSG

specificity. **d** The dynamics of the HMM transitions were calculated within each of the four PSG stages, in terms of switching frequency ('Switching'), and **e** the number of different HMM states visited per time ('Range of HMM states'). In **d** and **e** error bars represent standard error across participants and significant differences between PSG stages are denoted by stars: * $p < 0.05$, ** $p < 0.01$, *** $p < 0.001$.



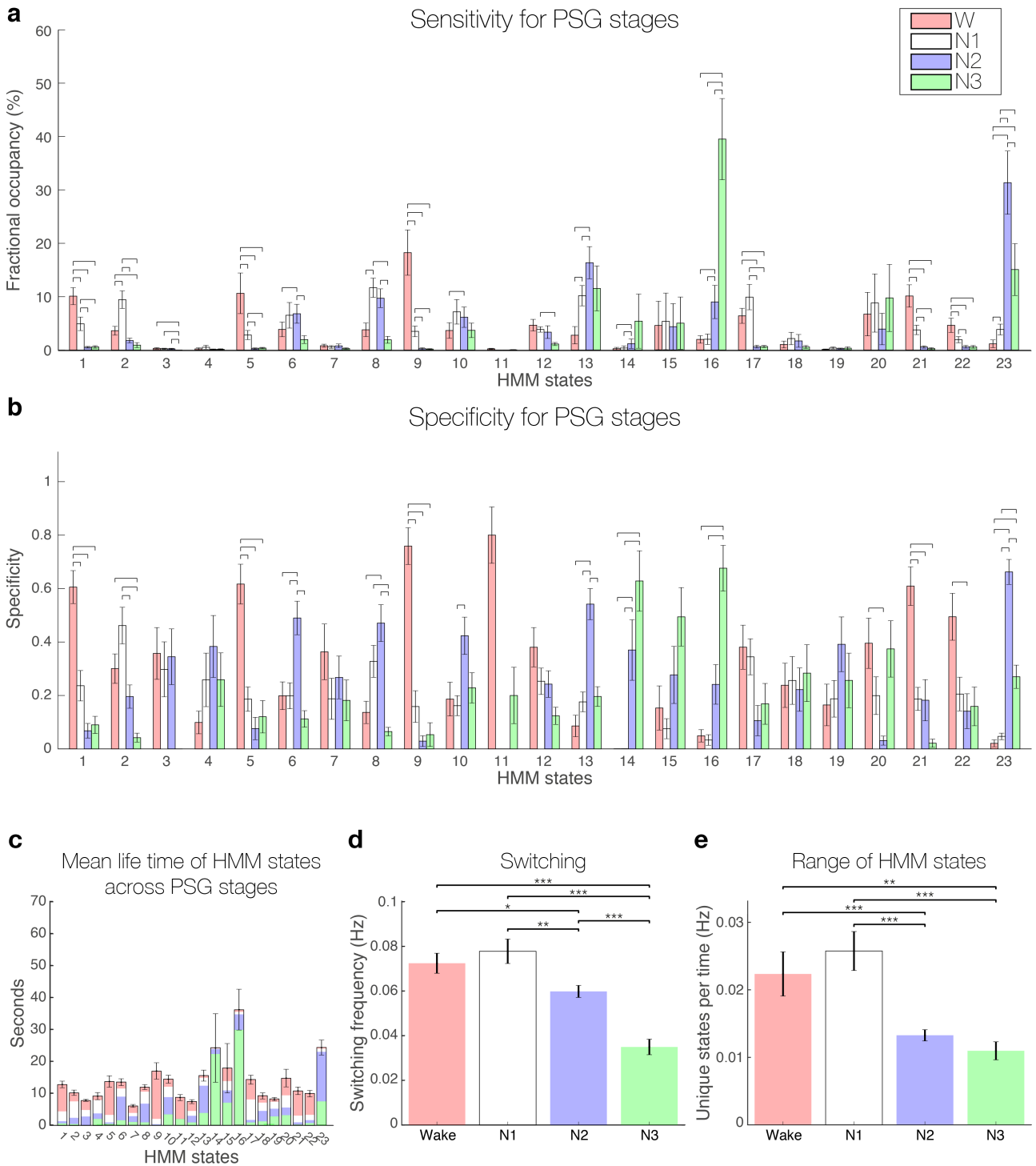
Supplementary Figure 8. $K = 17$, Sensitivity and specificity of HMM states and dynamics within polysomnography stages (supplement to Figure 3). **a** Fractional occupancies of each of the 17 HMM states computed within the four PSG stages corresponded to the PSG-sensitivity of the whole-brain network states. The coloured bars and error bars show the average and standard error, respectively, across the 18 participants that included all four PSG stages. **b** PSG-specificity of the HMM states for each of the four PSG stages. Specificity corresponds to the probability of an HMM state occurring within a PSG stage. The bars represent the group average and the error bars the standard error ($N = 18$). In **a** and **b** horizontal lines show significant differences within HMM states, with p -values < 0.01 as evaluated through paired t -tests and permutation testing. **c** The mean life times of the 17 HMM states are shown by the bars, representing values averaged across the 18 participants. Error-bars represent the standard error across participants. Each HMM state is coloured according to the probability of finding it within each of the four PSG stages, i.e. their PSG

specificity. **d** The dynamics of the HMM transitions were calculated within each of the four PSG stages, in terms of switching frequency ('Switching'), and **e** the number of different HMM states visited per time ('Range of HMM states'). In **d** and **e** error bars represent standard error across participants and significant differences between PSG stages are denoted by stars: * $p < 0.05$, ** $p < 0.01$, *** $p < 0.001$.



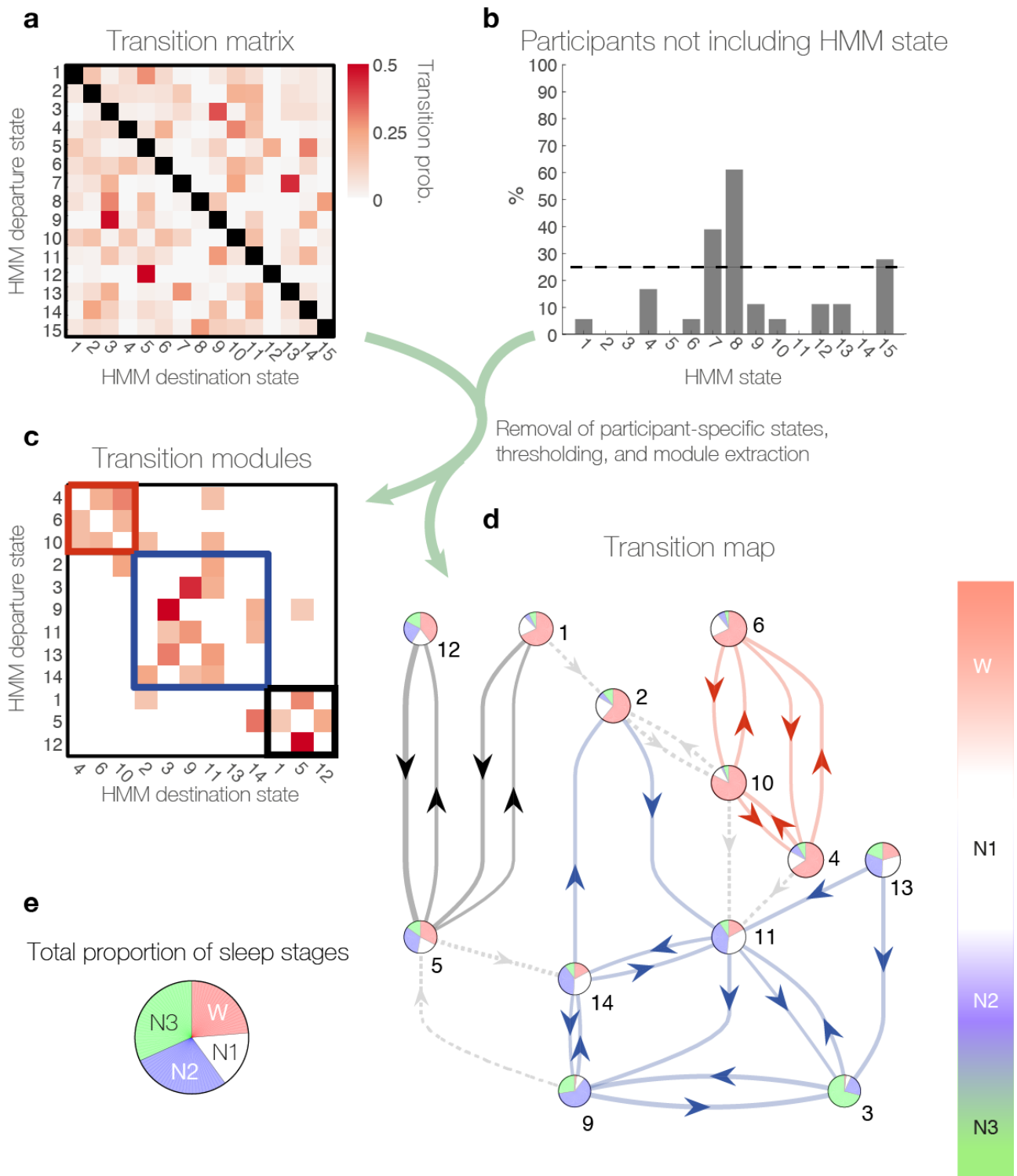
Supplementary Figure 9. $K = 21$, Sensitivity and specificity of HMM states and dynamics within polysomnography stages (supplement to Figure 3). **a** Fractional occupancies of each of the 21 HMM states computed within the four PSG stages corresponded to the PSG-sensitivity of the whole-brain network states. The coloured bars and error bars show the average and standard error, respectively, across the 18 participants that included all four PSG stages. **b** PSG-specificity of the HMM states for each of the four PSG stages. Specificity corresponds to the probability of an HMM state occurring within a PSG stage. The bars represent the group average and the error bars the standard error ($N = 18$). In **a** and **b** horizontal lines show significant differences within HMM states, with p -values < 0.01 as evaluated through paired t -tests and permutation testing. **c** The mean life times of the 21 HMM states are shown by the bars, representing values averaged across the 18 participants. Error-bars represent the standard error across participants. Each HMM state is coloured according to the probability of finding it within each of the four PSG stages, i.e. their PSG

specificity. **d** The dynamics of the HMM transitions were calculated within each of the four PSG stages, in terms of switching frequency ('Switching'), and **e** the number of different HMM states visited per time ('Range of HMM states'). In **d** and **e** error bars represent standard error across participants and significant differences between PSG stages are denoted by stars: * $p < 0.05$, ** $p < 0.01$, *** $p < 0.001$.



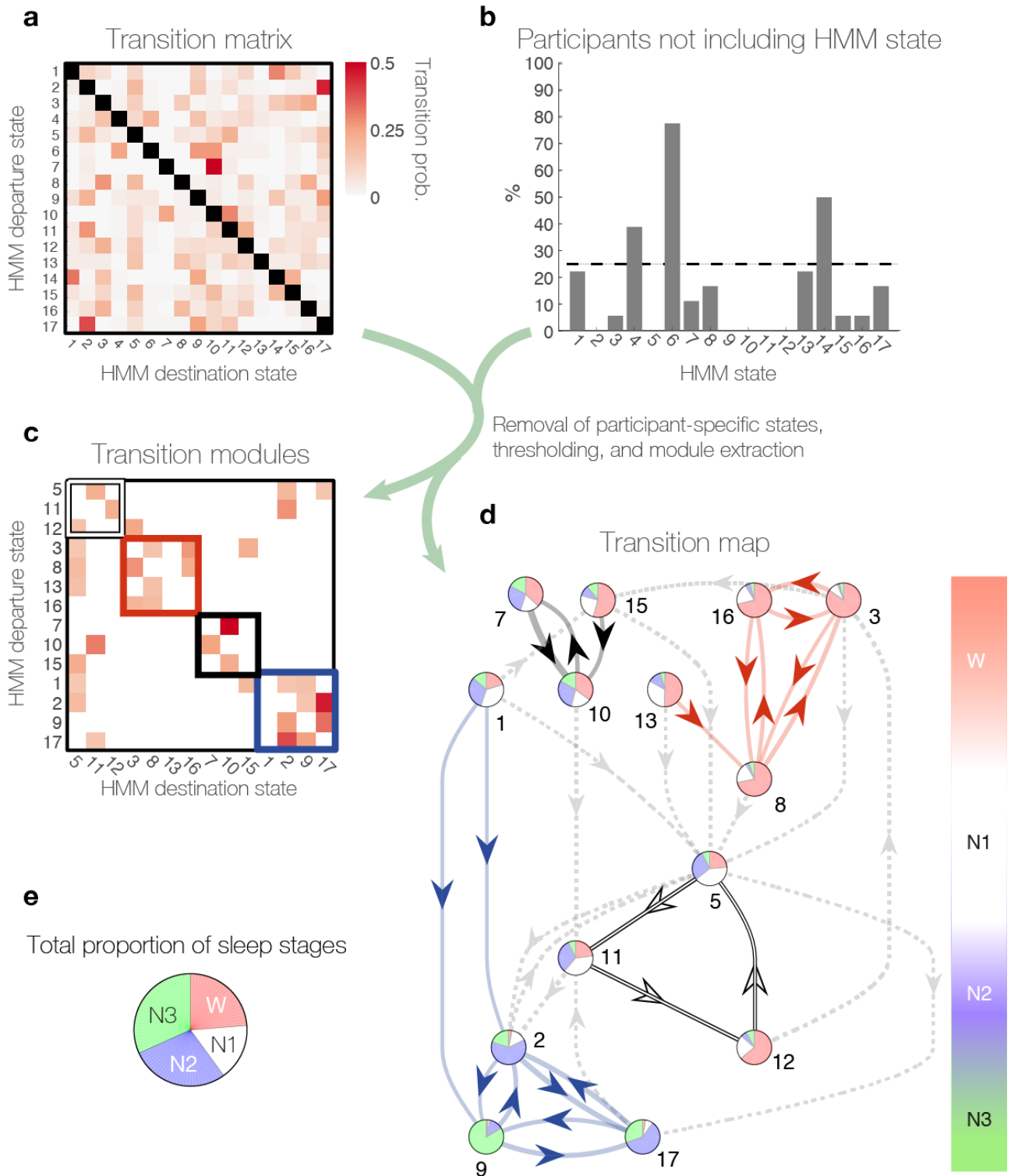
Supplementary Figure 10. $K = 23$, Sensitivity and specificity of HMM states and dynamics within polysomnography stages (supplement to Figure 3). **a** Fractional occupancies of each of the 23 HMM states computed within the four PSG stages corresponded to the PSG-sensitivity of the whole-brain network states. The coloured bars and error bars show the average and standard error, respectively, across the 18 participants that included all four PSG stages. **b** PSG-specificity of the HMM states for each of the four PSG stages. Specificity corresponds to the probability of an HMM state occurring within a PSG stage. The bars represent the group average and the error bars the standard error ($N = 18$). In **a** and **b** horizontal lines show significant differences within HMM states, with p -values < 0.01 as evaluated through paired t -tests and permutation testing. **c** The mean life times of the 23 HMM states are shown by the bars, representing values averaged across the 18 participants. Error-bars represent the standard error across participants. Each HMM state is coloured according to the probability of finding it within each of the four PSG stages, i.e. their PSG

specificity. **d** The dynamics of the HMM transitions were calculated within each of the four PSG stages, in terms of switching frequency ('Switching'), and **e** the number of different HMM states visited per time ('Range of HMM states'). In **d** and **e** error bars represent standard error across participants and significant differences between PSG stages are denoted by stars: * $p < 0.05$, ** $p < 0.01$, *** $p < 0.001$.



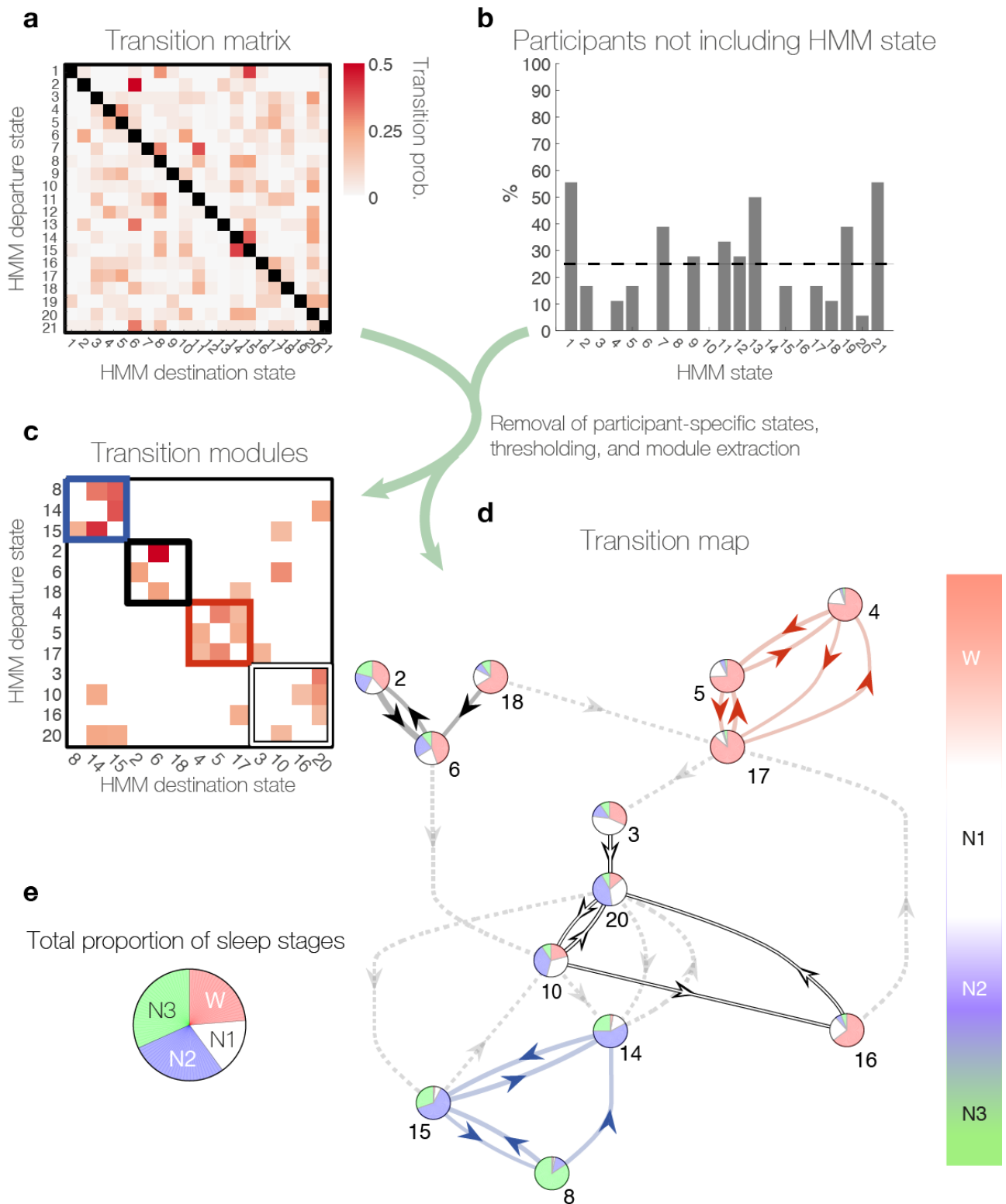
Supplementary Figure 11. $K = 15$ Investigating transitions between whole-brain network states. (supplement to Figure 4). **a** The figure shows the 15×15 transition probability matrix of the HMM states calculated for the 18 participants that included all four PSG stages in their respective scanning session. This quantifies the likelihood of transitioning from any given state to any other state, giving each matrix entry: probability of (departure state, destination state). **b** A few HMM states were ‘sporadic’ and did not occur consistently across participants. HMM states not occurring in more than 25% of the participants were excluded. **c** The strongest transitions of the consistent HMM states were partitioned through a modularity analysis, and reorganised in a matrix according to the four resulting modules. **d** The transitions shown in **c** are presented as a transition map with each state depicted as a pie plot expressing its specificity for each of the four PSG stages. Arrows show the direction of the transitions with thickness proportional to the transition

probability. Note the similar overall structure of the transition map to the one presented in Figure 4 of the main text. Unlike the other numbers of states tested, $K = 15$ only yielded 3 modules, suggesting that the white and the blue module of Figure 4 have merged together in one. e Pie chart showing the total proportion PSG stages within the 18 participants.



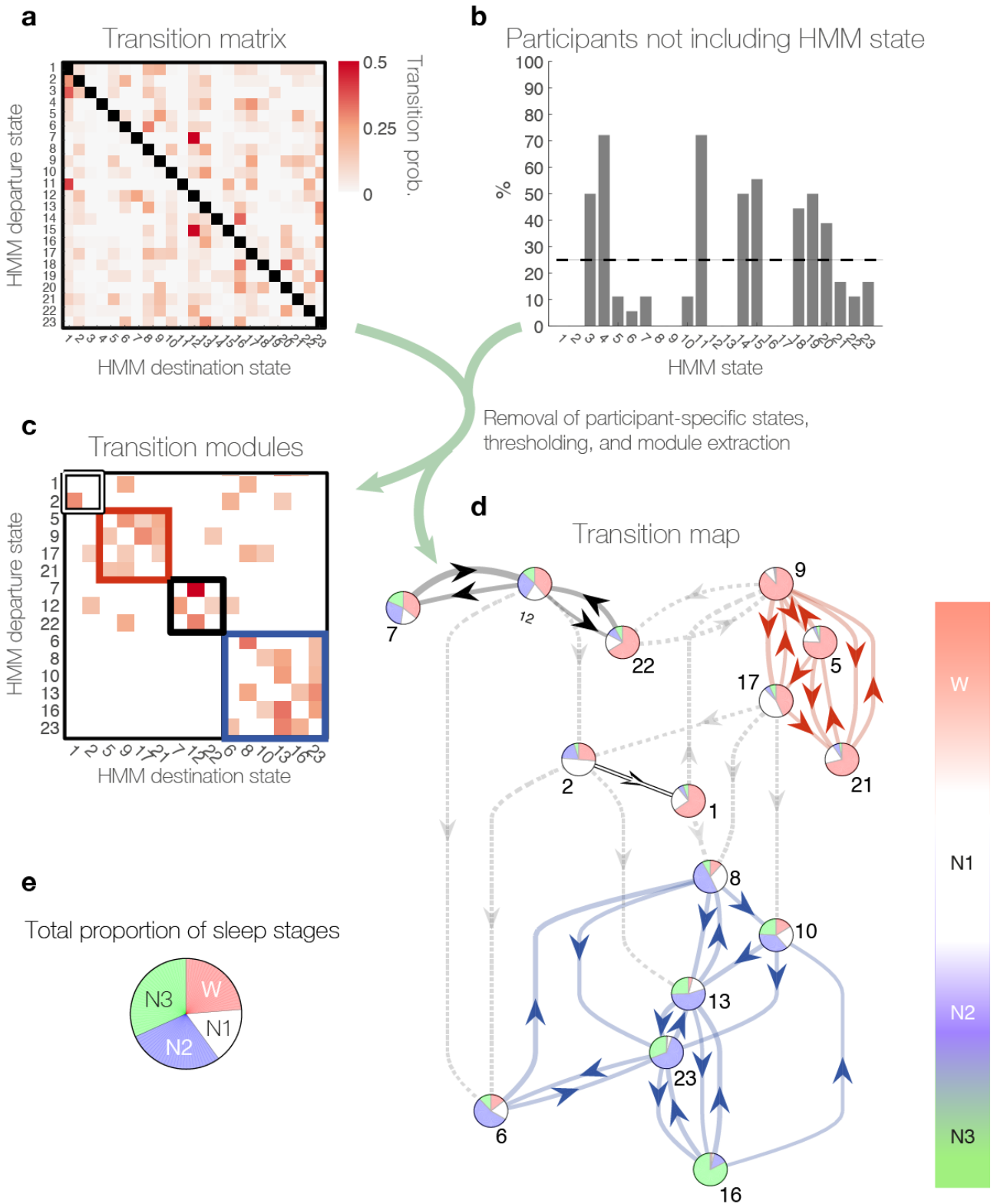
Supplementary Figure 12. $K = 17$ Investigating transitions between whole-brain network states. (supplement to Figure 4). **a** The figure shows the 17×17 transition probability matrix of the HMM states calculated for the 18 participants that included all four PSG stages in their respective scanning session. This quantifies the likelihood of transitioning from any given state to any other state, giving each matrix entry: probability of (departure state, destination state). **b** A few HMM states were ‘sporadic’ and did not occur consistently across participants. HMM states not occurring in more than 25% of the participants were excluded. **c** The strongest transitions of the consistent HMM states were partitioned through a modularity analysis, and reorganised in a matrix according to the four resulting modules. **d** The transitions shown in **c** are presented as a transition map with each state depicted as a pie plot expressing its specificity for each of

the four PSG stages. Arrows show the direction of the transitions with thickness proportional to the transition probability. Note the similar overall structure of the transition map to the one presented in Figure 4 of the main text, including 4 separated transition modules. e Pie chart showing the total proportion PSG stages within the 18 participants.



Supplementary Figure 13. $K = 21$ Investigating transitions between whole-brain network states. (supplement to Figure 4). **a** The figure shows the 21×21 transition probability matrix of the HMM states calculated for the 18 participants that included all four PSG stages in their respective scanning session. This quantifies the likelihood of transitioning from any given state to any other state, giving each matrix entry: probability of (departure state, destination state). **b** A few HMM states were ‘sporadic’ and did not occur consistently across participants. HMM states not occurring in more than 25% of the participants were excluded. **c** The strongest transitions of the consistent HMM states were partitioned through a modularity

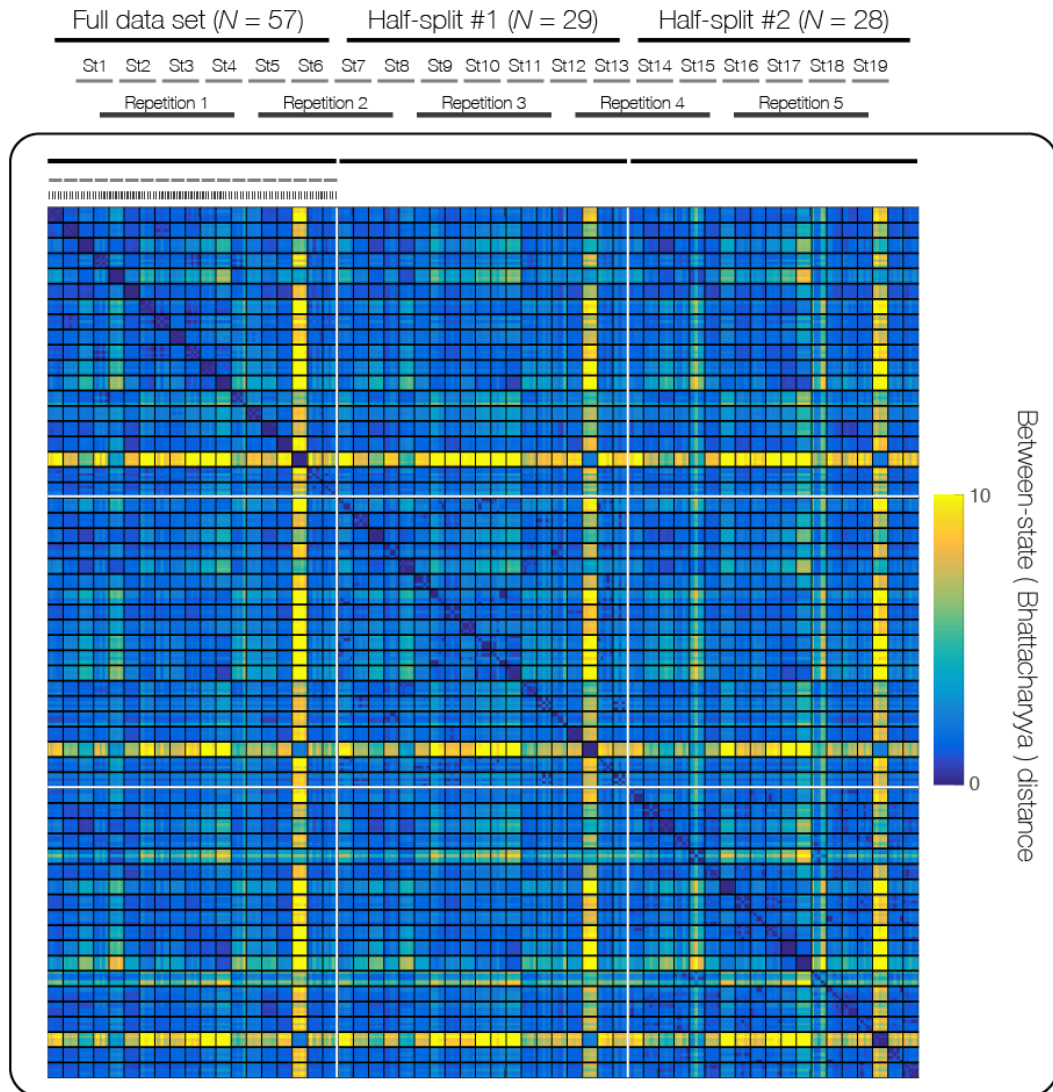
analysis, and reorganised in a matrix according to the four resulting modules. **d** The transitions shown in **c** are presented as a transition map with each state depicted as a pie plot expressing its specificity for each of the four PSG stages. Arrows show the direction of the transitions with thickness proportional to the transition probability. Note the similar overall structure of the transition map to the one presented in Figure 4 of the main text, including 4 separated transition modules. **e** Pie chart showing the total proportion PSG stages within the 18 participants.



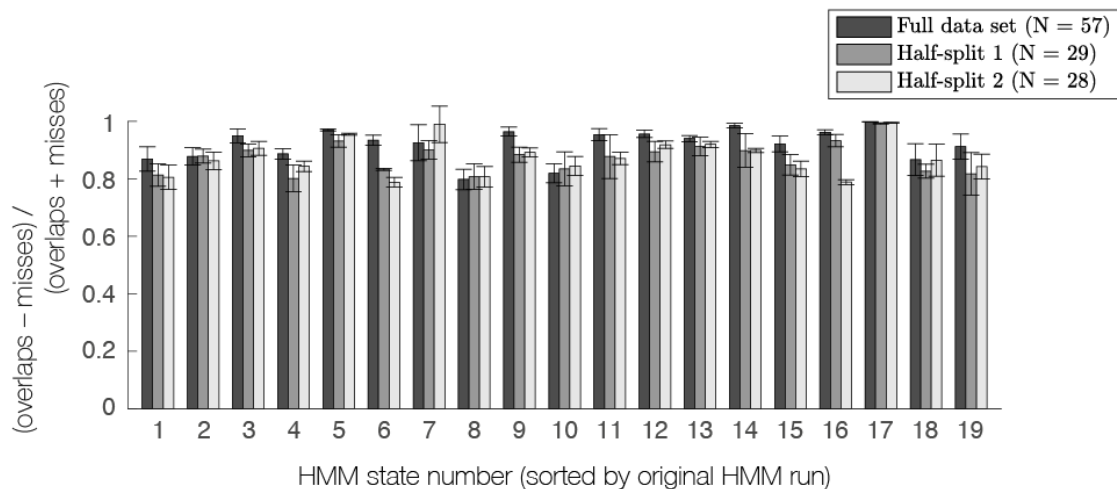
Supplementary Figure 14. $K = 23$ Investigating transitions between whole-brain network states. (supplement to Figure 4). **a** The figure shows the 23×23 transition probability matrix of the HMM states calculated for the 18 participants that included all four PSG stages in their respective scanning session. This quantifies the likelihood of transitioning from any given state to any other state, giving each matrix entry: probability of (departure state, destination state). **b** A few HMM states were ‘sporadic’ and did not occur consistently across participants. HMM states not occurring in more than 25% of the participants were

excluded. **c** The strongest transitions of the consistent HMM states were partitioned through a modularity analysis, and reorganised in a matrix according to the four resulting modules. **d** The transitions shown in **c** are presented as a transition map with each state depicted as a pie plot expressing its specificity for each of the four PSG stages. Arrows show the direction of the transitions with thickness proportional to the transition probability. Note the similar overall structure of the transition map to the one presented in Figure 4 of the main text, including 4 separated transition modules. **e** Pie chart showing the total proportion PSG stages within the 18 participants.

a Distances between state distributions across different HMM initialisations

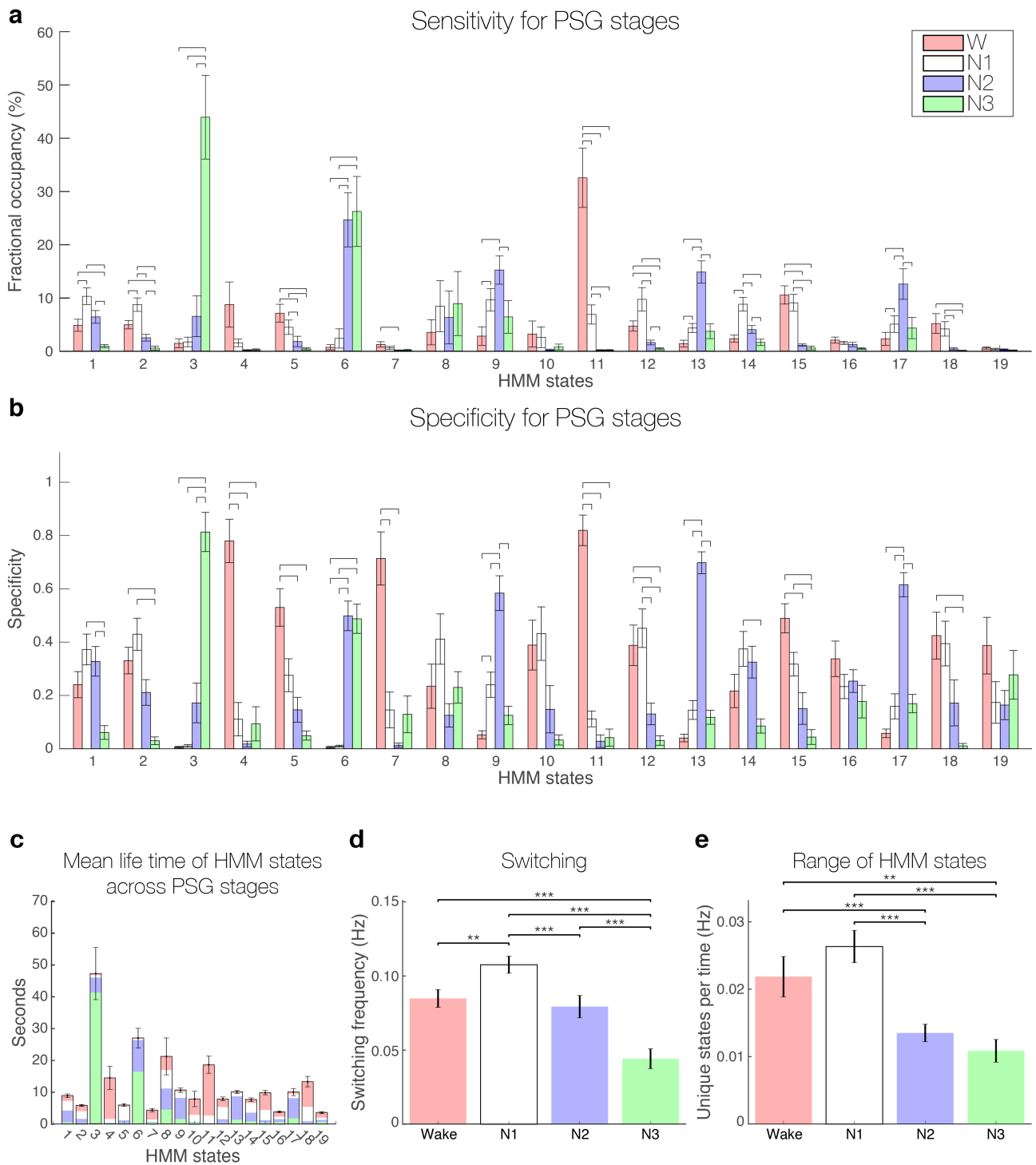


b Temporal robustness across different HMM initialisation

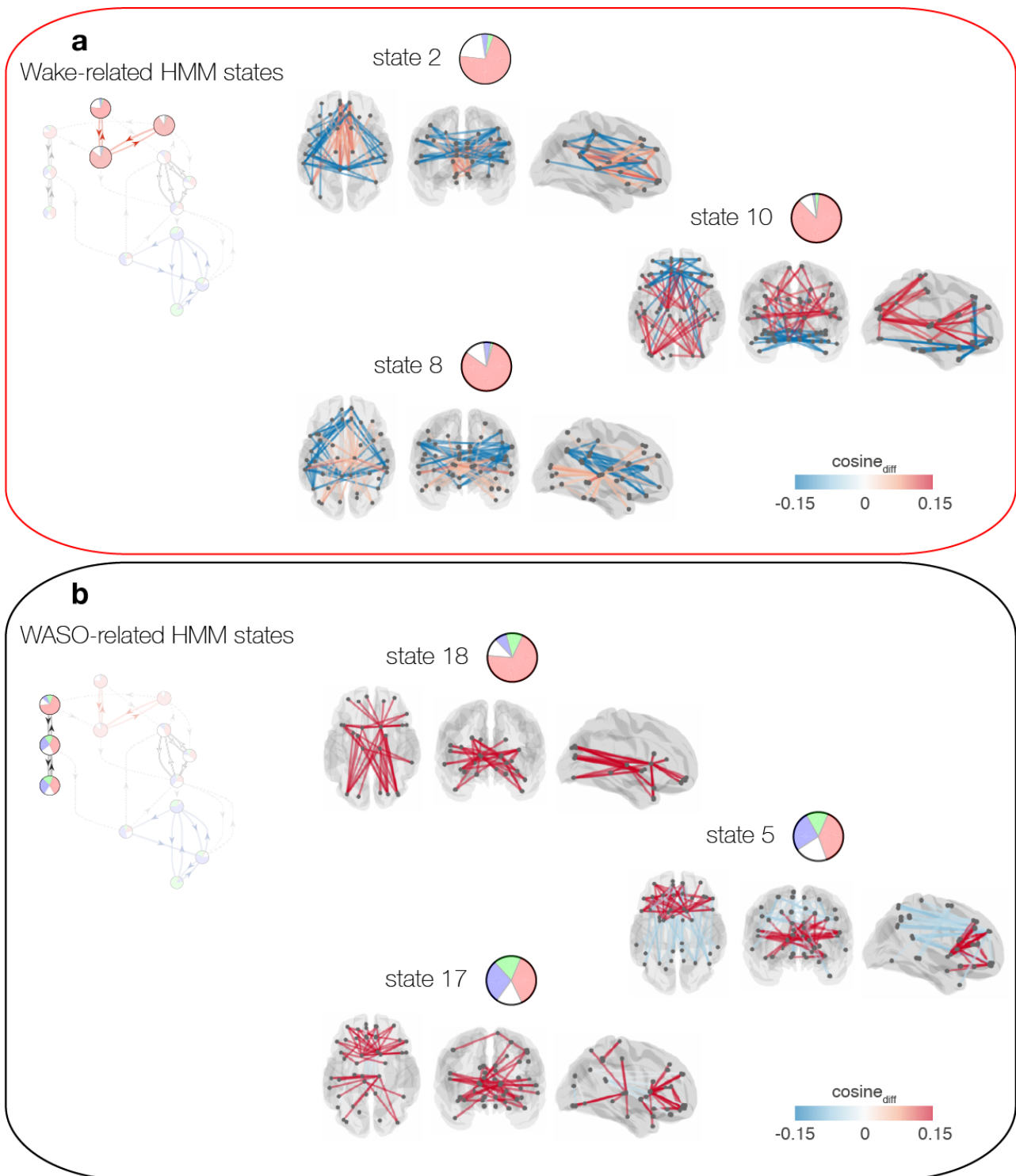


Supplementary Figure 15. Robustness across different random initialisation of the HMM. **a** To make sure that the states inferred by the HMM were not contingent on the initialisation, we ran the HMM with 19 states an additional four times on the full dataset ('Full data set', $N = 57$), and five times on each of the two half-

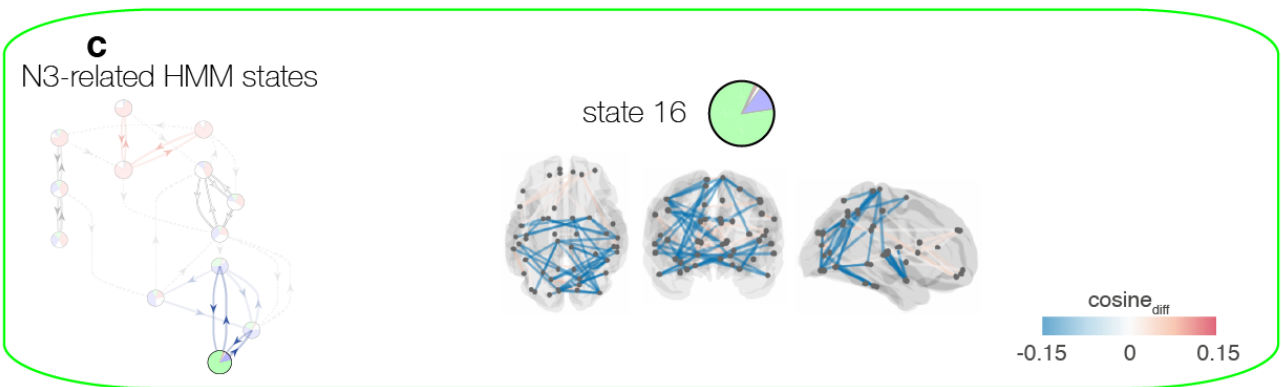
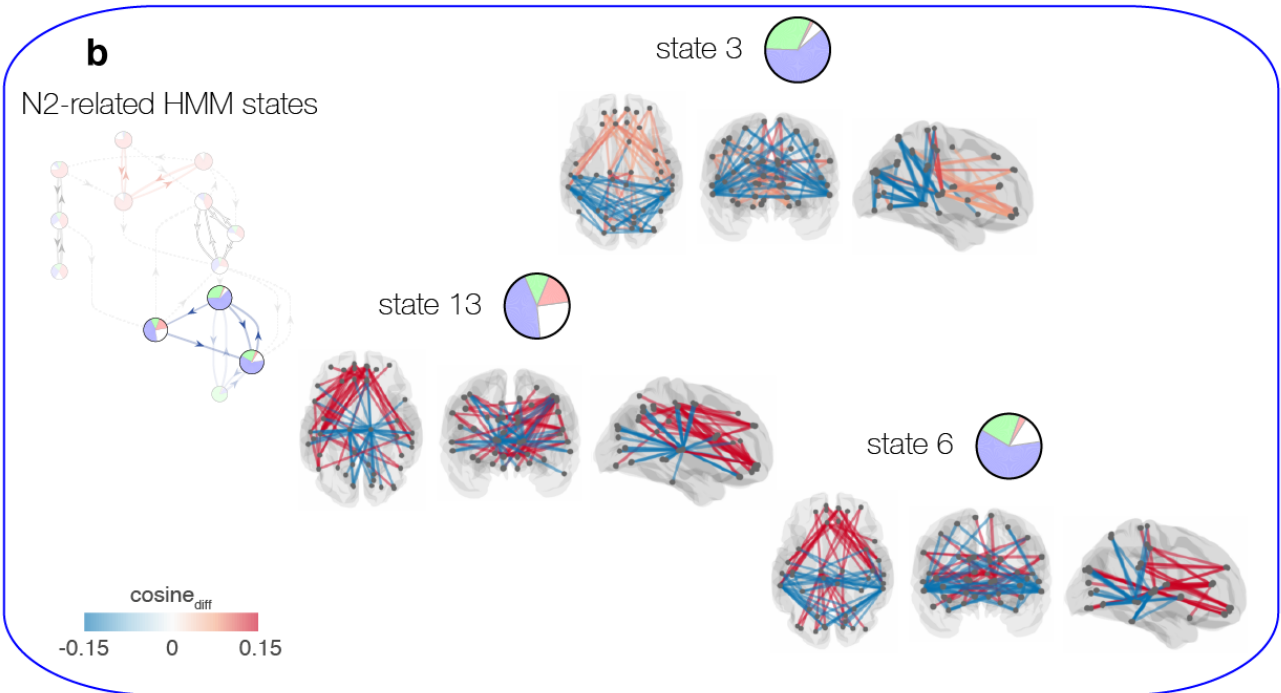
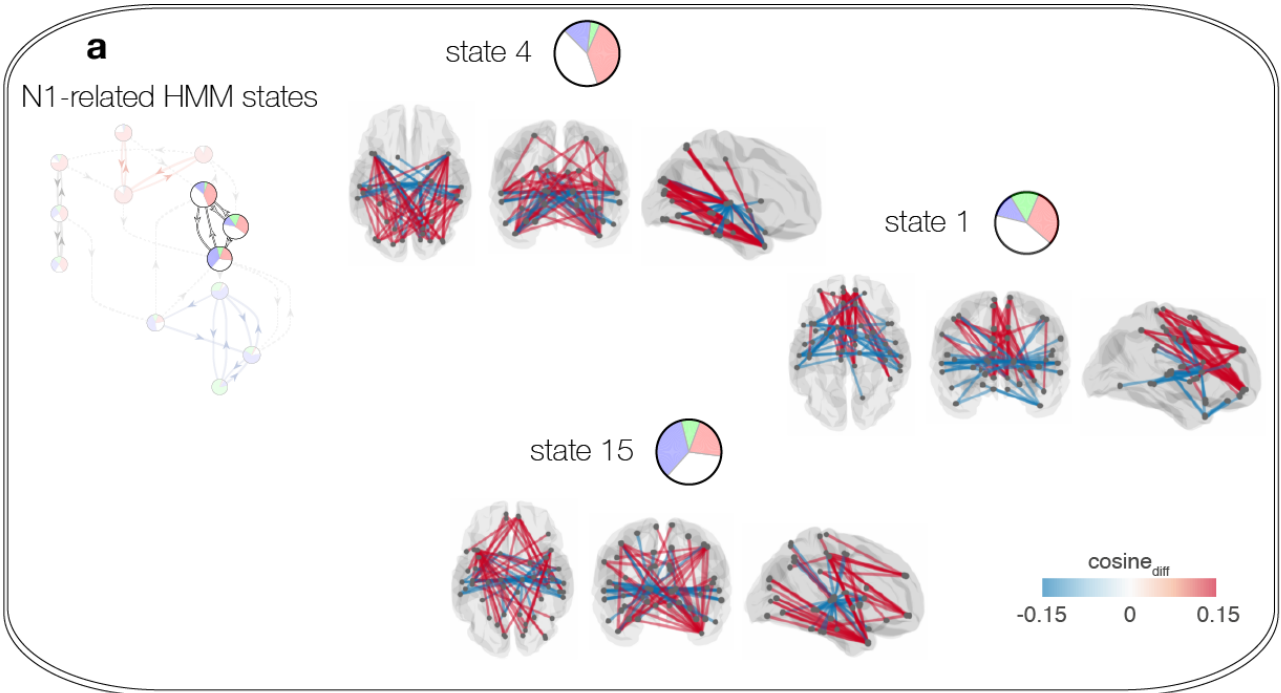
splits of the data ('Half-split 1', $N = 29$, and 'Half-split 2' $N = 28$). The 19 HMM states from a given repetition were matched to the HMM states of the original solution, using the Munkres algorithm, based on the intra-solution state-distances (measured using the Bhattacharyya distance between the states' Gaussian distributions). The matrix shows the pairwise Bhattacharyya distances between the Gaussian distributions following the matching of the HMM states from the different repetition runs. As indicated by the labelling above the matrix, the white borders demarcate states from the various data splits. The smaller black squares surround 5 repetitions of each of the 19 HMM states. The consistent appearance within each of the 9 white squares is a sign that the HMM inferred states with consistent Gaussian distributions. **b** For a pair of HMM states (one original and one from a repetition run) the temporal correspondence was quantified as the ratio between time points of overlap (simultaneous activity or inactivity) and time points of misses. The bar plot shows mean values and error bars show the standard deviations within data-splits. Note how that temporal overlaps outweighed misses for all runs of the HMM.



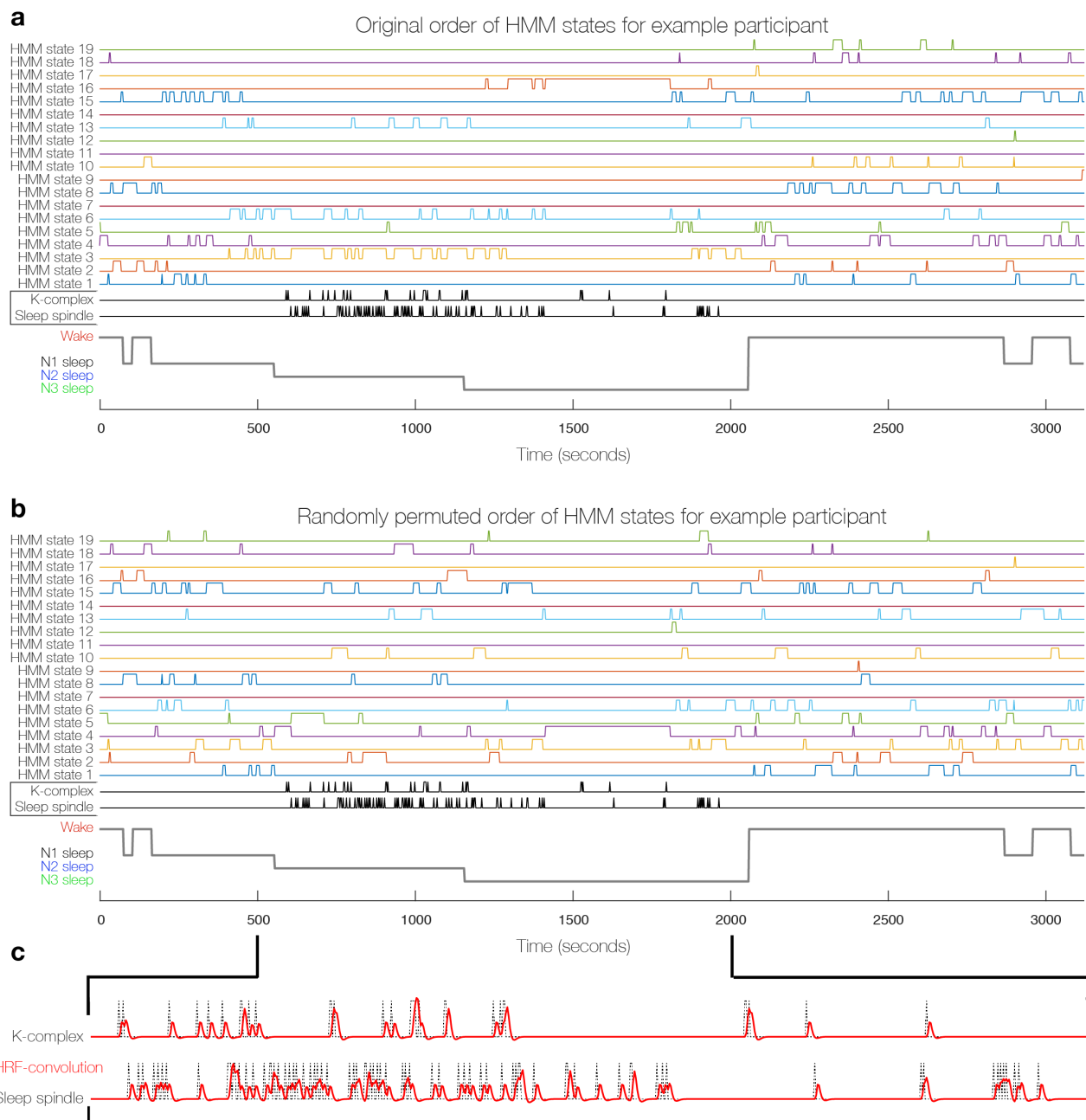
Supplementary Figure 16. Robustness of HMM results without the use of temporal filter (supplement to Figure 3). All plots were computed in the same way as for Figure 3, using an HMM with 19 states. The only difference was that the BOLD data was not temporally filtered. Note in **a** and **b** how, similarly to the results of the main text, select HMM states were sensitive and specific for certain PSG stages (although not for N1 sleep). In **c** the overall mean life time of the HMM states is decreased compared to the results using a low-pass temporal filter (compare with Figure 3). As a consequence, **d** shows increased switching frequencies within all of the four PSG stages. Importantly, the relative differences between the PSG stages were effectively unchanged (even if the significant difference between ‘Wake’ and ‘N2’ was no longer evident). Interestingly, in **e**, the number of unique HMM states visited per unit time were numerically quite stable with or without the use of temporal filter.



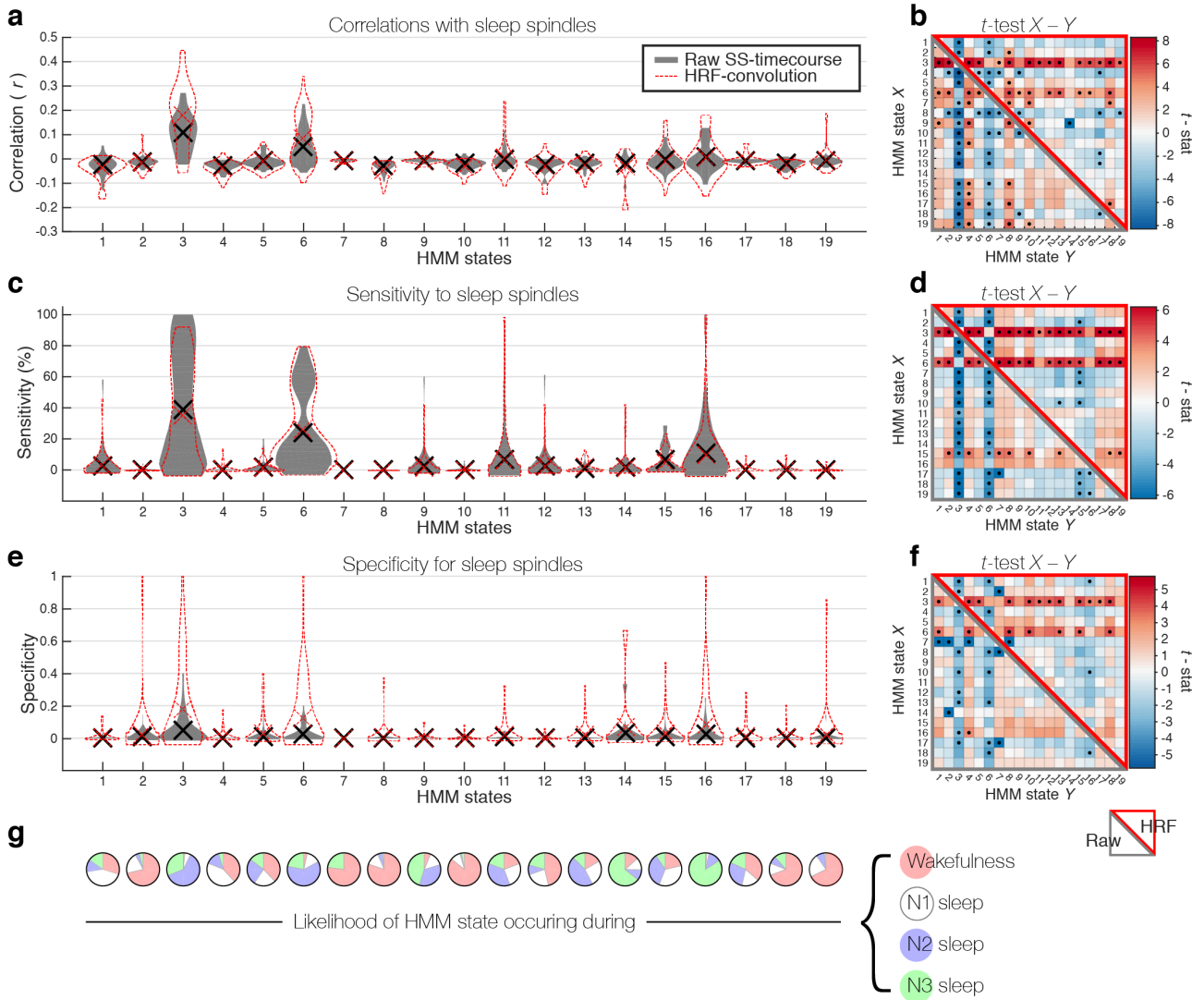
Supplementary Figure 17. Differential cosine similarity maps of wakefulness-related HMM states. (supplement to Supplementary Figure 4). Produced to show that the differential FC maps of Supplementary Figure 4 were not affected by the different mean activations of the HMM states. Please note the qualitative overlap with maps in Supplementary Figure 4. Like for Supplementary Figure 4, the maps show the 1% most negative and 1% most positive weights.



Supplementary Figure 18. *Differential cosine similarity maps of wakefulness-related HMM states.* (supplement to Supplementary Figure 5). Produced to show that the differential FC maps of Supplementary Figure 5 were not affected by the different mean activations of the HMM states. Please note the qualitative overlap with maps in Supplementary Figure 5. Like for Supplementary Figure 5, the maps show the 1% most negative and 1% most positive weights.

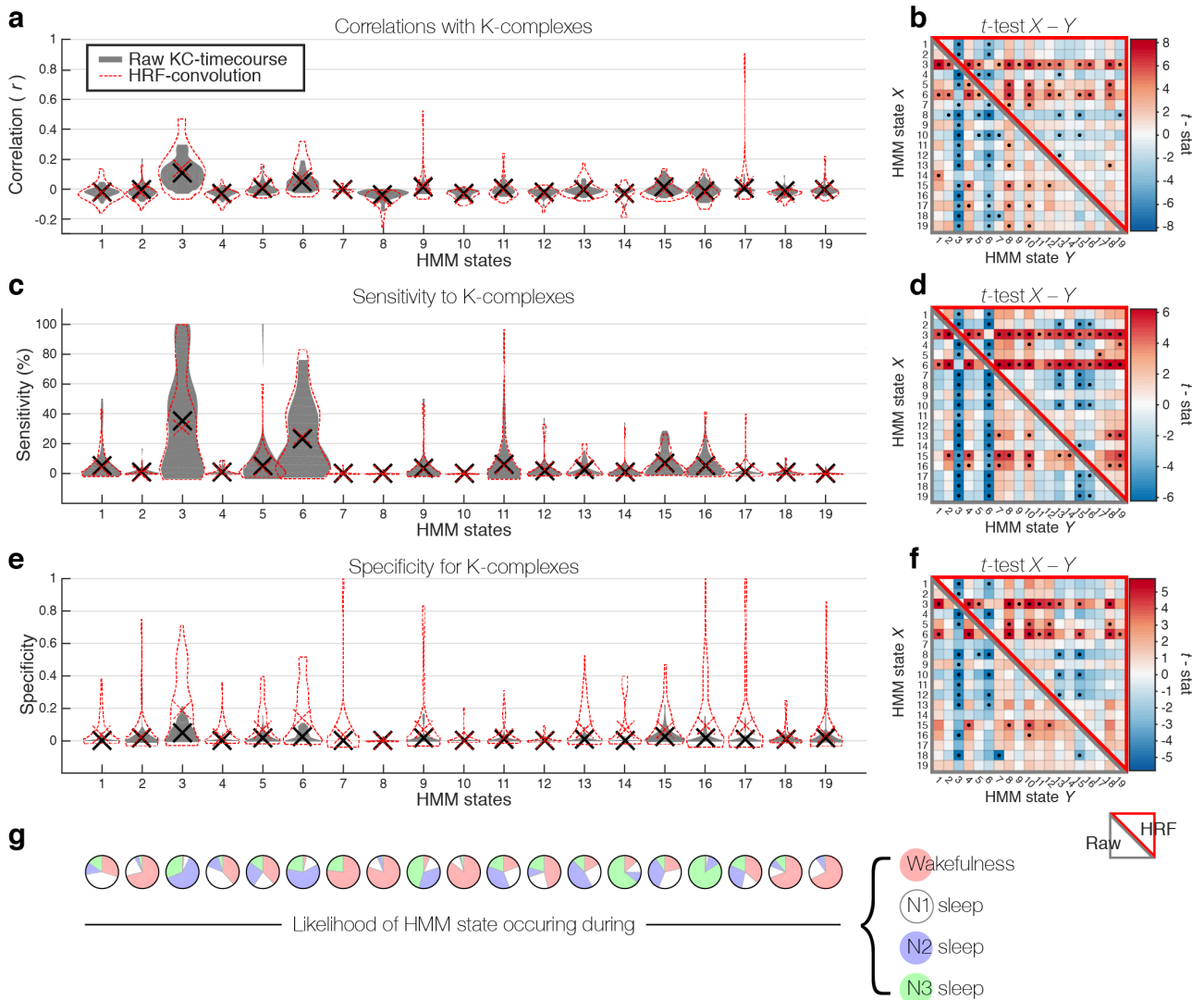


Supplementary Figure 19. Presence of sleep graphoelements in example participant. **a** Plotted together are the 19 HMM state timecourses, the markers of sleep spindles and K-complexes (SS-timecourse and KC-timecourse), and the PSG scoring for an example participant. The SS- and KC-timecourses were based on AASM scoring of sleep graphoelements in the EEG data. Specifically, SS-timecourse and KC-timecourse were binary and of the same length as the fMRI data, with ones representing the fMRI samples during which the respective graphoelement occurred. **b** The same information for the same participant is plotted again, however this time the HMM state timecourses have been randomly permuted. Each permutation consisted in a random switching of the labels of each instance of an HMM state, keeping the number of occurrences of each HMM state and state transition times constant within participants. This was done 1000 times for the purpose of comparing correlation, sensitivity, and specificity of the HMM states to the presence of sleep graphoelements (see Supplementary Figures 20 and 21). **c** The analyses were also performed after convolution of the SS- and KC-timecourses with the canonical hemodynamic response function (HRF). An illustration of the convolution is shown in an enlarged view of the SS- and KC-timecourses from ~500 to ~2000 seconds. The red timecourses with characteristic delays and undershoots represent the HRF-convoluted SS- and KC-timecourses for this example participant.



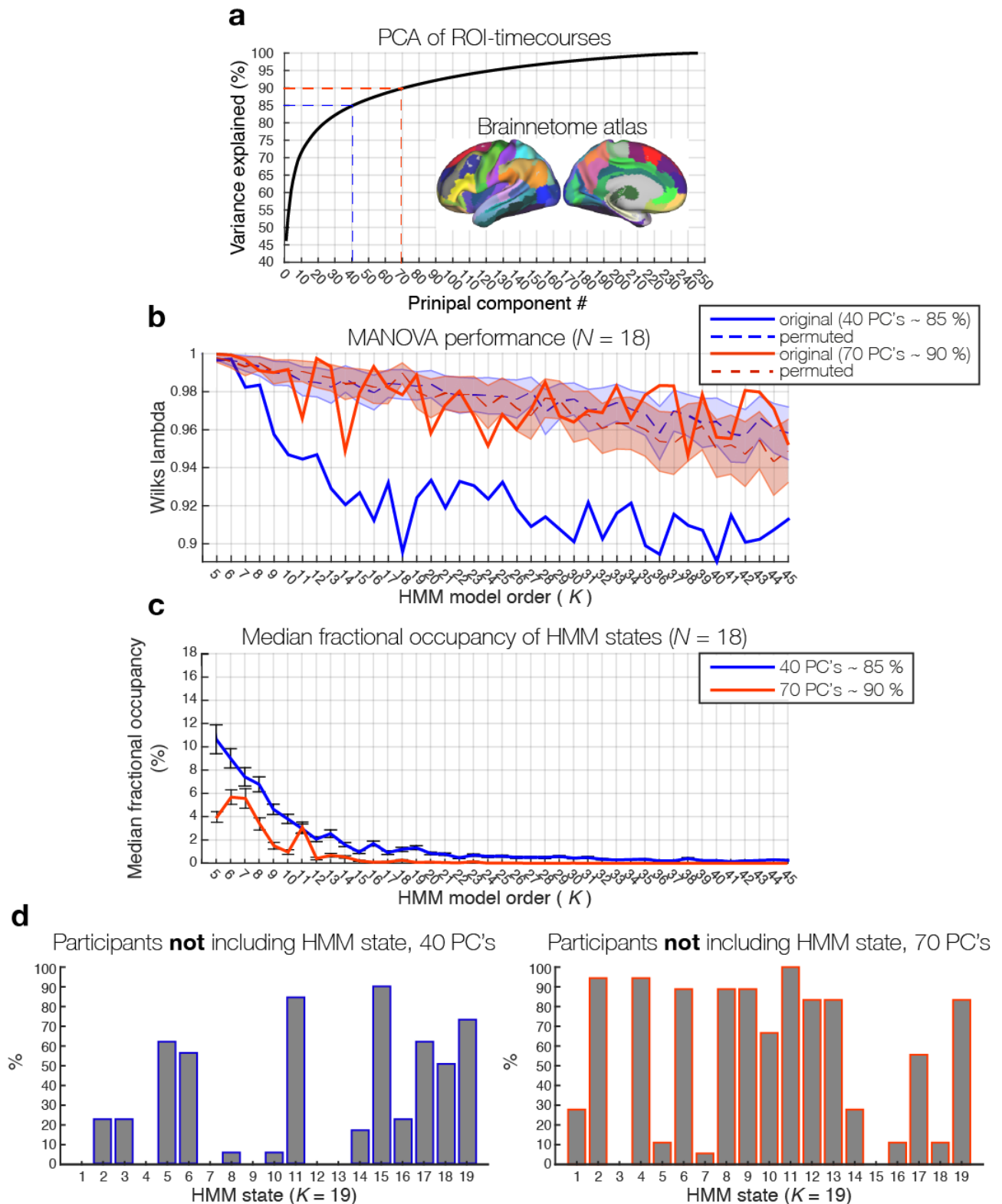
Supplementary Figure 20. Relationship between the 19 HMM states and the presence of sleep spindles. **a** The grey violin plot shows the distribution of Pearson's correlation values computed between the timecourse of each HMM state and the raw timecourse of sleep spindles for each of the 57 participants that included sleep spindles (see Supplementary Table 3 for summary statistics of sleep spindles). The black crosses denote the means across participants. In red are shown the outlines of an equivalent violin plot when considering HRF-convolved versions of the spindle timecourses. **b** The sub-diagonal part of the 19×19 matrix includes the t -statistics resulting from paired t -tests on the correlation values between each pair of the 19 HMM states. The super-diagonal part includes the t -stats considering the HRF-convolved versions of the spindle timecourses. A black star in the center of an entry (x, y) denotes a significant difference between the corresponding pair of HMM state X and Y as evaluated through 1000 random permutations of the HMM state timecourses, at a significance level that has been Bonferroni-corrected for the multiple comparisons between pairs of HMM states. **c** Distributions of sensitivity of each of the 19 HMM states to sleep spindles across participants for raw spindle timecourses (grey) and HRF convolved spindles (red). Sensitivity was defined as the proportion of sleep spindles that occurred within a given HMM state. **d** Equivalent to **b** but for sensitivity values. **e** Distributions of the 19 HMM states' specificity for sleep spindles across participants for raw spindle timecourses (grey) and HRF convolved spindles (red). Specificity was defined as the likelihood of finding a given HMM state active during a spindle, i.e. the ratio of an HMM state's occurrences taking place during spindles. **f** Equivalent to **b** and **d** but for specificity values. **g** For reference are included the circle plots, used throughout the manuscript, indicating the specificity of each HMM state to the sleep stages, calculated for the 18 participants that included all sleep stages. It is clear that sleep spindles correlated higher with the HMM states with high specificity for N2 sleep. HMM states 3 and 6 were thus found to correlate

significantly higher with spindles than most of the other HMM states, while no significant difference were found between the two. This was true regardless of HRF convolution of the spindles. HMM states 3 and 6 also accounted for the majority of spindle occurrences, as quantified through their sensitivity. Given the generally low specificity values, it is also clear that no HMM state occurred exclusively during spindles.



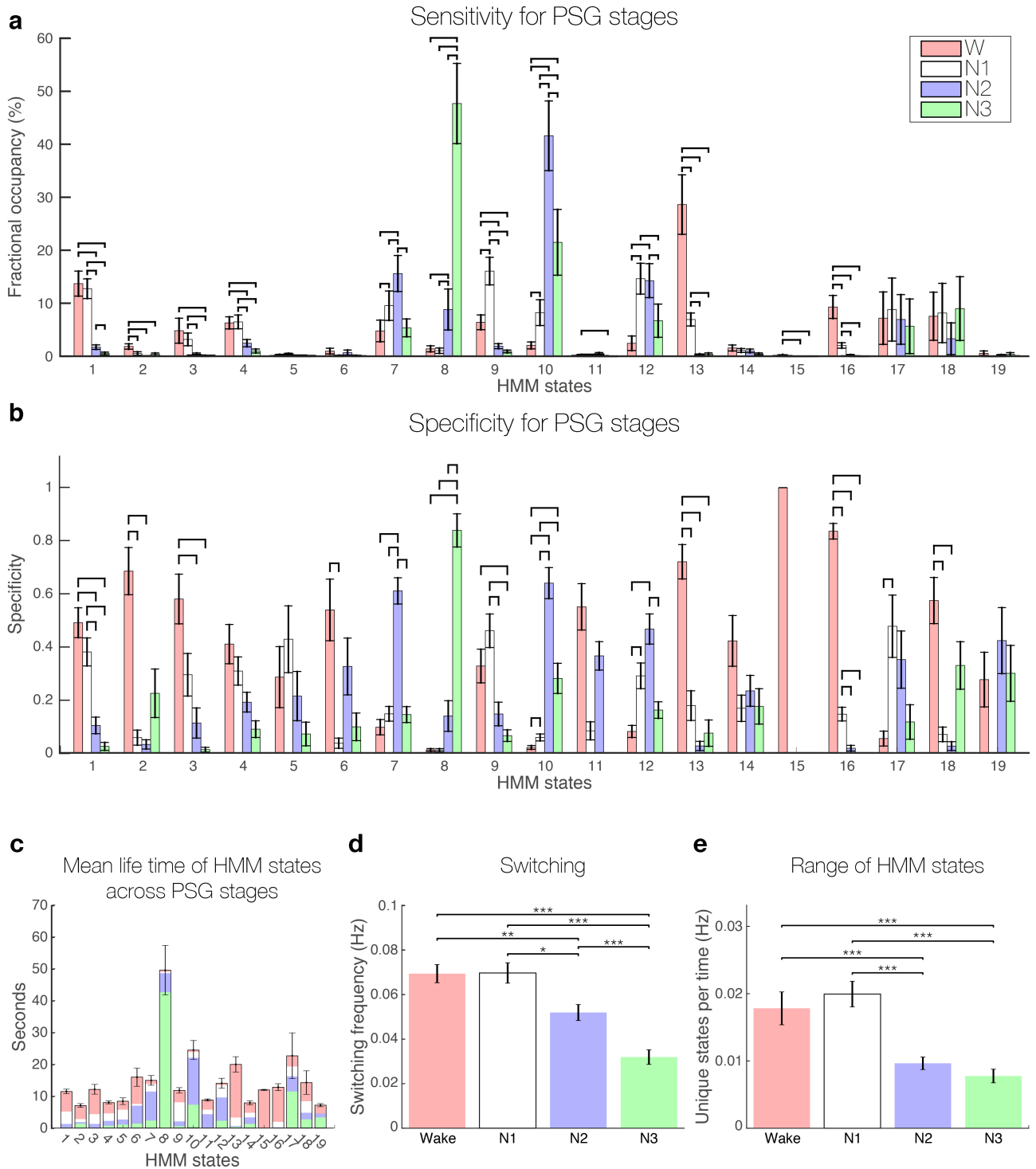
Supplementary Figure 21. Relationship between the 19 HMM states and the presence of K-complexes. **a** The grey violin plot shows the distribution of Pearson's correlation values computed between the timecourse of each HMM state and the raw timecourse of K-complexes for each of the 57 participants that included K-complexes (see Supplementary Table 3 for summary statistics of K-complexes). The black crosses denote the means across participants. In red are shown the outlines of an equivalent violin plot when considering HRF-convolved versions of the KC-timecourses. **b** The sub-diagonal part of the 19×19 matrix includes the t -statistics resulting from paired t -tests on the correlation values between each pair of the 19 HMM states. The super-diagonal part includes the t -stats considering the HRF-convolved versions of the KC-timecourses. A black star in the center of an entry (x, y) denotes a significant difference between the corresponding pair of HMM state X and Y as evaluated through 1000 random permutations of the HMM state timecourses, at a significance level that has been Bonferroni-corrected for the multiple comparisons between pairs of HMM states. **c** Distributions of sensitivity of each of the 19 HMM states to K-complexes across participants for raw KC-timecourses (grey) and HRF convolved K-complexes (red). Sensitivity was defined as the proportion of K-complexes that occurred within a given HMM state. **d** Equivalent to **b** but for sensitivity values. **e** Distributions of the 19 HMM states' specificity for K-complexes across participants for raw KC-timecourses (grey) and HRF convolved K-complexes (red). Specificity was defined as the likelihood of finding a given HMM state active during a K-complex, i.e. the ratio of an HMM state's occurrences taking place during K-complexes. **f** Equivalent to **b** and **d** but for specificity values. **g** For reference are included the circle plots, used throughout the manuscript, indicating the specificity of each HMM state to the sleep stages, calculated for the 18 participants that included all sleep stages. It is clear that the HMM states relate to K-complexes in a fashion highly similar to that of spindles, presented in Supplementary Figure 20. K-complexes correlated higher with the HMM states with high specificity for N2 sleep. HMM states 3 and 6 were thus found to

correlate significantly higher with K-complexes than most of other HMM states, while no significant difference were found between the two. HMM states 3 and 6 also accounted for the majority of K-complex occurrences, as quantified through their sensitivity. Given the generally low specificity values, it is also clear that no HMM state occurred exclusively during K-complexes.



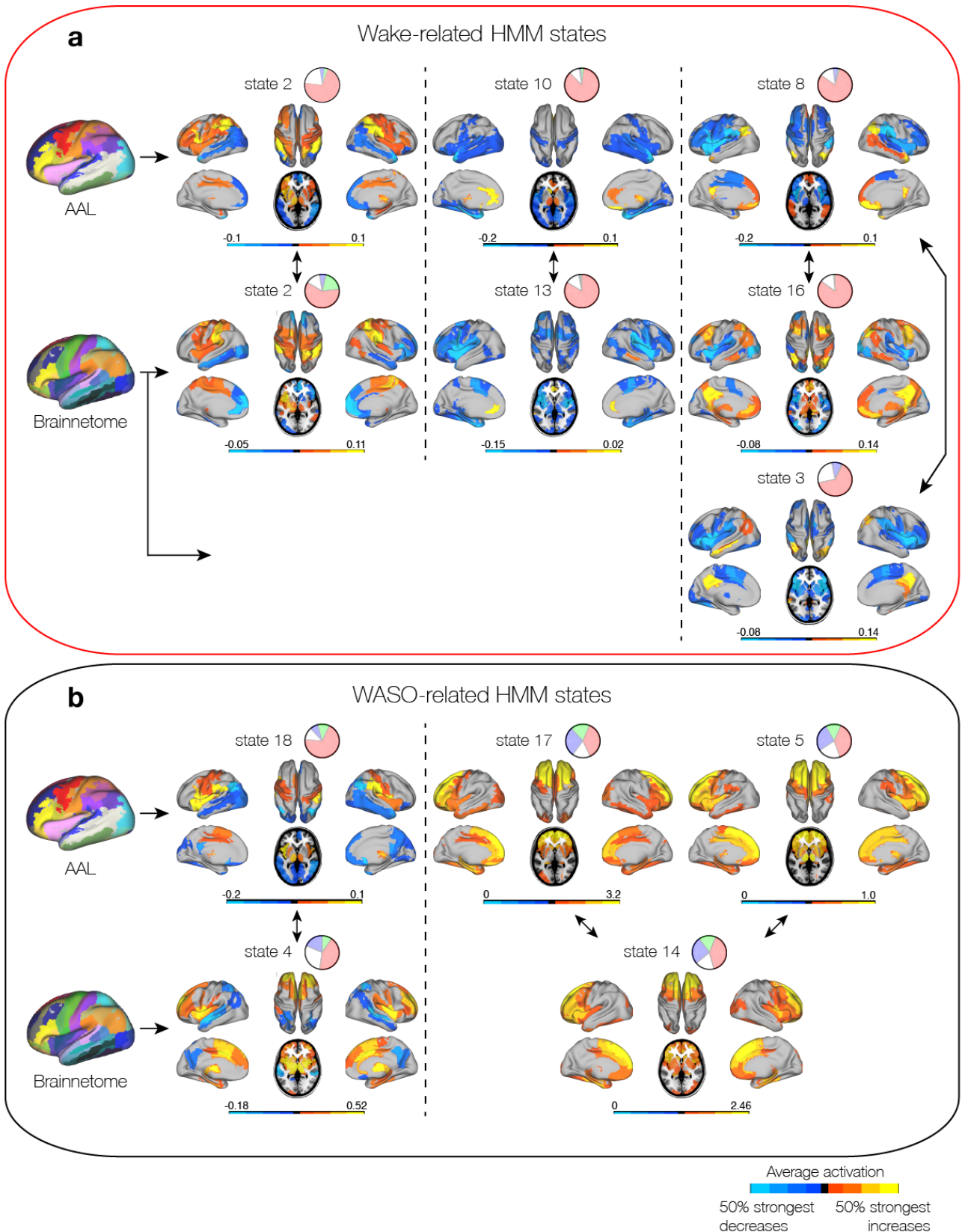
Supplementary Figure 22. Performance of HMM using the Brainnetome atlas. **a** Curve showing the cumulative percentage of variance represented by the components of the PCA performed on the ROI timecourses extracted from the Brainnetome atlas (see Figure 1b for an equivalent plot for the AAL data). The blue and the red dashed lines show the two cases analysed; 40 PC's ~ 85% and 70 PC's ~ 90%, respectively. **b** Plot showing the development across HMM model orders (from 5 to 45 states) of the MANOVA performance of the HMM when compared to the EEG-based sleep scoring for the 18 participants that included all PSG stages (see Supplementary Figure 1b for an equivalent plot for the AAL data). Going

from 90% of the variance (red) to 85% of the variance (blue) had a significant effect on how well the HMM states related to the PSG scoring. Notice how the red line rarely goes below the zone representing the permuted, random cases, whereas the blue line emulates the original analysis on the AAL data (see curve in Supplementary Figure 1b). **c** Tracking of the median fractional occupancy of the HMM states across model orders, within the 18 participants that included all four PSG stages. In blue is shown the curve for 40 PC's ~ 85%, while the result using 70 PC's ~ 90% is shown in red (An equivalent plot for the AAL data may be found in Supplementary Figure 1c). The fact that the red line is consistently lower than the blue suggests that using the higher percentage of variance implied a high occurrence of 'sporadic' HMM states that accounted for only small portions of the data. This is also evident in **d** where the HMM solution using 19 states are shown in more detail, for 40 PC's on the left and for 70 PC's on the right. These plots are equivalent to that of Supplementary Figure 6b, which pertains to the original HMM on the AAL data, and show the percentage of participants that did not include each of the 19 HMM states. Using 40 PC's ~ 85 % of variance produced a result more similar to the original HMM on the AAL, with 12 HMM states being included in more than 25% of the participants, whereas including 70 PC's ~ 90% meant that only 6 HMM states were represented in more than 25% of the participants. Error bars in **b** and **c** represent standard error across HMM states within a model order.



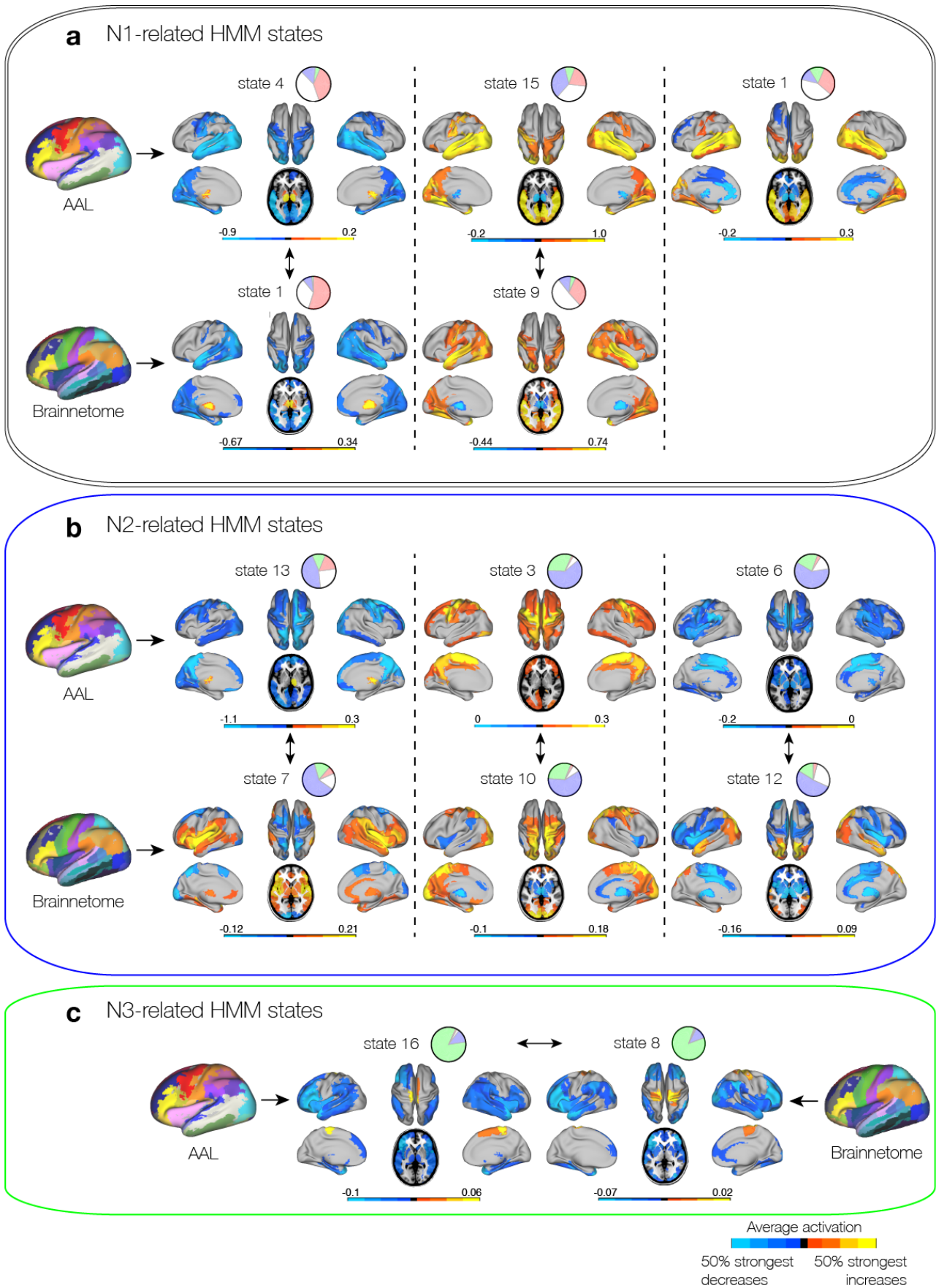
Supplementary Figure 23. Robustness of HMM results when using an alternative parcellation (Brainnetome) (Equivalent to Figure 3 but for the HMM run on 40 PC's ~ 85% of the variance of the Brainnetome ROI timecourses with 19 states). **a** Select HMM states account for the majority of different PSG stages as quantified through their fractional occupancies. **b** In the same way as for the original analysis on the AAL data there is an overlap between the HMM states with high sensitivity for a given PSG stage and the HMM states with high specificity for the same PSG stage. **c** HMM states with high specificity for N3 sleep expressed higher mean life times, as was the case for the original analysis. **d** The relative as well as the absolute values of switching were very similar to those of the original analysis on the AAL data. **e** Similarly to the switching dynamics in E, the ranges of unique HMM states visited within each PSG stage were similar to the original analysis. Please note that all plots were calculated from the 18 participants that included all

PSG stages, and that significant differences between HMM states or PSG stages were calculated in the same way as for Figure 3.



Supplementary Figure 24. Spatial correspondence between HMM states from AAL and Brainnetome in wakefulness-related HMM states. (Brain plots from the Brainnetome data are extracted from the HMM solution with 19 states on the 40 PC's ~ 85% of the variance). To demonstrate the correspondence between the original HMM solution on the AAL data and the HMM solution on the Brainnetome data, the original brain plots of mean activation distributions (from Figure 5) are shown together with brain plots from the

HMM on Brainnetome. These have been matched based on visual similarity between the spatial maps and their specificity profiles for PSG stages, represented in pie plots. **a** The original wake-related HMM states from the AAL together with HMM states from the Brainnetome. Notice the high correspondence not only in spatial distribution but also in the PSG-specificity. The original HMM state 8 appeared to show similarity to two HMM states from the Brainnetome analysis (HMM states 16 and 3). **b** The original three WASO-related HMM states appeared to have two equivalents in the Brainnetome solution.



Supplementary Figure 25. Spatial correspondence between HMM states from AAL and Brainnetome in N1-, N2-, and N3-related HMM states. (Equivalent to Supplementary Figure 24, but for N1-, N2-, and N3-

sleep) **A)** The original N1-related HMM states found two equivalents from the Brainnetome HMM states. **B)** Each of the three original N2-related HMM states had equivalents from the Brainnetome HMM, which was also the case for the original N3-related HMM state shown in **C**.

Supplementary References

1. Maquet P. Functional neuroimaging of normal human sleep by positron emission tomography. *Journal of sleep research* **9**, 207-231 (2000).
2. Hofle N, *et al.* Regional Cerebral Blood Flow Changes as a Function of Delta and Spindle Activity during Slow Wave Sleep in Humans. *The Journal of Neuroscience* **17**, 4800-4808 (1997).
3. Braun AR, *et al.* Regional cerebral blood flow throughout the sleep-wake cycle. An H₂(15)O PET study. *Brain : a journal of neurology* **120 (Pt 7)**, 1173-1197 (1997).
4. Kjaer TW, Law I, Wiltschiøtz G, Paulson OB, Madsen PL. Regional cerebral blood flow during light sleep—a H₂15O - PET study. *J Sleep Res* **11**, 201-207 (2002).
5. Laufs H, *et al.* Where the BOLD signal goes when alpha EEG leaves. *NeuroImage* **31**, 1408-1418 (2006).
6. Horovitz SG, *et al.* Low frequency BOLD fluctuations during resting wakefulness and light sleep: a simultaneous EEG-fMRI study. *Hum Brain Mapp* **29**, 671-682 (2008).
7. Dang-Vu TT, *et al.* Spontaneous neural activity during human slow wave sleep. *Proceedings of the National Academy of Sciences of the United States of America* **105**, 15160-15165 (2008).
8. Brodbeck V, *et al.* EEG microstates of wakefulness and NREM sleep. *NeuroImage* **62**, 2129-2139 (2012).
9. Tagliazucchi E, Laufs H. Decoding wakefulness levels from typical fMRI resting-state data reveals reliable drifts between wakefulness and sleep. *Neuron* **82**, 695-708 (2014).
10. Tagliazucchi E, von Wegner F, Morzelewski A, Borisov S, Jahnke K, Laufs H. Automatic sleep staging using fMRI functional connectivity data. *NeuroImage* **63**, 63-72 (2012).
11. Altmann A, *et al.* Validation of non-REM sleep stage decoding from resting state fMRI using linear support vector machines. *NeuroImage* **125**, 544-555 (2016).
12. Haimovici A, Tagliazucchi E, Balenzuela P, Laufs H. On wakefulness fluctuations as a source of BOLD functional connectivity dynamics. *Sci Rep* **7**, 5908 (2017).

13. Horovitz SG, *et al.* Decoupling of the brain's default mode network during deep sleep. *Proceedings of the National Academy of Sciences of the United States of America* **106**, 11376-11381 (2009).
14. Larson-Prior LJ, Zempel JM, Nolan TS, Prior FW, Snyder AZ, Raichle ME. Cortical network functional connectivity in the descent to sleep. *Proceedings of the National Academy of Sciences of the United States of America* **106**, 4489-4494 (2009).
15. Sämann PG, *et al.* Development of the brain's default mode network from wakefulness to slow wave sleep. *Cerebral cortex* **21**, 2082-2093 (2011).
16. Tagliazucchi E, von Wegner F, Morzelewski A, Brodbeck V, Jahnke K, Laufs H. Breakdown of long-range temporal dependence in default mode and attention networks during deep sleep. *Proceedings of the National Academy of Sciences of the United States of America* **110**, 15419-15424 (2013).
17. Snyder AZ. Intrinsic brain activity and resting state networks. In: *Neuroscience in the 21st Century* (ed[^](eds Pfaff DW, Volkow ND). Springer New York (2016).
18. Schabus M, *et al.* Hemodynamic cerebral correlates of sleep spindles during human non-rapid eye movement sleep. *Proceedings of the National Academy of Sciences of the United States of America* **104**, 13164-13169 (2007).
19. Andrade KC, *et al.* Sleep spindles and hippocampal functional connectivity in human NREM sleep. *The Journal of neuroscience : the official journal of the Society for Neuroscience* **31**, 10331-10339 (2011).
20. Caporro M, *et al.* Functional MRI of sleep spindles and K-complexes. *Clinical neurophysiology : official journal of the International Federation of Clinical Neurophysiology* **123**, 303-309 (2012).
21. Jahnke K, *et al.* To wake or not to wake? The two-sided nature of the human K-complex. *NeuroImage* **59**, 1631-1638 (2012).
22. Laufs H, Walker MC, Lund TE. 'Brain activation and hypothalamic functional connectivity during human non-rapid eye movement sleep: an EEG/fMRI study'--its limitations and an alternative approach. *Brain : a journal of neurology* **130**, e75; author reply e76 (2007).
23. Nir Y, *et al.* Regional slow waves and spindles in human sleep. *Neuron* **70**, 153-169 (2011).
24. Piantoni G, Halgren E, Cash SS. Spatiotemporal characteristics of sleep spindles depend on cortical location. *NeuroImage* **146**, 236-245 (2017).

25. Mak-McCully RA, *et al.* Distribution, Amplitude, Incidence, Co-Occurrence, and Propagation of Human K-Complexes in Focal Transcortical Recordings. *eNeuro* **2**, ENEURO.0028-0015.2015 (2015).
26. Maxim V, *et al.* Fractional Gaussian noise, functional MRI and Alzheimer's disease. *NeuroImage* **25**, 141-158 (2005).
27. He BJ. Scale-free properties of the functional magnetic resonance imaging signal during rest and task. *Journal of Neuroscience* **31**, 13786-13795 (2011).
28. Ciuciu P, Varoquaux G, Abry P, Sadaghiani S, Kleinschmidt A. Scale-Free and Multifractal Time Dynamics of fMRI Signals during Rest and Task. *Front Physiol* **3**, 186 (2012).
29. von Wegner F, Tagliazucchi E, Laufs H. Information-theoretical analysis of resting state EEG microstate sequences - non-Markovianity, non-stationarity and periodicities. *NeuroImage* **158**, 99-111 (2017).
30. Vidaurre D, Smith SM, Woolrich MW. Brain network dynamics are hierarchically organized in time. *Proceedings of the National Academy of Sciences of the United States of America* **114**, 12827-12832 (2017).
31. Allen EA, Damaraju E, Plis SM, Erhardt EB, Eichele T, Calhoun VD. Tracking whole-brain connectivity dynamics in the resting state. *Cerebral cortex (New York, NY : 1991)* **24**, 663-676 (2014).
32. Hindriks R, *et al.* Can sliding-window correlations reveal dynamic functional connectivity in resting-state fMRI? *NeuroImage* **127**, 242-256 (2015).
33. Tagliazucchi E, Balenzuela P, Fraiman D, Chialvo DR. Criticality in large-scale brain FMRI dynamics unveiled by a novel point process analysis. *Frontiers in physiology* **3**, 15 (2012).
34. Liu X, Duyn JH. Time-varying functional network information extracted from brief instances of spontaneous brain activity. *Proceedings of the National Academy of Sciences* **110**, 4392-4397 (2013).
35. Karahanoğlu FI, Ville DVD. Transient brain activity disentangles fMRI resting-state dynamics in terms of spatially and temporally overlapping networks. *Nature communications* **6**, 7751 (2015).

36. Calhoun Vince D, Miller R, Pearlson G, Adalı T. The Chronnectome: Time-Varying Connectivity Networks as the Next Frontier in fMRI Data Discovery. *Neuron* **84**, 262-274 (2014).
37. Preti MG, Bolton TAW, Ville DVD. The dynamic functional connectome: State-of-the-art and perspectives. *NeuroImage*, (2016).
38. Baker AP, *et al.* Fast transient networks in spontaneous human brain activity. *eLife* **3**, e01867 (2014).
39. Vidaurre D, Quinn AJ, Baker AP, Dupret D, Tejero-Cantero A, Woolrich MW. Spectrally resolved fast transient brain states in electrophysiological data. *NeuroImage* **126**, 81-95 (2016).
40. Vidaurre D, *et al.* Spontaneous cortical activity transiently organises into frequency specific phase-coupling networks. *Nature communications* **9**, 2987 (2018).
41. Ryali S, *et al.* Temporal Dynamics and Developmental Maturation of Salience, Default and Central-Executive Network Interactions Revealed by Variational Bayes Hidden Markov Modeling. *PLoS computational biology* **12**, e1005138 (2016).
42. Deco G, *et al.* Perturbation of whole-brain dynamics in silico reveals mechanistic differences between brain states. *NeuroImage* **169**, 46-56 (2018).
43. Jobst BM, *et al.* Increased Stability and Breakdown of Brain Effective Connectivity During Slow-Wave Sleep: Mechanistic Insights from Whole-Brain Computational Modelling. *Sci Rep* **7**, 4634 (2017).
44. Deco G, Hagmann P, Hudetz AG, Tononi G. Modeling resting-state functional networks when the cortex falls asleep: local and global changes. *Cerebral cortex* **24**, 3180-3194 (2014).
45. Cabral J, Kringelbach ML, Deco G. Functional connectivity dynamically evolves on multiple time-scales over a static structural connectome: Models and mechanisms. *NeuroImage* **160**, 84-96 (2017).
46. Lavigne G, Kryger M. Chapter 11 - Relevance of Sleep Physiology for Sleep Medicine Clinicians. In: *Principles and Practice of Sleep Medicine (Sixth Edition)* (ed[^](eds Kryger M, Roth T, Dement WC). Elsevier (2017).
47. Ogilvie RD, Wilkinson RT. The detection of sleep onset: behavioral and physiological convergence. *Psychophysiology* **21**, 510-520 (1984).

48. Bonnet MH, Moore SE. The threshold of sleep: perception of sleep as a function of time asleep and auditory threshold. *Sleep* **5**, 267-276 (1982).
49. Siclari F, *et al.* The neural correlates of dreaming. *Nature neuroscience* **20**, 872-878 (2017).
50. Nobili L, *et al.* Chapter 13 - Local aspects of sleep: Observations from intracerebral recordings in humans. In: *Progress in Brain Research* (ed[^](eds Andries Kalsbeek MMTR, Russell GF). Elsevier (2012).
51. Goupil L, Bekinschtein TA. Cognitive processing during the transition to sleep. *Archives italiennes de biologie* **150**, 140-154 (2012).
52. Hori T, Hayashi M, Morikawa T. Topographical EEG changes and the hypnagogic experience. (1994).
53. Tassi P, Muzet A. Sleep inertia. *Sleep medicine reviews* **4**, 341-353 (2000).
54. Diekelmann S, Born J. The memory function of sleep. *Nature reviews Neuroscience* **11**, 114-126 (2010).
55. Wei Y, *et al.* Sleep Stage Transition Dynamics Reveal Specific Stage 2 Vulnerability in Insomnia. *Sleep* **40**, zsx117-zsx117 (2017).
56. Chang C, *et al.* Tracking brain arousal fluctuations with fMRI. *Proceedings of the National Academy of Sciences* **113**, 4518-4523 (2016).
57. Stickgold R. Sleep-dependent memory consolidation. *Nature* **437**, 1272-1278 (2005).
58. Edinger JD, Ulmer CS, Means MK. Sensitivity and Specificity of Polysomnographic Criteria for Defining Insomnia. *Journal of clinical sleep medicine : JCSM : official publication of the American Academy of Sleep Medicine* **9**, 481-491 (2013).
59. Manconi M, *et al.* Measuring the error in sleep estimation in normal subjects and in patients with insomnia. *J Sleep Res* **19**, 478-486 (2010).
60. Littner M, *et al.* Practice parameters for using polysomnography to evaluate insomnia: an update. *Sleep* **26**, 754-760 (2003).

61. Ni Mhuirheartaigh R, Warnaby C, Rogers R, Jbabdi S, Tracey I. Slow-wave activity saturation and thalamocortical isolation during propofol anesthesia in humans. *Sci Transl Med* **5**, 208ra148 (2013).
62. Uhrig L, Dehaene S, Jarraya B. Cerebral mechanisms of general anesthesia. *Annales francaises d'anesthesie et de reanimation* **33**, 72-82 (2014).
63. Barttfeld P, Uhrig L, Sitt JD, Sigman M, Jarraya B, Dehaene S. Signature of consciousness in the dynamics of resting-state brain activity. *Proceedings of the National Academy of Sciences of the United States of America* **112**, 887-892 (2015).
64. Carhart-Harris RL, *et al.* The entropic brain: a theory of conscious states informed by neuroimaging research with psychedelic drugs. *Frontiers in human neuroscience* **8**, 20 (2014).
65. Dehaene S, Charles L, King JR, Marti S. Toward a computational theory of conscious processing. *Current opinion in neurobiology* **25**, 76-84 (2014).
66. Vidaurre D, *et al.* Discovering dynamic brain networks from big data in rest and task. *NeuroImage*, (2017).
67. Olbrich S, *et al.* EEG-vigilance and BOLD effect during simultaneous EEG/fMRI measurement. *NeuroImage* **45**, 319-332 (2009).
68. Eickhoff SB, Yeo BTT, Genon S. Imaging-based parcellations of the human brain. *Nature Reviews Neuroscience*, 1 (2018).
69. Fan L, *et al.* The Human Brainnetome Atlas: A New Brain Atlas Based on Connectional Architecture. *Cereb Cortex* **26**, 3508-3526 (2016).
70. Bhattacharyya A. On a measure of divergence between two statistical populations defined by their probability distributions. *Bulletin of the Calcutta Mathematical Society* **35**, 99-109 (1943).
71. Munkres J. Algorithms for the Assignment and Transportation Problems. *Journal of the Society for Industrial and Applied Mathematics* **5**, 32-38 (1957).
72. Iber C, Ancoli-Israel S, Chesson A, Quan SF. The AASM manual for the scoring of sleep and associated events: rules, terminology and technical specifications. (ed[^](eds). American Academy of Sleep Medicine Westchester, IL (2007).

73. Piantoni G, Halgren E, Cash SS. The Contribution of Thalamocortical Core and Matrix Pathways to Sleep Spindles. *Neural plasticity* **2016**, 3024342 (2016).
74. Luthi A. Sleep spindles: where they come from, what they do. *The Neuroscientist : a review journal bringing neurobiology, neurology and psychiatry* **20**, 243-256 (2014).
75. Murphy M, Riedner BA, Huber R, Massimini M, Ferrarelli F, Tononi G. Source modeling sleep slow waves. *Proceedings of the National Academy of Sciences* **106**, 1608-1613 (2009).